Faculty of Mathematics and Natural Sciences | RWTH AACHEN UNIVERSITY

Probing Electric and Magnetic Order in 2D van der Waals Heterostructures with Scanning Tunneling Methods

Von der Fakultät für Mathematik und Naturwissenschaften der RWTH Aachen University zur Erlangung des akademischen Grades eines Doktors der Naturwissenschaften genehmigte Dissertation vorgelegt von

Keda Jin, M. Sc.
aus
Yunnan, China

Berichter: Univ.-Prof. Dr. Markus Ternes
apl. Prof. Dr. rer. nat. Thomas Schäpers

Tag der mündlichen Prüfung: June 17, 2025

Diese Dissertation ist auf den Internetseiten der Universitätsbibliothek verfügbar.

Eidesstattliche Erklärung
Declaration of Authorship

I, Keda Jin
declare that this thesis and the work presented in it are my own and has been generated by me as the result of my own original research. Hiermit erkläre ich an Eides statt / I do solemnely swear that:

1. This work was done wholly or mainly while in candidature for the doctoral degree at this faculty and university;

2. Where any part of this thesis has previously been submitted for a degree or any other qualification at this university or any other institution, this has been clearly stated;

3. Where I have consulted the published work of others or myself, this is always clearly attributed;

4. Where I have quoted from the work of others or myself, the source is always given. This thesis is entirely my own work, with the exception of such quotations;

5. I have acknowledged all major sources of assistance;

6. Where the thesis is based on work done by myself jointly with others, I have made clear exactly what was done by others and what I have contributed myself;

7. Parts of this work have been published before as:

Keda Jin, Tobias Wichmann, Sabine Wenzel, Tomas Samuely, Oleksander Onufriienko, Pavol Szabó, Kenji Watanabe, Takashi Taniguchi, Jiaqiang Yan, F. Stefan Tautz, Felix Lüpke, Markus Ternes, and Jose Martinez-Castro *Assembly of Arbitrary Designer Heterostructures with Atomically Clean Interfaces.* Adv. Mater. Interfaces (2023)

date

signature

In Wirklichkeit aber hatte man eben etwas Neues gelernt,
an das man vorher nicht gedacht hatte.
— W. Heisenberg
in "Kausalgesetz und Quantenmechanik" (1931)

To my parents and my grandparents.

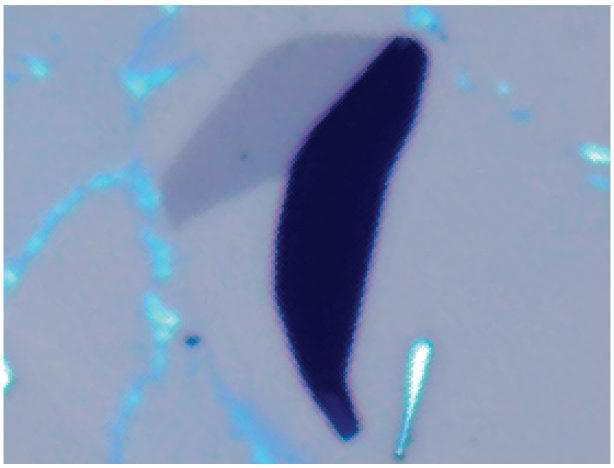

I found a graphene flake; its shape resembles a silhouette of a parrot.
Yet, the physics of the two-dimensional materials explored in this thesis
lies hidden beneath countless flakes like this parrot-shaped graphene sheet.

Acknowledgements

This PhD journey in Jülich has been a remakable chapter of my life, because of such an interesting scientific topic and the invaluable support from my colleagues, friends and family. Their presence and encouragement have been important; without them, this thesis would not have been possible.

First and foremost, I would like to express my appreciation to my PhD advisor **Prof. Markus Ternes**, for giving me an opportunity to join the Peter Grünberg Institute (PGI-3) at Forschungszentrum Jülich, where I jumped into a new world and started from zero in the low-temperature STM and 2D materials. His scientific expertise, encouragement, and invaluable feedback have greatly shaped this thesis and my personal development.

I extend my heartfelt thanks to **Dr. Jose Martinez Castro** for his supervision. For over two years, he patiently taught me his knowledge in the preparation of the 2D heterostructure sample and using STM for the measurement. I appreciate the time we have together in the lab, trying different polymers to transfer 2D material flakes. Without his insights and determination, this suspended dry pick-up and flip-over assembly technique would never have come out. Beyond experiment, he also taught me important aspects of academic writing and scientific presentation.

I would like to thank **Prof. Felix Lüpke**, the leader of our 2D team, for ensuring the optimal performance of every instrument, especially the STM. His guidance in exploring the physics of 2D materials, plus his experimental expertise and theoretical insights, has helped me overcome challenges and inspired meaningful discussions.

I wish to thank **Prof. Frank Stefan Tautz**, the director of PGI-3, for establishing a cutting-edge scientific infrastructure, including state-of-the-art laboratories and fostering close collaborations among different research groups. These contributions were important for the work presented in this thesis. It has been an honour to work in his institute, where scientific freedom and open exchange of ideas thrive.

I would like to thank Prof.**Thomas Schäpers** for being the second referee of this thesis.

I am grateful to **Tobias Wichmann**, who started together with me on a similar project. Over

the past three and half years, we collaborated in the lab, attended DPG spring meetings, workshops, and summer schools together, and shared many memorable experiences.

Special thanks to **Dr. Lennart Klebl** and **Prof. Dante Kennes** for their theoretical collaborations. Their deep understanding of solid-state physics provided crucial insights that complemented my experimental work. The discussions we shared were instrumental in bridging the gap between the observed phenomena and the underlying physics, helping me contextualize and interpret my measurements with greater clarity.

I am also grateful to my colleagues from the 2D lab and the weekly 2D meetings, including **Jonas Daniel Gerber**, **Zhongkui Lyu**, **Dr. Xiaosheng Yang**, **Dr. Sabine Wenzel**, **Dr. Honey Boban**, **Prof. Jia Grace Lu**, and **Abhisek Kole**. My heartfelt thanks go to **Junting Zhao**, who worked together with me during her master's thesis.

My office mates, **Janine Lorenz**, **Dr. Mark Hutter**, and **Dr. Jose Maria Guevara**, deserve my appreciation for fostering a warm and friendly atmosphere in the office.

Warm Acknowledgment goes to **Yuqing Wang** for helping me etch tungsten tips, as well as to **Claudia Funk** and **Helmut Stollwerk** for their technical support. I also extend my gratitude to the staff at Helmholtz Nano Facility, especially **Dr. Florian Lentz**, for assisting me with electron beam lithography work.

I owe thanks to **Dr. Hao Yin** for driving me to the lab through snowy and rainy days over the past three and half years. A sincere thanks to **Dr. Caiyun Chen** and **Dr.Jonathan Karl Hofmann** for taking the time to read the draft of this thesis and for their comments, which improved the quality of this work. I also want to thank my friends, whom I cannot list all here, for their support and fun times spent together.

Finally, I reserve my deepest gratitude to my family, especially my parents, **Yuzhu Yang** and **Wenjing Jin**, and my grandparents who always love and support me. Their love and education have shaped the person I am today (for worse or better). Words cannot express the depth of my appreciation and love for them. Thank you very much! Herzlichen Dank!

Jülich, November 28, 2025 Keda Jin

Abstract

Van der Waals (vdW) heterostructures offer a versatile platform for engineering exotic quantum states of matter. These states arise at the interfaces where layers are weakly coupled by vdW interactions. Scanning tunnelling microscopy (STM) provides a powerful tool to probe these interfaces, offering a microscopic understanding of these exotic states. However, STM requires pristine sample surfaces, often incompatible with conventional polymer-based transfer techniques. The first step of this thesis involved developing a novel assembly method to fabricate clean heterostructures by avoiding direct contact between the polymer and the materials. This approach enables the creation of air-sensitive heterostructures with clean interfaces and surfaces, which is compatible with STM investigations.

Using this method, three systems were studied: 1T-$NbSe_2$ on 2H-$NbSe_2$, graphene on 1T-$NbSe_2$/2H-$NbSe_2$, and CrSBr on 2H-$NbSe_2$. In the first system, the $\sqrt{13} \times \sqrt{13}$ charge density wave (CDW) in 1T-$NbSe_2$ led to localized states within the CDW superlattice. Interfacing 1T-$NbSe_2$ with metallic 2H-$NbSe_2$ provided a platform to investigate the competition between Heisenberg coupling of local moments and Kondo coupling in a two-dimensional system. STM measurements revealed high inhomogeneities of electronic structure on the nanometer scale. This inhomogeneities is due to the incommensurate stacking of $\sqrt{13} \times \sqrt{13}$ CDW in 1T-$NbSe_2$ and $\sqrt{3} \times \sqrt{3}$ CDW in 2H-$NbSe_2$.

The second system of this thesis focuses on engineering flat bands through superlattice engineering. By stacking graphene on 1T-$NbSe_2$/2H-$NbSe_2$ with controlled twist angles, two near-commensurate superlattices—2×2 and $\sqrt{3} \times \sqrt{3}$—aligned with the CDW of 1T-$NbSe_2$ were realized. In the 2×2 superlattice, the C_3 rotational symmetry was preserved, while in the $\sqrt{3} \times \sqrt{3}$ superlattice, a stripe phase with C_2 rotational symmetry emerged, indicating broken symmetry and tunable electronic behaviours.

The third part investigates flat bands in systems with highly anisotropic band structures, exemplified by the 2D magnet CrSBr. In CrSBr, weak interlayer coupling results in dispersive electronic states along one-dimensional chains, but localized with the chains. By engineering CrSBr on 2H-$NbSe_2$, STM visualized the quasi-one-dimensional electronic structure in real space with high spatial and energy resolution. Furthermore, a reconstruction of the electronic band structure of CrSBr induced by spin canting in the external magnetic field was observed.

Abstract

This work provides fundamental insight into the interplay between electronic structure, symmetry breaking, and magnetic ordering in van der Waals heterostructures and presents a key step for future research on the emergence and manipulation of quantum phenomena in these systems.

Zusammenfassung

Van-der-Waals (vdW)-Heterostrukturen bieten eine vielseitige Plattform für die Entwicklung exotischer Quantenzustände der Materie. Diese Zustände entstehen an den Grenzflächen, wo die Schichten durch vdW-Wechselwirkungen schwach gekoppelt sind. Die Rastertunnelmikroskopie (STM) ist ein leistungsfähiges Instrument zur Untersuchung dieser Grenzflächen und ermöglicht ein mikroskopisches Verständnis dieser exotischen Zustände. Die STM erfordert jedoch atmor reine Probenoberflächen, die mit herkömmlichen polymerbasierten Übertragungstechniken oft nicht kompatibel sind. Der erste Schritt dieser Arbeit bestand in der Entwicklung einer neuartigen Montagemethode zur Herstellung atomar sauberer Heterostrukturen, indem der direkte Kontakt zwischen dem Polymer und den Materialien vermieden wird. Dieser Ansatz ermöglicht die Herstellung von luftempfindlichen Heterostrukturen mit sauberen Grenzflächen und Oberflächen, die mit STM-Untersuchungen kompatibel sind.

Mit dieser Methode wurden drei Systeme untersucht: 1T-$NbSe_2$ auf 2H-$NbSe_2$, Graphen auf 1T-$NbSe_2$/2H-$NbSe_2$ und CrSBr auf 2H-$NbSe_2$. Im ersten System führte die $\sqrt{13}\times\sqrt{13}$ Ladungsdichtewelle (CDW) in 1T-$NbSe_2$ zu lokalisierten Zuständen innerhalb des CDW-Übergitters. Die Kopplung von 1T-$NbSe_2$ mit metallischem 2H-$NbSe_2$ bot eine Plattform zur Untersuchung der Konkurrenz zwischen Heisenberg-Kopplung lokaler Momente und Kondo-Kopplung in einem zweidimensionalen System. STM-Messungen ergaben starke Inhomogenitäten der elektronischen Struktur im Nanometerbereich. Diese Inhomogenität ist auf die inkommensurate Stapelung von $\sqrt{13}\times\sqrt{13}$ CDW in 1T-$NbSe_2$ und $\sqrt{3}\times\sqrt{3}$ CDW in 2H-$NbSe_2$ zurückzuführen.

Das zweite System dieser Arbeit konzentriert sich auf die Entwicklung flacher Bänder durch Übergittertechnik. Durch das Stapeln von Graphen auf 1T-$NbSe_2$/2H-$NbSe_2$ mit kontrollierten Verdrehungswinkeln wurden zwei nahezu kommensurate Übergitter - 2×2 und $\sqrt{3}\times\sqrt{3}$ - realisiert, die mit der CDW von 1T-$NbSe_2$ ausgerichtet sind. Im 2×2-Übergitter blieb die C_3-Rotationssymmetrie erhalten, während im $\sqrt{3}\times\sqrt{3}$-Übergitter eine Streifenphase mit C_2-Rotationssymmetrie auftrat, was auf eine gebrochene Symmetrie und ein abstimmbares elektronisches Verhalten hinweist.

Im dritten Teil werden flache Bänder in Systemen mit hochgradig anisotropen Bandstrukturen untersucht, wie am Beispiel des 2D-Magneten CrSBr. In CrSBr führt eine schwache Zwischenschichtkopplung zu dispersiven elektronischen Zuständen entlang eindimensionaler Ketten, die jedoch mit den Ketten lokalisiert sind. Durch die Konstruktion von CrSBr auf

Zusammenfassung

2H-$NbSe_2$ konnte mit STM die quasi eindimensionale elektronische Struktur im realen Raum mit hoher räumlicher und energetischer Auflösung sichtbar gemacht werden. Darüber hinaus wurde eine Rekonstruktion der elektronischen Bandstruktur von CrSBr beobachtet, die durch Spin-Verkantung im externen Magnetfeld hervorgerufen wird.
Diese Arbeit gibt einen grundlegenden Einblick in das Zusammenspiel zwischen elektronischer Struktur, Symmetriebrechung und magnetischer Ordnung in van-der-Waals-Heterostrukturen und stellt einen wichtigen Schritt für die künftige Forschung zur Entstehung und Manipulation von Quantenphänomenen in diesen Systemen dar.

Contents

List of Figures

List of Tables

Acronym

2D two-dimensional

AC alternating current

AFM atomic force microscopy

CB conduction band

CDW charge density wave

DC direct current

DFT density functional theory

FFT fast Fourier transform

FWHM full width at half maximum

Gr graphene

HNF Helmholtz Nano Facility

LDOS local density of states

LHB lower Hubbard band

PDMS polydimethylsiloxane

PMMA polymethyl methacrylate

PVC polyvinyl chloride

SOC spin orbital coupling

SoD star of David

SOC spin-orbit coupling

STM scanning tunneling microscopy

STS scanning tunnelling spectroscopy

TMD transition metal dichalcogenide

TMR tunnelling magnetoresistance

tBLG twisted bilayer graphene

UHB upper Hubbard band

UHV ultra-high vacuum

vdW van der Waals

VB valence band

1 Introduction

Although the Mermin-Wagner theorem states that there should be no long-range order in two dimensions at finite temperatures [1], the experimental isolation of graphene, by Andre Geim and Konstantin Novoselov in 2004, marked a significant milestone in solid-state physics [2]. This discovery, which led to the 2010 Nobel Prize in Physics, not only showed that monolayer graphene could be mechanically isolated, but also established a practical route to study atomic thin flakes of two-dimensional van der Waals (vdW) materials. Using similar exfoliation techniques, other layered materials, such as transition metal dichalcogenide (TMD), can also be thinned down to their 2D limits [3].

While graphene exhibits unique chemical, mechanical, and thermal properties [4, 5, 6], its electronic structure is of principal interest within solid-state physics. Near the charge neutrality point, its low-energy electronic structure obeys a linear dispersion relation and behaves as massless Dirac fermions described by Dirac-like equations in relativistic quantum mechanics [7]. The significance of this Dirac-like behaviour extends beyond the electronic properties of graphene; it establishes graphene and other two-dimensional materials as quantum materials that serve as platforms for exploring exotic quantum effects, topological phases of matter, and phenomena such as the quantum Hall effect within solid-state systems [8, 9].

1.1 2D vdW heterostructures

The state-of-the-art for achieving unique properties with the two-dimensional (2D) layered material lies in the assembly of 2D vdW heterostructures. These heterostructures are formed by stacking various 2D material sheets atop one another, with the layers held together by weak vdW forces, reminiscent of construction with Lego bricks [10]. Unlike conventional epitaxial growth, which demands strict lattice matching between layers [11], the weak vdW forces at the interface enable the assembly of materials with differing lattice constants, symmetries, and electronic properties [12]. This freedom in design provides high flexibility in creating artificial materials with customised properties [13].

1.1.1 Moiré physics

One of the most interesting phenomena emerging from vdW heterostructures is moiré physics [14, 15]. When two 2D layers with slightly mismatched lattice constants or rotational misalignments are stacked, a moiré pattern naturally forms due to the lattice mismatch [16]. This moiré superlattice introduces a periodic potential and folds the electronic bands into a mini-Brillouin zone, altering the electronic structure and enabling the emergence of new quantum phenomena [17, 18].

The most famous example is twisted bilayer graphene [19]. When the twist angle between the two layers is adjusted to the "*magic angle*" of 1.05°, two flat electronic bands appear near the Fermi energy [20, 21, 22]. These flat bands suppress the kinetic energy and enhance electron-electron interactions, leading to new phases ranging from correlated insulating states [23] to superconductivity [24, 25] when the filling factor is fine-tuned. Additionally, the observation of rotational symmetry breaking known as a nematic phase in twisted bilayer graphene [26] mirrors phenomena observed in high-temperature cuprate and iron-based superconductors [27, 28]. Furthermore, the phase diagram of twisted bilayer graphene, which includes correlated insulating states, superconductivity, and nematic phases, shows high similarities to the phase diagram of high-temperature superconductors. This similarity suggests magic-angle twisted bilayer graphene as a platform for investigating the mechanisms of high-temperature superconductivity.

The success of twist-angle engineering in graphene has inspired similar investigations in other 2D materials, particularly TMDs, where the interplay of moiré patterns with intrinsic spin-valley coupling and strong electron-electron interactions leads to even richer phase diagrams [29]. For example, the emergence of Wigner crystals in WS_2/WSe_2 moiré heterostructures [30], fractional quantum anomalous Hall states in twisted $MoTe_2$ [31], and the moiré Kondo lattice in $MoTe_2/WSe_2$ heterostructures illustrate the vast potential of moiré superlattices to artificially engineer new states of matter.

1.1.2 Proximity effect

A second interesting phenomenon that emerges in 2D vdW heterostructures is the proximity effect. Proximity effects can transfer various properties, including magnetism and superconductivity, across the interface [32]. By assembling different 2D vdW sheets together, new physical properties and functionalities can arise at their interfaces due to interlayer interactions. In 2D heterostructures, these effects become interesting because of their atomically sharp interfaces and weak interlayer bonding.

For instance, the magnetic proximity effect refers to the phenomenon where magnetic properties are induced in a non-magnetic material through its interaction with an adjacent magnetic material. For example, monolayer WSe_2, a 2D non-magnetic semiconductor, demonstrates this effect when placed in proximity to a 2D magnet like CrI_3. The interaction between WSe_2 and CrI_3 induces a valley Zeeman splitting in WSe_2, acting as an exchange field on the

WSe_2 monolayer [33].

When a metal is brought in direct contact with a superconductor, Cooper pairs with their long penetration depth can induce a superconductor in the metal. This effect is known as the superconductor proximity effect [34, 35]. In 2D vdW heterostructure, this effect was demonstrated in the graphene/2H-$NbSe_2$ heterostructure, where graphene, which is a semimetal, acquires superconducting properties through proximity with 2H-$NbSe_2$ [36]. A more interesting example involves the case of monolayer 1T'-WTe_2, which is a quantum spin Hall insulator characterized by helical edge states [37]. When monolayer 1T'-WTe_2 interfaced with superconducting 2H-$NbSe_2$, the proximity effect induces superconductivity at the edge states of 1T'-WTe_2, showing pairing mechanisms that might differ from both the intrinsic superconductivity in 2H-$NbSe_2$ and the induced superconductivity observed in the central regions of 1T'-WTe_2 [38]. We successfully reproduced these results and further investigated the emergence of a robust superconducting pairing gap in 1T'-WTe_2 under the influence of a magnetic field. This superconductor gap is characterized by triplet pairing and resilience to magnetic fields, distinguishing it from the bulk properties of either component [39]. Our observation provided evidence to argue 1T'-WTe_2/2H-$NbSe_2$ heterostructure as a promising platform for realizing one-dimensional topological superconductivity, with potential implications for advancing quantum technologies.

1.1.3 Combination of these two methods

Combining moiré physics and the proximity effect in van der Waals heterostructures opens new opportunities for engineering exotic quantum states. For instance, in the heterostructure of a monolayer ferromagnetic $CrBr_3$ and the van der Waals superconductor 2H-$NbSe_2$, superconductivity can be proximity-induced in $CrBr_3$. However, the introduction of a moiré potential is essential to realize topological superconductivity in such systems [40].

Recently, Eva Andrei's group has reported an interesting case of stacking graphene on 1T-TaS_2. Unlike simple screening effects or trivial co-tunneling mechanisms, the charge modulations in overlying graphene are attributed to periodic band hybridization with underlying 1T-TaS_2, forming a proximity-induced charge density wave (CDW) [41]. Given the moiré periodicity is a powerful knob in tuning vdW heterostructure, a question arises: can the proximity-induced CDW in graphene and its hybridization with 1T-TaS_2 be manipulated by varying the twist angle? In Chapter 6, I address this question by investigating an analogous system of graphene on 1T-$NbSe_2$. By selecting specific twist angles, I explore the interplay between proximity effects and moiré physics, shedding light on the tunability and emergent phenomena in such engineered heterostructures.

1.2 Advantage of local probe technique

Developed in the early 1980s, scanning tunneling microscopy (STM) has granted scientists the powerful ability to visualise and manipulate electronic states on surfaces with atomic

resolution [42, 43, 44]. Beyond topographic imaging, scanning tunnelling spectroscopy (STS) enables spatially resolved measurements of the local density of states, providing direct access to the electronic structure at the atomic scale [45**?**]. These capabilities have been crucial in the study of 2D heterostructures, exemplified by Herbert Kroemer's word that *"the interface is the device"* [46]. Without the interference of capping layers, STM enables direct probing of the interfaces in 2D heterostructures, offering an atomic-level perspective on their structural and electronic properties. By mapping local quantum phenomena, STM reveals details that are often averaged out in macroscopic transport measurements.

For instance, research on magic-angle twisted bilayer graphene has revealed an apparent paradox [47]: transport measurements of magic-angle twisted bilayer graphene reveal delocalisation [23, 26], whereas STM measurements have observed strongly localised states resembling strongly correlated quantum dot lattice behaviour [48, 49]. This apparent paradox highlights the complementary nature of macroscopic transport and microscopic local probe techniques, both of which are essential to unravelling the complexities of novel quantum phenomena. Furthermore, STM enables the manipulation of 2D material properties on the nanoscale; for instance, Katharina J. Franke's group reported controlling charge density wave (CDW) states in 2H-$NbSe_2$ by precisely positioning iron adatoms on the surface and building a chain of iron atoms on 2H-$NbSe_2$ using STM tip, paving the way for the realization of Majorana zero modes [50, 51].

Beyond STM, other local probe methods have also made contributions to the study of 2D materials. Techniques such as scanning nitrogen-vacancy magnetometry have revealed coexisting ferromagnetic and antiferromagnetic states in twisted CrI_3 [52]. In addition, scanning single-electron transistors has been used in observing fractional Chern insulators in magic-angle twisted bilayer graphene [53].

In summary, the application of STM and other advanced local probe techniques, which are fundamental tools for nanotechnology, has enabled researchers to explore the electronic properties of 2D heterostructures (quantum materials) down to the atomic level. This integration bridges the disciplines of nanoscience and quantum materials science together, approaching the new field of quantum nanoscience. This new field is paving the way for the development of next-generation quantum devices and technologies.

1.3 An outline of the thesis

In this thesis, I will present a new sample fabrication method for assembling clean 2D vdW heterostructures compatible with STM measurements. Following this method, this thesis investigates three distinct 2D vdW heterostructure systems (Fig. 1.1), each exhibiting unique electronic phenomena arising from the interplay of proximity effects, moiré superlattices, and correlation physics, including 1T-$NbSe_2$ on 2H-$NbSe_2$ (Fig.1.1a), graphene on 1T-$NbSe_2$/2H-$NbSe_2$ (Fig.1.1b), and CrSBr on 2H-$NbSe_2$ (Fig.1.1c).

In chapter 4, I present a new suspended dry pick-up and flip-over assembly technique aimed at minimizing surface contamination and achieving clean, defect-free interfaces. This

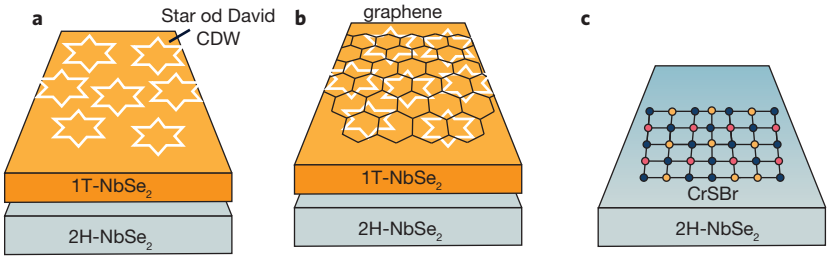

Figure 1.1: **A summary of three 2D vdW heterostructures investigated in this thesis a,** 1T-$NbSe_2$ on 2H-$NbSe_2$,as discussed in chapter 5. **b,** graphene on 1T-$NbSe_2$ on 2H-$NbSe_2$ in chapter 6. **c,** CrSBr on 2H-$NbSe_2$ in chapter 7.

innovative method involves a stepwise assembly process using custom-designed polydimethylsiloxane (PDMS) stamps, followed by a controlled flip-over procedure. By enabling the fabrication of arbitrary designer heterostructures while preserving pristine surface conditions, this assembly technique becomes essential for the highly surface-sensitive STM measurements explored in the subsequent chapters of this thesis.

Next, in chapter 5, I explore the proximity-induced doped Mott physics in heterostructures of 1T-$NbSe_2$ and 2H-$NbSe_2$. While the 2H phase exhibits metallic and superconducting behaviours accompanied by a 3×3 CDW modulation, the 1T phase forms a $\sqrt{13} \times \sqrt{13}R13.9°$ CDW characterized by star of David (SoD) clusters. The relatively large Coulomb interaction within each SoD clusters compared to the hopping between the clusters results in correlated electronic properties. By applying voltage pulses to 2H-$NbSe_2$ bulk sample, we successfully induced a local phase transition to 1T-$NbSe_2$ on 2H-$NbSe_2$. Using STM, I found a spatially inhomogeneous electronic landscape driven by the interplay of Kondo coupling and charge transfer. This chapter finds out the incommensurate stacking order between 3×3 CDW in 2H-$NbSe_2$ and $\sqrt{13} \times \sqrt{13}$ CDW in 1T-$NbSe_2$ causes the spatially inhomogeneous electronic structure. The resulting electronic structure varies on the nanometer scale, transitioning from an insulator-like behaviour to a metallic-like behaviour, highlighting the richness of correlated phenomena in this heterostructure.

In Chapter 6, I focus on engineering a periodic modulation of graphene by stacking it on 1T-$NbSe_2$/2H-$NbSe_2$. By tuning the twist angle, I realized two near-commensurate superlattices with $\sqrt{3} \times \sqrt{3}$ and 2×2 periodicity in respect to CDW of 1T-NbSe2. Using STM and STS I visualized local stacking configurations for these two superlattices. I applied a newly developed symmetry analysis method, which is detailed in section 2.4 of chapter 2, to track rotational symmetry breaking as a function of bias. In the 2×2 superlattice, C_3 rotational symmetry was preserved. However, in the $\sqrt{3} \times \sqrt{3}$, a strong stripe phase with C_2 rotational symmetry occurs. Our theoretical collaborator Dr. Lennart Klebl, conducted density functional theory (DFT) calculation and built tight-binding models to explain this symmetry breaking. Our findings highlight a mechanism for superlattice-induced symmetry breaking that might lead to the creation of exotic states of matter.

Finally, in Chapter 7, I explore the electronic properties of CrSBr on 2H-$NbSe_2$. CrSBr is a

quasi-one-dimensional magnetic semiconductor with highly anisotropic conduction bands. I identified two localized electronic states along its easy axis, corresponding to two conduction bands with flat dispersions predicted along the $\Gamma \rightarrow X$ direction. Applying an out-of-plane magnetic field modifies the band dispersion, causing these flat bands to disappear while inducing a conduction band with flat dispersion along the $\Gamma \rightarrow Y$ direction. Although I do not observe clear evidence for moiré patterns or in-gap states which would signal strong coupling between CrSBr and 2H-$NbSe_2$, the quasi-particle interference patterns hint at spin excitations potentially coupled with other quasi-particles. Furthermore, by tunnelling through CrSBr into 2H-$NbSe_2$, I observe the superconducting gap where I am able to image Abrikosov vortex states under an applied magnetic field. While this study remains in its early stages, these findings lay the groundwork for deeper investigations of the interplay between 2D magnetism and superconductivity in such heterostructures.

2 Theoretical background

2.1 Local magnetic moment on surface

Magnetic impurities on surfaces are interesting because they host unpaired local spins that give rise to classical magnetic moments and are drivers of complex quantum phenomena, such as entanglement. One prominent manifestation of these quantum effects is the Kondo effect, observed when magnetic adatoms are introduced onto a metal surface. Historically, the study of magnetic impurities was constrained by their atomic-scale size, requiring ensemble-based macroscopic measurements such as transport measurements.

In a normal conducting metal, resistivity typically decreases as the temperature is lowered, a consequence of reduced phonon scattering, before plateauing at a residual value due to static defect scattering [56] (Fig. 2.1a). However, the presence of magnetic impurities disrupts this trend. Instead of further decreasing, the resistivity anomalously increases at low temperatures [57] (Fig. 2.1a).

This anomalous behaviour was theoretically explained by Jun Kondo [58, 59, 54], who attributed it to the interaction between the localised spins of magnetic impurities and the itinerant electrons in the underlying metal. This interaction exhibits a temperature-dependent nature. At temperatures above the Kondo temperature ($T > T_K$), the local magnetic moment remains unscreened, representing the weak coupling regime. In contrast, at temperatures below the Kondo temperature ($T < T_K$), the system enters the strong coupling regime, where perturbation theory fails. In this regime, conduction electrons screen the impurity spin, forming a nonmagnetic many-body Kondo singlet state. This state gives rise to a sharp resonance near the Fermi energy in the electronic density of states, a defining feature of the Kondo effect (Fig. 2.1b).

2.1.1 Measure Kondo effect by the local probe method

The advent of local probing techniques, such as STM and STS, provides a new microscopic insight into the Kondo effect by enabling investigations at the nanometer scale. These tools enable the direct, spatially resolved study of the electronic structure of individual magnetic

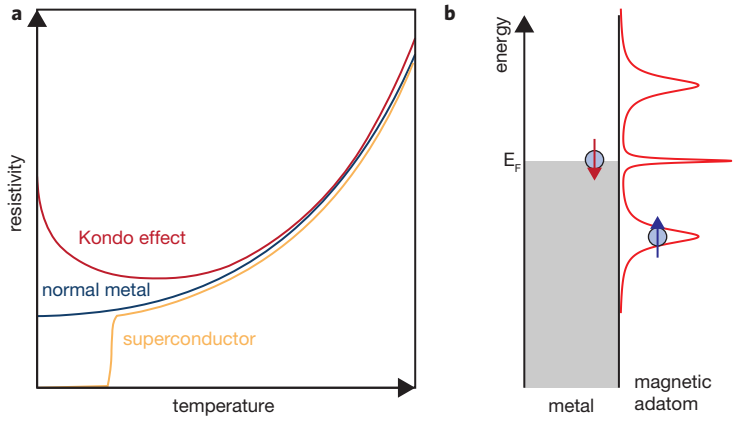

Figure 2.1: **Schematic of the Kondo effect. a,** Macroscopic behaviour of low-temperature transport. In a superconductor, resistivity drops to zero below the critical temperature. In a normal metal, resistivity decreases with decreasing temperature. When a magnetic adatom is introduced to the surface of a normal metal, an anomalous increase in resistivity emerges at low temperatures, signalling the Kondo effect (adapted from ref. [54]) **b,** Microscopic schematic of the Kondo effect. The characteristic Kondo resonance peak appears in the density of states near the Fermi energy. This feature arises from spin-flip scattering between the localized magnetic moment hosted by the magnetic adatom and the itinerant electrons in the metal (adapted from ref. [55]).

adatoms on surfaces [60, 61].

Unlike the idealised schematic peak illustrated in Fig. 2.1b, the experimentally recorded $\mathrm{d}I/\mathrm{d}V$ spectra for magnetic adatoms on metallic surfaces exhibit more asymmetric lineshapes. These deviations arise from the complex tunnelling processes occurring between the metallic probing tip and the sample, which involve multiple conduction pathways (Fig. 2.2a).

The first pathway (path 1) involves electrons tunnelling directly from the metallic tip into the metallic substrate, resulting in a continuous feature in the local density of states (LDOS) spectrum. The second pathway (path 2) occurs when electrons tunnel into the Kondo resonance near E_F, producing a discrete spectral feature localised close to E_F. Additionally, a third process (path 3) involves indirect tunnelling via a spin-flip transition into the hybridised and localised state of the magnetic adatom.

Among the tunnelling processes involved in scanning tunnelling microscopy measurements of the Kondo effect, two key pathways, including direct tunnelling to the substrate (path 1) and tunnelling via the discrete Kondo resonance states (path 2), conserve the spin of the tunnelling electrons and play a crucial role in shaping the observed $\mathrm{d}I/\mathrm{d}V$ spectrum. The tunnelling current, as a coherent quantum process, is influenced by the quantum interference between these two pathways. This interplay between the continuous states associated with direct tunnelling (path 1) and the discrete Kondo resonance states (path 2) gives rise to the characteristic Fano-like lineshapes observed in the experimental spectrum (Fig. 2.2b).

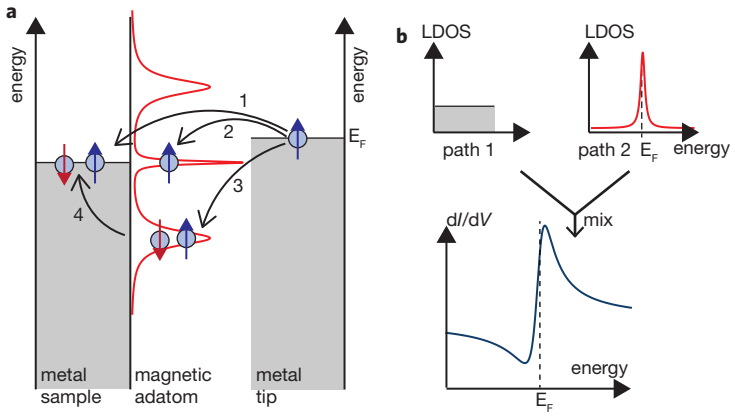

Figure 2.2: **Local probing of the Kondo effect. a,** Electrons from the STM tip can tunnel directly into the empty states of the sample via path 1 or into the Kondo resonance via path 2, with both processes conserving electron spin. A third process involves an indirect transition via spin-flip scattering on the magnetic adatom through path 3 (adapted from ref. [55]). **b,** The interference between tunnelling paths 1 and 2 leads to a Fano-like lineshape in the dI/dV spectrum.

The tunnelling matrix element for path 1, denoted as t_1, is a constant and is given by

$$t_1 = -\frac{1}{1-iq} \tag{2.1}$$

where q is a real number, representing a parameter whose physical interpretation will be discussed later. The tunnelling matrix element for path 2, denoted as t_2 depends on the energy alignment with the Kondo resonance energy E_K and is expressed as:

$$t_2 = \frac{1}{1+i\epsilon}. \tag{2.2}$$

Here, ϵ describes the energy offset from the Kondo resonance, normalized by the resonance width, such that

$$\epsilon = \frac{E - E_\mathrm{K}}{\Gamma},$$

where Γ represents the half-width at half-maximum of the Kondo resonance. The amplitudes of the two tunnelling paths are given by

$$|t_1|^2 = \frac{1}{1+q^2} \tag{2.3a}$$

$$|t_2|^2 = \frac{1}{1+\epsilon^2} \tag{2.3b}$$

The amplitude of path 1 is constant across the energy spectrum, manifesting as a horizontal line in the LDOS spectrum (equation 2.3a), whereas the amplitude of path 2 forms a Lorentzian-shaped peak centred at E_K, with its width determined by Γ (equation 2.3b). The interference

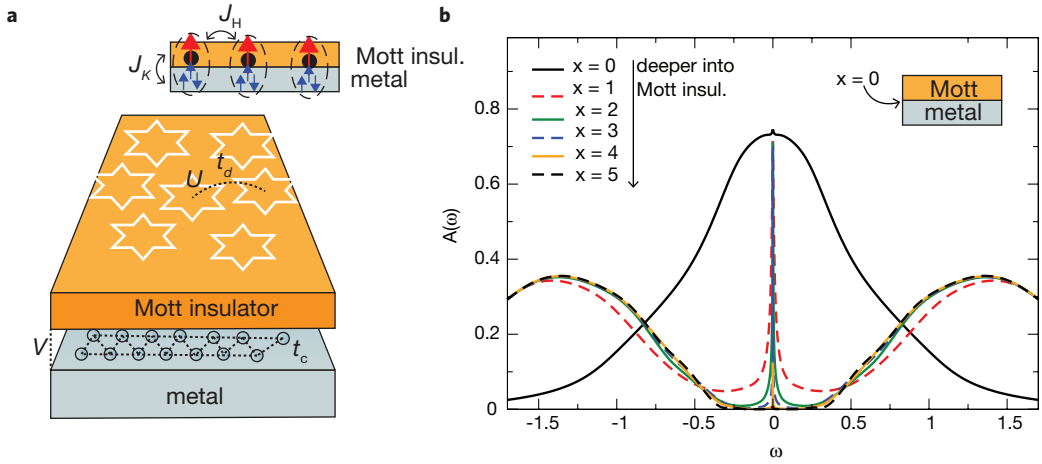

Figure 2.3: **Modelling Mott insulator on metal. a,** Schematic illustration of the Mott insulator (orange) on metal (cyan), where t_d is nearest-neighbour hopping and U represents the on-site Hubbard interaction in the Mott insulator; t_d is nearest-neighbour hopping for the itinerant electrons in the metal. Electrons can tunnel between two layers parameterised by V. The inset shows the competition between the Heisenberg coupling J_H and the Kondo coupling J_K. **b,** Local spectra function $A(\omega)$ for various Mott insulator layers. x = 0 indicates the interface between the Mott insulator and the metal (adapted from ref.[62])

.

between these two tunnelling paths produces the total tunnelling amplitude:

$$
\begin{aligned}
|t_1 + t_2|^2 &= \left| -\frac{1+iq}{1+q^2} + \frac{1-i\epsilon}{1+\epsilon^2} \right|^2 \\
&= \frac{1}{1+q^2} \frac{(q+\epsilon)^2}{1+\epsilon^2}
\end{aligned}
\tag{2.4}
$$

Equation 2.4 describes the Fano lineshape, which arises from the interference of the tunnelling paths. The asymmetry of the lineshape is quantified by the parameter q, with the interplay between the Lorentzian peak (path 2) and the constant background (path 1) determining the Fano resonance profile.

2.2 Kondo effect in heterostructure of Mott insulator and metal

A Mott insulator is a material where strong electron-electron interactions dominate, resulting in an insulating state that breaks classical band theory predictions of metallic behaviour. This insulating nature arises from large Coulomb repulsion between electrons on the same atomic site, effectively localising them and preventing free movement across the lattice. As a result of this strong interaction, Mott insulators exhibit magnetic degrees of freedom associated with the presence of localised spins [62].

When a Mott insulator is interfaced with a metal, two competing interactions dictate the

emergent electronic properties: the Heisenberg coupling (J_H) between the local moments in the Mott insulator and the Kondo coupling (J_K) between the local moments and the itinerant electrons in the metal (Fig.2.3a). Within the Mott insulator layer, the localised electrons maintain magnetic ordering through exchange interactions with neighbouring electrons. However, at the interface, the localised spins couple with the itinerant electrons in the metal, forming Kondo singlets. The first one-dimensional case with weak antiferromagnetic coupling J_H was considered by Doniach [63].

Therefore, the Hamiltonian of this hybridised system needs to combine the Anderson model with the Hubbard model:

$$\begin{aligned} H = &- t_d \sum_{\langle i,j\rangle,\sigma} d^{\dagger}_{i,\sigma} d_{j,\sigma} + \sum_i n_{d,i}\left(\epsilon^{(0)}_d - \mu_F\right) - t_c \sum_{\langle i,j\rangle,\sigma} c^{\dagger}_{i,\sigma} c_{j,\sigma} + \sum_i n_{c,i}\left(\epsilon^{(0)}_c - \mu_F\right) \\ &+ \frac{U}{2}\sum_i \left(n_{d,i}-1\right)^2 - V\sum_{i,\sigma}\left(c^{\dagger}_{i,\sigma} d_{i,\sigma} + \text{H.c.}\right), \end{aligned} \tag{2.5}$$

where electrons created by the operator $c^{\dagger}$ are the itinerant electrons and electrons created by the operator $d^{\dagger}$ represent the correlated electrons [64]. This model has two limits: first when the correlated electrons are entirely localized, $t_d = 0$, equation 2.7 reduces to the periodic Anderson model, and when $V = 0$, equation 2.5 can decouple to a Hubbard model for describing the Mott insulator and a tight-binding model for the metal [64].

Solving this 2D many-body Hamiltonian needs some approximations. The common method is to apply the Slave rotor method, the correlated electron can be separated by a local charge θ_i and an auxiliary fermion $f_{i,\sigma}$:

$$d_{i,\sigma} \equiv e^{i\theta_i} f_{i,\sigma}. \tag{2.6}$$

By setting constraints on the thermal fluctuation with $n_{\theta,i} + n_{f,i} = 1$. The Hamiltonian can be reduced to:

$$\begin{aligned} H = &- t_d \sum_{\langle i,j\rangle,\sigma} \exp\left(-i\theta_i\right)\exp\left(i\theta_j\right) f_{i,\sigma} f_{j,\sigma} + \sum_i n_{f,i}\left(\epsilon^{(0)}_d - \mu_F\right) - t_c \sum_{\langle i,j\rangle,\sigma} c^{\dagger}_{i,\sigma} c_{j,\sigma} \\ &+ \sum_i n_{c,i}\left(\epsilon^{(0)}_c - \mu_F\right) + \frac{U}{2}\sum_i n^2_{\theta,i} - V\sum_{i,\sigma}\left(c^{\dagger}_{i,\sigma}\exp\left(i\theta_i\right) + \text{H.c.}\right) \end{aligned} \tag{2.7}$$

Even with the approximations, solving this Hamiltonian remains a challenging task, necessitating the application of the dynamic mean field theory. An important insight from Ref.[62] is that despite the large charge gap in the Mott insulator, which is typically on the order of the local Coulomb repulsion U and suppresses direct electronic tunnelling, a new tunnelling channel emerges through resonant spin-flip scattering. This mechanism, driven by the Kondo effect, enables conduction electrons from the metallic layer to interact with localised spins in the Mott insulator. This Kondo coupling manifests in the layer-dependent local spectral function of the Mott insulator (Fig. 2.3b). At the interface with the metal, the LDOS reflects the metallic character, showing a large LDOS around the Fermi energy. As one moves deeper into

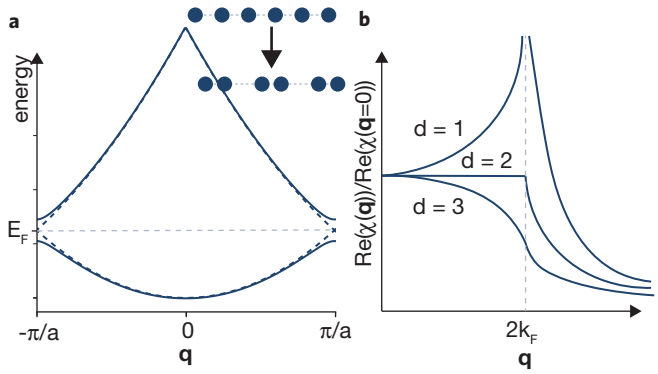

Figure 2.4: **Formation of one-dimensional CDW. a,** Band structure in the presence of a weak 1D periodic potential. The dotted line shows the band structure without potential. Inset panel: the geometry of the one-dimensional chain lattice undergoes dimerisation. **b,** Lindhard response function as a function of wavevector **q**. In one dimension, the Lindhard response function exhibits a divergence at the Fermi surface ($\mathbf{q} = 2\mathbf{k}_F$), indicating a weak-coupling instability of a one-dimensional chain toward CDW order, known as the Peierls instability. In contrast, for dimensions higher than one (d>1), the Lindhard response function does not exhibit such a divergence. As a result, there is no weak coupling instability to CDW formation. (replotted from ref.[65])

the Mott insulator, the spectral features transition, with the LDOS being dominated by a sharp peak centred at zero bias, characteristic of the Kondo resonance.

2.3 Charge density waves

Charge density waves (CDWs) are characterised by the periodic modulation of electronic charge density within a crystal lattice. Fundamentally, a CDW is a collective electronic phenomenon that breaks the lattice translational symmetry while preserving time-reversal, spin rotation, and phase symmetries [66, 67, 68]. In this state, any density-like observable—specifically those invariant under operations of time-reversal, spin-rotation, and phase-rotation operations—exhibits a modulation with a periodicity that differs from that of the underlying crystal lattice.

A one-dimensional lattice chain at half-filling is unstable, a phenomenon known as Peierls instability [69]. Peierls demonstrated that a one-dimensional chain can lower the energy by undergoing a periodic lattice distortion that doubles the unit cell, thereby opening a gap at the Fermi level. This distortion leads to the formation of a CDW, where the electronic charge density becomes modulated with a periodicity that is twice that of the underlying lattice (Fig. 2.4a). Peierls instability can be understood by the linear response theory. In this theory, the electron gas density $\rho(\mathbf{r})$ to external perturbations $\psi(\mathbf{q})$ is given by

$$\rho(\mathbf{r}) = \chi(\mathbf{q})\phi(\mathbf{q}),$$

where $\chi(\mathbf{q})$ is known as the Lindhard response function. The Lindhard response function

characterizes the susceptibility of the electron gas to perturbations at different wave vectors $\mathbf{q}$. Its imaginary part is [70]

$$\Im\big(\chi(\mathbf{q})\big) = \int \frac{d\mathbf{k}}{(2\pi)^d} \left(f_{\mathbf{k}} - f_{\mathbf{k}+\mathbf{q}}\right) \delta\left(\epsilon_{\mathbf{k}} - \epsilon_{\mathbf{k}+\mathbf{q}}\right), \tag{2.8}$$

and the real part is

$$\Re\left(\chi(\mathbf{q})\right) = \int \frac{d\mathbf{k}}{(2\pi)^d} \frac{f_{\mathbf{k}} - f_{\mathbf{k}+\mathbf{q}}}{\epsilon_{\mathbf{k}} - \epsilon_{\mathbf{k}+\mathbf{q}}}. \tag{2.9}$$

In these two equations, $f_{\mathbf{k}}$ is the Fermi function, and $\epsilon_{\mathbf{k}}$ is the Fermi energy. The real part of the $\epsilon_{\mathbf{k}}$ characterises the stability of the system against charge density modulations at wave vector $\mathbf{q}$. Figure 2.4b shows the real part of Lindhard response function $\Re\big(\chi(\mathbf{q})\big)$ for dimensions $d = 1, 2$ and 3 at zero temperature. In one dimension ($d = 1$), $\Re\big(\chi\left(\mathbf{q}\right)\big)$ diverges when $\mathbf{q} = 2\mathbf{k}_F$. This divergence results from the denominator approach to zero over a finite domain as $\epsilon_{\mathbf{k}} = \epsilon_{\mathbf{k}+\mathbf{k}_F}$ in equation 2.9. This particular condition $\epsilon_k = \epsilon_{k+k_F}$ is known as perfect nesting [65, 71]. Perfect nesting occurs when large portions of the Fermi surface can be mapped onto other portions by a single CDW vector q_{CDW}. Consequently, this condition enhances the electronic susceptibility and drives the Peierls instability.

In contrast, for the higher dimensions ($d > 1$), the real part of the Lindhard response functions $\Re(\epsilon_k)$ does not exhibit such divergence. Therefore, the perfect nesting condition is not typically satisfied in higher-dimensional systems. To extend the Peierls picture to higher dimensions, the formation of CDW requires distortions of the Fermi surface that promote partial nesting. At the partial nesting condition, both the real and imaginary parts of the Lindhard response function $\chi(\mathbf{q})$ derived from the measured band structure, should exhibit peaks structure at the CDW wave vector q_{CDW} [70].

The formation of the CDW in the real system is more complex due to the presence of multiple bands, electron-electron interactions, and atomic defects. Specially in the family of TMD layered material, various polytypes such as hexagonal structure (H-phase) and trigonal structure (T-phase) exhibit various crystal structures and various CDW patterns, each with unique formation mechanism and characteristics [72].

Importantly, 2H-$NbSe_2$ exhibits a 3×3 CDW phase around 30 K, which coexists with superconductivity at lower temperatures. The mechanism driving the CDW into the 2H phase is still a topic of debate. Measurements on monolayer $NbSe_2$ in H-phase indicate that electron-phonon coupling plays a significant role in the formation of CDW than Fermi surface nesting [73, 74]. Typically, the energy scales associated with the Peierls instability and the electron-phonon coupling lie within a few multiples of the thermal energy ($k_{\mathrm{B}}T$) from the Fermi energy meaning that only states near the Fermi level are related to the formation of the CDW.

However, the observation of the CDW phase occurs at higher energy scales [75]. This discrepancy is significant, as it exceeds the energy predicted by both the Peierls mechanism and electron-phonon coupling theories, which generally rely on Fermi surface nesting and interactions near the Fermi level. To explain the energy scale deviation, it is proposed that strong coupling between the electrons and the lattice drives 2H-$NbSe_2$ for the formation of

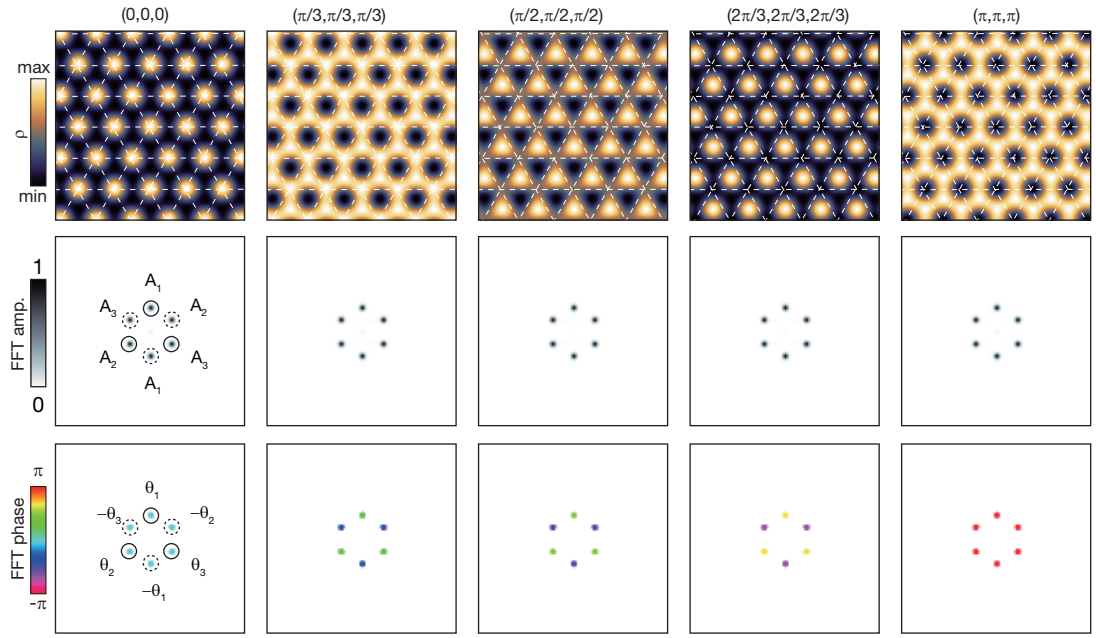

Figure 2.5: **Simulation of a triangular lattice corresponding to the different form factors with preserving C_3 rotational symmetry.** Top row: simulated grids in real space. Middle row: corresponding FFT amplitude patterns. Bottom row: corresponding FFT phase patterns. The form factors have identical magnitudes but exhibit varying phases.

the CDW.

2.4 Extraction of the form factor

In this section, we introduce a tool to analyse the rotational symmetry breaking observed in the STS grids, which will be further applied in Chapter 6. To illustrate the fundamental principles involved, we first consider one-dimensional CDW modulating the LDOS $\rho(\mathbf{r})$ in real space. This modulation can be described as a plane wave function with a finite background ρ_0, as follows [65, 76]:

$$\rho_i(\mathbf{r}) = A_i \cos(\mathbf{Q}_i \cdot \mathbf{r} + \theta_i) + \rho_0 = \Re\left(\psi_i \exp(i\mathbf{Q}_i \cdot \mathbf{r}_i)\right) + \rho_0, \tag{2.10}$$

where A_i scales the amplitude of the modulation, θ_i is the phase, and $\mathbf{Q}_i$ is the reciprocal vector of the CDW superlattice. Thus, the modulation of the CDW can be further expressed as the complex form factor $\psi_i = A_i \exp(i\theta_i)$ multiplied by a plane wave function $\exp(i\mathbf{Q}_i \cdot \mathbf{r})$ [66].

In 2D systems, when a CDW forms a triangular superlattice, the charge modulation occurs along three equivalent directions defined by the reciprocal vectors $\mathbf{Q}_1$, $\mathbf{Q}_2$, and $\mathbf{Q}_3$ known as triple $\mathbf{q}$-CDW [72]. These vectors are equivalent in magnitude and separated by 120°. Consequently, the charge modulation in the system can be expressed by the superposition of

three plane waves with their respective form factors $\{\psi_1, \psi_2, \psi_3\}$ [77]:

$$\rho(\mathbf{r}) = \sum_{i=1}^{3} \rho_i + \rho_0 = \sum_{i=1}^{3} \Re\left(\psi_i \exp(i\mathbf{Q}_i \cdot \mathbf{r})\right) + \rho_0, \tag{2.11}$$

We start from the cases where all three complex form factors have identical magnitudes and phases. The resulting simulated real-space grids are shown in the top row of Fig. 2.5. Given that the magnitudes are identical, the form factors can be characterised by their phases $\{\theta_1, \theta_2, \theta_3\}$. Each set of phases corresponds to a unique real-space pattern, where the modulation maxima are located at different positions. To extract the form factors from STS grids or the simulated grids, two methods can be used. The first method is to fit the STS grids by minimizing the difference between the observed STS grdis and the equation 2.11 [77, 78]:

$$\min_{\{\psi_1,\psi_2,\psi_3\}} \left(\mathrm{STS} - \rho\left(\psi_1, \psi_2, \psi_3\right)\right)^2.$$

The second method is to apply the Fourier transformation to equation 2.11:

$$\hat{\rho}(\mathbf{k}) = \int d\mathbf{r} \exp(-i\mathbf{k}\cdot\mathbf{r})\, \rho(\mathbf{r}) = \sum_{i=1}^{3} \Re\left(\int d\mathbf{r}\, \psi_i \exp(i(\mathbf{Q}_i - \mathbf{k})\cdot\mathbf{r})\right) = (2\pi)^2 \sum_{i=1}^{3} \Re(\psi_i)\delta(\mathbf{Q}_i - \mathbf{k}). \tag{2.12}$$

This Fourier transformation indicates that the form factors can be extracted at the corresponding Bragg peaks in the reciprocal space. In practice, the extraction of the form factors from the fast Fourier transform (FFT) of STS grid [79]:

$$\psi_i = \int_{\mathbf{k}\in P(\mathbf{Q}_i)} d\mathbf{k} \int d\mathbf{r} \exp(-i\mathbf{k}\cdot\mathbf{r})\ \mathrm{STS}(\mathbf{r})\ w(\mathbf{r}), \tag{2.13}$$

where $\omega(\mathbf{r}) = \exp\left(-\mathbf{r}^2/2R^2\right)$ is a Gaussian window function and $P(\mathbf{Q}_i)$ represent appropriately sized square area around Bragg spot $\mathbf{Q}_i$. The form factors extracted using the Fourier transformation are decomposed into their magnitude and the phase shown in the middle row and the bottom row of Fig. 2.5. In the FFT phase images, the colour of each pixel represents the phase of the FFT patterns, while their brightness indicates their magnitude. For clarity, pixels with magnitudes smaller than 10% are filtered out. The uniform colour around the Bragg peaks indicates that the phase takes on a constant value within each peak.

The FFT magnitude and phase patterns reveal six Bragg spots forming a hexagonal pattern. To simplify the analysis, we use the conjugate symmetry (Hermitian symmetry) of the FFT image. This Hermitian symmetry indicates that the FFT image satisfies

$$\mathrm{FFT}(k_x, k_y) = \overline{\mathrm{FFT}}(-k_x, -k_y),$$

where (k_x, k_y) are the coordinates in the FFT image, and $(-k_x, -k_y)$ is the centrosymmetric counterparts. Using this Hermitian symmetry of the FFT, these six Bragg spots can be reduced to three independent spots separated by 120°. Thus, we can assign three spots corresponding to the reciprocal vectors $\mathbf{Q}_i (i = 1, 2, 3)$, as labelled by the solid line circles, and assign the other

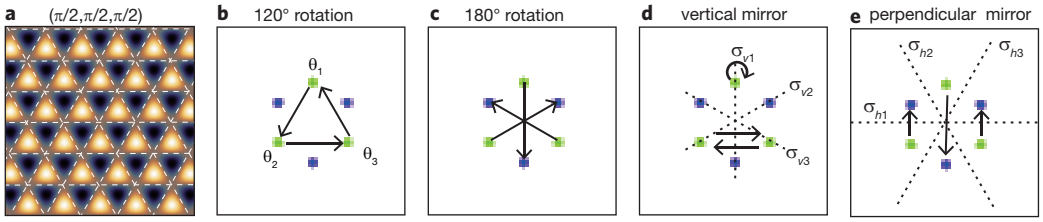

Figure 2.6: **Example of a triangular lattice under the various symmetry operations. a,** simulated grids of $(\pi/2,\pi/2,\pi/2)$ in real space. **b,** the FFT phase under the 120° rotation. **c,** the FFT phase under the 180° rotation. **d**, the FFT phase under the vertical mirror operation, where the black arrows show the mirror operation under the mirror plane of σ_{v1}. **e**, the FFT phase under the perpendicular mirror operation, where the black arrows show the mirror operation under the mirror plane of σ_{h1}.As one can see, this pattern has C_3 rotational symmetry, and the vertical mirror symmetry (σ_{v3}), but breaks the C_2 symmetry and the perpendicular mirror symmetry σ_h.

three spots as their conjugated peaks $G_i^*\,(i=1,2,3)$ labelled by the dashed line circle.

2.4.1 Form factors under the symmetry operations

After establishing the method to extract the form factors, we analyse the form factors under the $2\pi/3$ rotation, π rotation and mirror operation. First, under a rotation of $2\pi/3$ in the real space, the $\rho(\mathbf{r})$ transforms to $\rho(\mathbf{R}(\mathbf{2\pi/3})\mathbf{r})$ as follows:

$$\rho\left(\mathbf{R}(2\pi/3)\mathbf{r}\right)=\sum_{i=1}^{3}\Re\left(\psi_i\exp\left(i\mathbf{Q}_i\cdot\mathbf{R}(2\pi/3)\mathbf{r}\right)\right)+\rho_0, \tag{2.14}$$

with $\mathbf{R}(2\pi/3)$ is the rotation operator. Given that $\mathbf{Q}_i\cdot\mathbf{R}(2\pi/3)$ rotates the G_i vectors by $-2\pi/3$, the reciprocal vectors permute as $\mathbf{Q}_1\rightarrow\mathbf{Q}_2$, $\mathbf{Q}_2\rightarrow\mathbf{Q}_3$ and $\mathbf{Q}_3\rightarrow\mathbf{Q}_1$, Substituting these permutations into equation 2.14 gives

$$\begin{aligned}\rho\left(\mathbf{R}(2\pi/3)\mathbf{r}\right)=&\Re\left(\psi_1\exp\left(i\mathbf{Q}_2\cdot\mathbf{r}\right)\right)+\Re\left(\psi_2\exp\left(i\mathbf{Q}_3\cdot\mathbf{r}\right)\right)\\&+\Re\left(\psi_3\exp\left(i\mathbf{Q}_1\cdot\mathbf{r}\right)\right)+\rho_0.\end{aligned} \tag{2.15}$$

Equation 2.15 demonstrates that $2\pi/3$ rotation results in the permutation of the form factors: $\psi_1\rightarrow\psi_2$, $\psi_2\rightarrow\psi_3$ and $\psi_3\rightarrow\psi_1$, as shown in Fig. 2.6b. If the symmetry preserves the C_3 rotational symmetry, the LDOS must satisfy $\rho(\mathbf{r})=\rho(R(2\pi/3)\mathbf{r})$. This symmetry condition implies that all three form factors must be equal in magnitude and phase $\psi_1=\psi_2=\psi_3$. All the form factors shown in Fig. 2.5 satisfy this relationship, thus they all have the C_3 rotational symmetry.

Next, consider the rotation of π, the $\rho(\mathbf{r})$ transforms as follows:

$$\rho\left(\mathbf{R}(\pi)\mathbf{r}\right)=\sum_{i=1}^{3}\Re\left(\psi_i\exp\left(i\mathbf{Q}_i\cdot\mathbf{R}(\pi)\mathbf{r}_i\right)\right)+\rho_0 \tag{2.16}$$

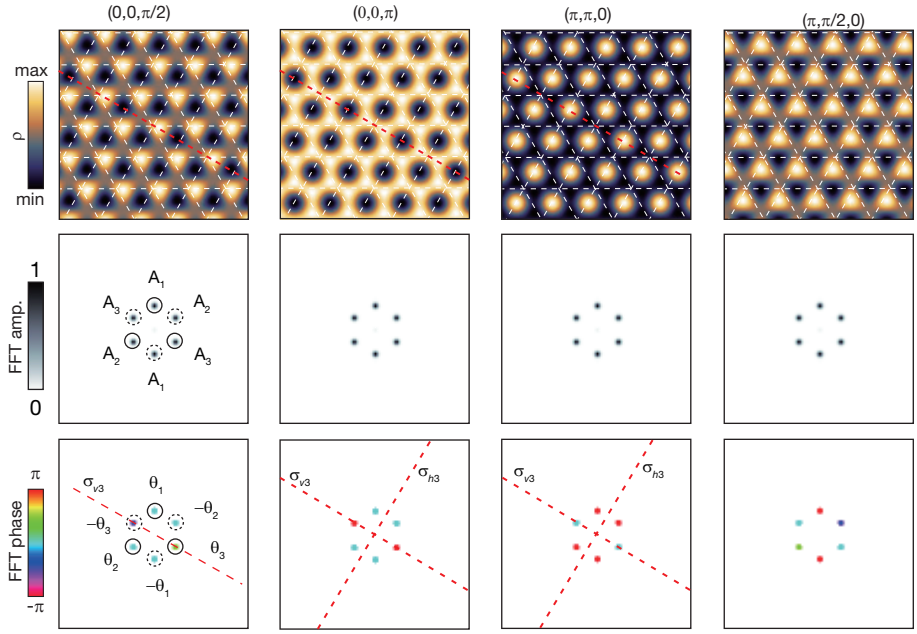

Figure 2.7: **Simulation of a triangular lattice corresponding to the different form factors with C_3 rotational symmetry breaking.** Top row: simulated grids in real space. Middle row: corresponding FFT amplitude patterns. Bottom row: corresponding FFT phase patterns. The form factors have identical magnitudes but exhibit varying phases.

Using the fact that $\mathbf{R}(\pi)r$ transforms the $\mathbf{r}$ to $-\mathbf{r}$ gives:

$$\begin{aligned}\rho\left(\mathbf{R}(\pi)\mathbf{r}\right)=\rho\left(-\mathbf{r}\right)&=\sum_{i=1}^{3}\Re\left(\psi_i\exp\left(-i\mathbf{Q}_i\cdot\mathbf{r}_i\right)\right)+\rho_0\\&=\sum_{i=1}^{3}\Re\left(\psi_i^*\exp\left(i\mathbf{Q}_i\cdot\mathbf{r}_i\right)\right)+\rho_0.\end{aligned}\tag{2.17}$$

Equation 2.17 indicates that applying the π rotation to equation 2.11 transforms the form factors to its complex conjugated: $\psi_i \rightarrow \psi_i^*(i=1,2,3)$ as shown in Fig. 2.6c. If the system preserves the C_2 rotational symmetry, the LDOS must satisfy $\rho(\mathbf{r})=\rho(-\mathbf{r})$. This symmetry condition implies that all three form factors must be 0 or π, as $\psi_i=\psi_i^*$.

Similarly, the vertical mirror operation (σ_v) can be proved to interchange the two form factors, for example, $\psi_2\rightarrow\psi_3$ and $\psi_3\rightarrow\psi_2$ if the vertical mirror operation is applied along σ_{v1} as shown in Fig. 2.6d. We can also prove that the perpendicular mirror operation along σ_{h1}, whose mirror plane is perpendicular to σ_{v1}, transfer $\psi_1\rightarrow\psi_1^*,\psi_2\rightarrow\psi_3^*$ and $\psi_3\rightarrow\psi_2^*$ as shown in Fig. 2.6e.

Figure 2.7 shows the patterns corresponding to three form factors with identical magnitudes but different phases. Similarly, the form factors can be represented by their phases $\{\theta_1,\theta_2,\theta_3\}$, with various sets of phases corresponding to different patterns in the real space of the top row. In the FFT pattern, we have similar hexagon patterns, but the difference is

that after the permutation, the form factors pick up or lose a phase. In such a situation, the C_3 rotational symmetry is not preserved. However, $(0,0,\pi/2)$ preserves the mirror symmetry, and the red dotted line labels the mirror plane in both the pattern in real space and the FFT pattern in reciprocal space. $(0,0,\pi)$ and $(\pi,\pi,0)$ have both mirror symmetry and C_2 rotational symmetry. However $(\pi,\pi/2,0)$ does not preserve either rotational symmetry nor the mirror symmetry.

Table 2.1: **Symmetry operation and the form factors**

Operation	Transformation	Preserving symmetry	Example
C_3	$\psi_1 \rightarrow \psi_2$, $\psi_2 \rightarrow \psi_3$, $\psi_3 \rightarrow \psi_1$	$\psi_1 = \psi_2 = \psi_3$	(0,0,0) $(\pi/2,\pi/2,\pi 2/2)$ (π,π,π)
C_2	$\psi_i \rightarrow \psi_i^*$ $(i = 1,2,3)$	$\theta_i = \pi \quad \text{or} \quad 0$	$(0,0,\pi)$ $(\pi,\pi,0)$
σ_{vi}	$\psi_i \rightarrow \psi_i$, $\psi_j \rightarrow \psi_k$, $\psi_k \rightarrow \psi_j$	$\psi_j = \psi_k$	$(0,0,\pi)$ $(0,0,\pi/2)$
σ_{hi}	$\psi_i \rightarrow \psi_i^*$, $\psi_j \rightarrow \psi_k^*$, $\psi_k \rightarrow \psi_j^*$	$\theta_i = 0 \quad \text{or} \quad \pi$, $\psi_j = \psi_k^*$,	$(0,0,\pi)$ $(0,-\pi/2,\pi/2)$

The relation between the form factors and the symmetry operations of C_3, C_2 and σ is summarised in the table 2.1. This relation can help us identify the symmetry of the real system with the form factors.

3 Experimental setup: Scanning tunnelling microscopy measurement

All the measurements in this thesis were conducted using a commercial STM from Scienta Omicron (POLAR SPM LAB). The system operates in ultra-high vacuum (UHV) conditions of $\approx 1.0 \times 10^{-10}$ mbar and at low temperatures. For the experiments described in Chapter 5 and Chapter 6, the temperature reached 6.5 K. After upgrading the 1K pot, the machine could achieve 1.4 K for the experiments in Chapter 7. This chapter covers the fundamental principles of STM and provides details on our STM setup.

3.1 Basic principles of scanning tunnelling microscopy

The scanning tunnelling microscope is a tool for imaging nanostructures at the atomic level based on the principles of quantum tunnelling. As shown in Fig. 3.1a, when a conductive tip is brought very close to a sample on the order of Ångströms ($\sim 1 \times 10^{-10}$ m), a bias voltage V applied between the tip and the sample allows electrons to tunnel through the vacuum gap of width (z), which is the distance between the tip and the sample. The resulting tunnelling current (I) satisfies the following relation: [81]

$$I(z) \sim e^{-2\kappa \cdot z}. \tag{3.1}$$

Here, κ is the decay constant, which depends on the work function of the tip Φ_{T} and the sample Φ_{S}. It is expressed as:

$$\kappa = \sqrt{\frac{m_0}{\hbar}(\Phi_{\mathrm{T}} + \Phi_{\mathrm{S}} - eV_T)}, \tag{3.2}$$

where eV_T represents the trapezoidal tunnelling barrier potential. For simplicity, we assume the work functions of the tip and sample are equal ($\Phi = \Phi_{\mathrm{T}} = \Phi_{\mathrm{S}}$) and that $eV_T = 0$. This reduces the decay constant to:

$$\kappa = \sqrt{\frac{2m_0\Phi}{\hbar}} \tag{3.3}$$

Given that the work function of most metals lies in the range of $4-5$ eV, κ typically has a value of approximately $1\,\text{Å}^{-1}$ [43]. This results in an extremely high sensitivity of the tunnelling current to the tip-sample distance, such that a change in the distance by just 1 Å leads to

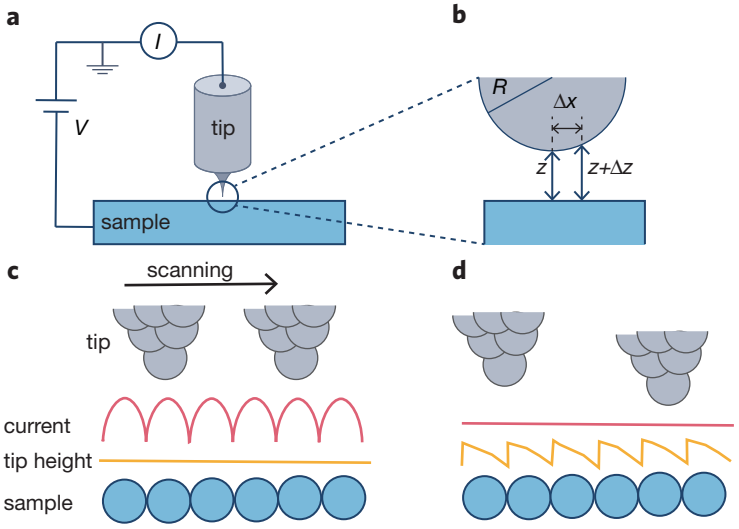

Figure 3.1: **STM operating principle. a,** A schematic view of the STM. **b,** Zoom-in image of the tunnelling junction. **c,** Schematic of constant height scanning mode. **d,** Schematic of constant current scanning probe. Due to the delay of the feedback loop to sudden changes, the tip height signal in constant current mode may differ slightly from the current signal in constant height mode. (revised from Ref.[80]).

an approximate change in the tunnelling current by a factor of e^{-2}. This sensitivity is a fundamental principle underlying STM's capability to resolve atomic-scale features down to roughly 0.1 nm.

Typically, an STM can image surface topography by two scanning modes: constant current mode and constant height mode [82]. Constant height mode (Fig. 3.1c) keeps the bias and tip height fixed while recording the tunnelling current as the tip scans across the surface. In contrast, the constant current mode (Fig. 3.1d) regulates the tunnelling current as a setpoint value by a feedback loop that adjusts the vertical position of the tip height. A topography image can be obtained by recording the vertical position of the tip for each point scanned.

Constant current mode is more commonly used because it is suitable for a wider range of surface topographies, whereas constant height mode is only available for very flat surfaces. In this thesis, most of the topography images were acquired by the constant current mode.

3.2 Theoretical background of scanning tunnelling spectroscopy

Scanning tunnelling spectroscopy (STS) is an extension of STM that provides detailed electronic properties of a surface at the atomic scale with high energy resolution. The energy resolution of STS is fundamentally limited by thermal fluctuations ($3k_BT$). For instance, at 6.5 K, the energy resolution is approximately 1.68 meV, while at 1.4 K, it improves to around 0.36 meV. While STM images the surface topography at a fixed bias voltage, STS involves varying the bias voltage and measuring the resulting differential tunnelling conductance ($\mathrm{d}I/\mathrm{d}V$)

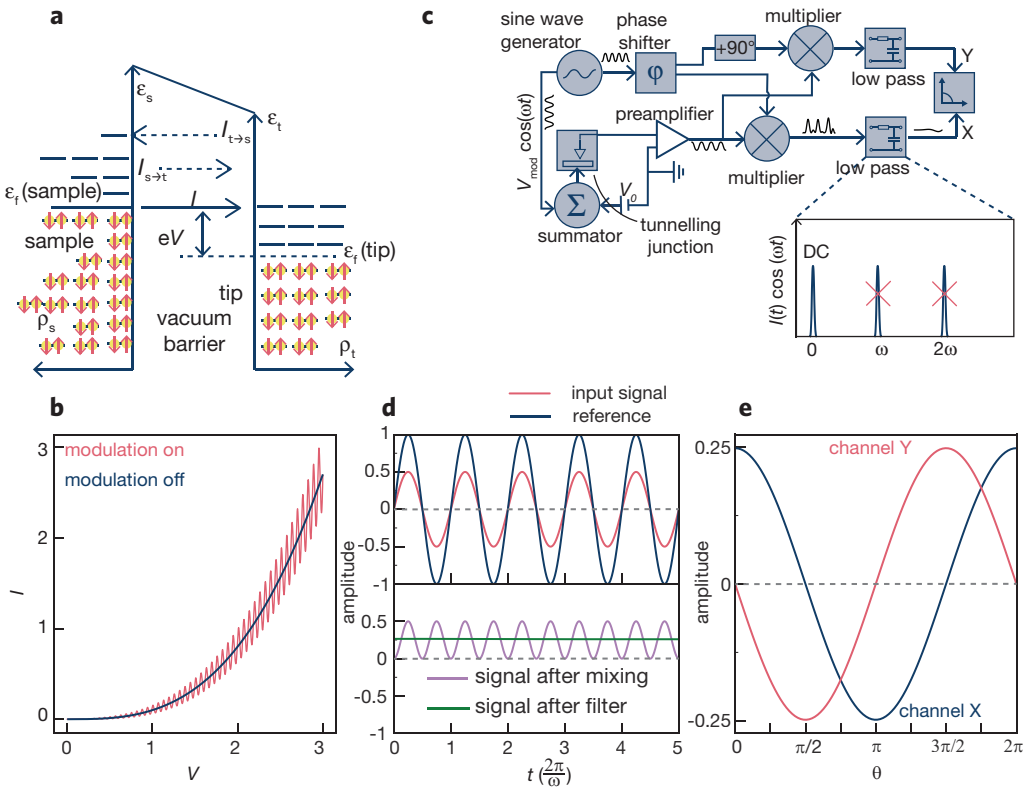

Figure 3.2: **STS operating principle.** **a,** Schematic illustration of the tunnelling process between an ideally metallic tip and a sample in the one-dimensional approximation. **b,** Simulated response of the current $I(V)$ to the applied modulation voltage (red). The modulation in $I(V)$ depends on the slope of the curve. For reference, the blue curve represents $I(V)$ without modulation. **c,** The basic electric circuit of the lock-in amplifier demonstrates both the process of modulation and its corresponding demodulation. **d,** Upper panel: Sinusoidal input signal (red) is multiplied with the reference signal (blue) with the same frequency and same phase. Lower panel: The mixing signal (purple) of the multiply of the input signal and the reference signal with a DC offset and double frequency. After filtering, the green trace, only the DC component remains, which is equal to the in-phase amplitude (X) of the input signal. **e,** The amplitude of the DC signal in channel X (blue) and channel Y (red) as a function of the relative phase θ.

as a function of the bias (V) which is applied to the sample.

3.2.1 Bardeen's approach to tunnelling

To better understand the physical meaning of dI/dV spectroscopy, it is necessary to introduce Bardeen's approach to tunnelling. Bardeen's approach considers the one-dimensional tunnelling process of a single electron between two electrodes, which, in the context of dI/dV spectroscopy, correspond to the probing tip and the sample.

As shown in Fig. 3.2a, the measured tunnelling current $I(V)$ as a function of applied bias V

depends on the difference between the tunnelling rate of electrons from the tip to the sample $I_{s\to t}$ and the reverse tunnelling rate $I_{t\to s}$:

$$I = I_{s\to t} - I_{t\to s}. \tag{3.4}$$

The process of electron tunnelling from the sample to the tip depends on the number of the occupied states in the sample, satisfies the Fermi-Dirac distribution $f_s(\epsilon_s - \epsilon_F^s)$, relative to the Fermi energy ϵ_F^s of the sample. It also depends on the number of unoccupied states in the tip $(1 - f_t(\epsilon_t - \epsilon_F^t))$, with ϵ_F^t the Fermi energy of the tip. For a simplified discussion, I assume the Fermi energy of the tip aligns with the Fermi energy of the sample ($\epsilon_F = \epsilon_F^t = \epsilon_F^s$). Thus, the tunnelling current rate $I_{s\to t}$ is proportional to the product of the occupied density of states in the sample and the unoccupied density in states in the tip as:

$$I_{s\to t} = e\sum_{s,t,\sigma} W_{s\to t} f_s(\epsilon_s - \epsilon_F + eV) \times \left(1 - f_t(\epsilon_t - \epsilon_F)\right), \tag{3.5a}$$

$$I_{t\to s} = e\sum_{s,t,\sigma} W_{t\to s} f_t(\epsilon_t - \epsilon_F) \times \left(1 - f_s(\epsilon_s - \epsilon_F + eV)\right). \tag{3.5b}$$

In these two equations, s(t) labels single-electron states in the sample (tip), $\sigma = \{\uparrow, \downarrow\}$ labels the spin state, and ϵ_F is the Fermi energy. $W_{t\to s}$ and $W_{s\to t}$ correspond to the tunnelling rates of a single electron from the tip to the sample and from the sample to the tip. For simplicity, the spin is assumed to be not flipped during the tunnelling process and $W_{s\to t}$ and $W_{t\to s}$ are independent of the spin. Bardeen's approach further assumes that the tunnelling rate from the tip to the sample and reversely from the sample to the tip are equivalent such that $W_{s\to t} = W_{t\to s} = W_{st}$.

Substituting equation 3.5a, equation 3.5b into the equation 3.4, and replacing $W_{s\to t}$ and $W_{t\to s}$ by W_{st} gives the net tunneling current I:

$$I = e\sum_{s,t,\sigma} W_{st}\left(f_s(\epsilon_s - \epsilon_F + eV) - f_t(\epsilon_t - \epsilon_F)\right). \tag{3.6}$$

This equation reveals that the net tunnelling current is determined by the product of the tunnelling rate W_{st} and the difference in occupation probabilities $\left(f_s(\epsilon_s - \epsilon_F + eV) - f_t(\epsilon_t - \epsilon_F)\right)$ between the sample and the tip, where the occupation probabilities is displaced by the applied bias voltage eV.

The tunnelling rate W_{st} is derived from the Hamiltonian of Bardeen's approach H_B:

$$H_B = H_s + H_t + H_T,$$

where H_s and H_t represent the general Hamiltonians of the sample and tip placed far apart, meaning no coupling between them ($[H_s, H_t] = 0$). Barden's insight into this tunnelling problem is that the tunnelling process is determined by the tunnelling Hamiltonian H_T when the tip and the sample are bought close together. Using Fermi's Golden Rule, the tunnelling rate

W_{st} from the sample to the tip is given by

$$W_{st} = \frac{2\pi}{\hbar}|T_{\mathrm{st}}|^2\delta(\epsilon_{\mathrm{s}} - \epsilon_{\mathrm{t}}) \tag{3.7}$$

where ϵ_{s} (ϵ_{t}) is the energy of the states of the sample (tip), and T_{st} is the tunnelling matrix elements $\langle \mathrm{s}|H_T|\mathrm{t}\rangle$, which represents the probability amplitude for an electron to tunnel from the state $|s\rangle$ in the sample to state $|t\rangle$ in the tip. Barden assumes this term as a constant which does not depend on the energy, allowing it to be represented simply as $T_{\mathrm{st}} = T$.

Plugging equation 3.7 into equation 3.6, considering the spin degeneracy of 2 and replacing the finite summation over the discrete states by an integral over energies using the density of state $\sum_{s,t,\sigma} \rightarrow 2\int d\epsilon_{\mathrm{s}} d\epsilon_{\mathrm{t}} \rho_{\mathrm{s}}(\epsilon_{\mathrm{s}})\rho_{\mathrm{t}}(\epsilon_{\mathrm{t}})$ gives:

$$\begin{aligned} I &= \frac{4\pi e}{\hbar}\sum_{\mathrm{s,t},\sigma}|T|^2\left(f_{\mathrm{s}}(\epsilon_s - \epsilon_F + eV) - f_{\mathrm{t}}(\epsilon_t - \epsilon_F)\right)\delta(\epsilon_{\mathrm{s}} - \epsilon_{\mathrm{t}}) \\ &= \frac{4\pi e|T|^2}{\hbar}\int d\epsilon\left[\rho_{\mathrm{s}}(\epsilon + eV)\rho_{\mathrm{t}}(\epsilon)\left(f_{\mathrm{s}}(\epsilon - \epsilon_F + eV) - f_{\mathrm{t}}(\epsilon - \epsilon_F)\right)\right] \end{aligned}, \tag{3.8}$$

where $\rho_{\mathrm{t}}(\epsilon)$ denotes the density of states in the tip, and $\rho_{\mathrm{s}}(\epsilon)$ corresponds the local density of state underneath the tip.

To reduce the term $\left(f_{\mathrm{s}}(\epsilon - \epsilon_F + eV) - f_{\mathrm{t}}(\epsilon - \epsilon_F)\right)$, Bardeen's approach makes two assumptions: First, both sample and tip are at zero Kelvin, which transforms the Fermi-Dirac distributions to the step functions $f_{\mathrm{s}}(\epsilon - \epsilon_F) = f_{\mathrm{t}}(\epsilon - \epsilon_F) = \theta(\epsilon - \epsilon_F)$. Second, the small energy away from the Fermi energy approximates the difference to the derivation:

$$\begin{aligned} f_{\mathrm{s}}(\epsilon - \epsilon_F + eV) - f_{\mathrm{t}}(\epsilon - \epsilon_F) &\approx \theta(\epsilon - \epsilon_F + eV) - \theta(\epsilon - \epsilon_F) \\ &\approx eV\frac{d\theta(\epsilon - \epsilon_F)}{d\epsilon} \\ &= eV\delta(\epsilon - \epsilon_F). \end{aligned} \tag{3.9}$$

Substituting this zero temperature approximation (equation 3.9) into the equation 3.8 gives:

$$\begin{aligned} I &= \frac{4\pi e^2|T|^2}{\hbar}\int d\epsilon V\delta(\epsilon - \epsilon_F)\rho_{\mathrm{t}}(\epsilon)\rho_{\mathrm{s}}(\epsilon + eV) \\ &= \frac{4\pi e^2|T|^2}{\hbar}V\rho_{\mathrm{t}}(\epsilon_F)\rho_{\mathrm{s}}(\epsilon_F + eV) \end{aligned} \tag{3.10}$$

As a result, the differential conductivity $\mathrm{d}I/\mathrm{d}V$ at the bias V_0 is given by

$$\left.\frac{dI}{dV}\right|_{V_0} \sim \rho_S(\epsilon_F + eV_0)\rho_t(\epsilon_F). \tag{3.11}$$

Equation 3.11 derived from Barden's approach to tunnelling is a key concept to scanning tunnelling spectroscopy because it indicates that the measured differential conductance is proportional to the product of the density of states in the tip and the LDOS in the sample beneath the tip, displaced by the bias voltage from the Fermi energy. As further assuming a

featureless tip around Fermi energy, the measured differential conductivity at a given bias V_0 is directly proportional to the density of states of the sample displaced from the Fermi energy by eV_0:

$$\left.\frac{dI}{dV}\right|_{V_0} \sim \rho_S(\epsilon_F + eV_0) \tag{3.12}$$

3.2.2 Lock-in technique

The intuitive way to obtain the dI/dV spectroscopy involves recording the current-voltage $I-V$ curve at a fixed tip height and subsequently applying the numerical derivative. However, this numerical derivative approach has the drawback of amplifying the noise, which can obscure the subtle features in the signal. To address this issue, lock-in amplifiers are utilised for the dI/dV measurement due to their capability to extract signals from a noisy background [83].

The basic principle of using the lock-in amplifier is as follows: An alternating current (AC) modulation is added to the direct current (DC) bias voltage V_0 by:

$$V(t) = V_0 + V_{\text{mod}} \cos(\omega t). \tag{3.13}$$

Here V_{mod} is the modulation amplitude and ω is the modulation frequency. The tunnelling current $I(t)$ in response to the modulated voltage, shown in Fig. 3.2b, can be expressed on the Taylor series as:

$$\begin{aligned} I(V) &\approx I_0(V_0) + \left.\frac{dI}{dV}\right|_{V_0} (V - V_0) + \mathcal{O}\left((V - V_0)^2\right) \\ &= I_0(V_0) + \left.\frac{dI}{dV}\right|_{V_0} V_{\text{mod}} \cos(\omega t) + \mathcal{O}\left((V - V_0)^2\right), \end{aligned} \tag{3.14}$$

where the first term is the DC term and the second term also known as the first harmonic term corresponds to the dI/dV, while the higher harmonic is proportional to the higher derivative of the current.

The modulated tunnelling current, combined with noise, is input to the lock-in amplifier after passing through the preamplifier. The input signal is denoted as $(I(t) + N(t))$, where $N(t)$ represents the noise. The lock-in amplifier utilizes a dual-phase demodulation circuit as shown in Fig. 3.2c. In this circuit, the input signal is split and separately passed in two multipliers, namely channel X and channel Y. In channel X, the input signal mixes with the reference signal, and results in

$$X(t) = I(t) \cdot V_{\text{ref}}, \tag{3.15}$$

where $V_{\text{ref}} = \cos(\omega t + \theta)$ with θ the phase of the input signal relative to the reference signal. For simplicity, first, let us consider the input signal and reference signal are in the same phase, i.e. $\theta = 0$. The input signal and the reference signal over time is shown in Fig. 3.2d upper panel.

Equation 3.15, which represents the signal in channel X, can be reduced to

$$\begin{aligned} X(t) = I(t)\cos(\omega t) &= \left(I_0 + \left.\frac{dI}{dV}\right|_{V_0} V_{\text{ac}}\cos(\omega t) + N(t)\right)\cos(\omega t) \\ &= I_0\cos(\omega t) + \left.\frac{dI}{dV}\right|_{V_0} V_{\text{mod}}\cos^2(\omega t) + N(t)\cos(\omega t) \\ &= I_0\cos(\omega t) + \left.\frac{dI}{dV}\right|_{V_0}\frac{V_{\text{mod}}}{2} + \left.\frac{dI}{dV}\right|_{V_0}\frac{V_{\text{mod}}}{2}\cos(2\omega t) + N(t)\cos(\omega t) \end{aligned} \quad , \tag{3.16}$$

After mixing with the reference signal, the output of the multiplier signal features a DC off-shift and a component with double frequency (2ω) in channel X. After the low-pass filters, which select the frequencies up to a certain value, is applied, the DC component of the signal will pass in channel X, as shown in Fig. 3.2d lower channel.

For Channel Y, the phase reference signal is shifted by 90°, i.e. $\cos(\omega t + 90°) = \sin(\omega t)$ and the signal after the multiplier is:

$$\begin{aligned} Y(t) = I(t)\sin(\omega t) &= \left(I_0 + \left.\frac{dI}{dV}\right|_{V_0} V_{\text{mod}}\cos(\omega t) + N(t)\right)\sin(\omega t) \\ &= I_0\sin(\omega t) + \left.\frac{dI}{dV}\right|_{V_0}\frac{V_{\text{mod}}}{2}\sin(2\omega t) + N(t)\sin(\omega t). \end{aligned} \tag{3.17}$$

Because channel Y does not involve any DC offset signal component, after applying a low-pass filter, all the signal is filtered out in channel Y except for some noises. To evaluate the noise after passing the low-pass filter, the noise spectrum function is expanded by the Fourier series as:

$$N(t) = \sum_{k=1}^{\infty}\left[A_k\cos(\omega_k t) + B_k\sin(\omega_k t)\right]. \tag{3.18}$$

Since the $\mathrm{d}I/\mathrm{d}V$ signal only passes channel X, here I show the noise analysis in channel X:

$$\begin{aligned} N(t)\cos(\omega t) &= \sum_{k=1}^{\infty}\left[A_k\cos(\omega_k t)\cos(\omega t) + B_k\sin(\omega_k t)\cos(\omega t)\right] \\ &= \sum_{k=1}^{\infty}\left[\frac{A_k}{2}\left(\cos(\omega_k t + \omega t) + \cos(\omega_k t - \omega t)\right)\right] \\ &\quad + \sum_{k=1}^{\infty}\left[\frac{B_k}{2}\left(\sin(\omega_k t + \omega t) + \sin(\omega_k t - \omega t)\right)\right] \end{aligned} \tag{3.19}$$

After applying the low-pass filter, the noise signal is also reduced because only the noise components within the bandwidth of the reference frequency can pass the low-pass filter. Phase sensitivity plays a crucial role in $\mathrm{d}I/\mathrm{d}V$ measurements, as it determines how effectively the lock-in amplifier can isolate the desired signal from noise.

When the relative phase between the input signal and reference is not zero ($\theta \neq 0$), the reference signal becomes $V_{\text{ref}} = \cos(\omega t + \theta)$. This phase difference directly affects the demodu-

lated signal in channel X, introducing a phase shift that can alter the signal's interpretation:

$$\begin{aligned} X(t) &= I(t)\cos(\omega t+\theta) \\ &= \left(I_0 + \left.\frac{dI}{dV}\right|_{V0} V_{\text{mod}}\cos(\omega t) + N(t)\right)\cos(\omega t+\theta) \\ &= I_0\cos(\omega t+\theta) + \left.\frac{dI}{dV}\right|_{V0} V_{\text{mod}}\cos(\omega t)\cos(\omega t+\theta) + N(t)\cos(\omega t+\theta) \end{aligned} \tag{3.20}$$

Using the trigonometric identity $\cos(\alpha+\beta) = \cos(\alpha)\cos(\beta) - \sin(\alpha)\sin(\beta)$, the $\mathrm{d}I/\mathrm{d}V$ term can be expanded as:

$$\begin{aligned} \left.\frac{dI}{dV}\right|_{V0} V_{\text{mod}}\cos(\omega t) = &-\sin(\omega t)\sin(\theta)) \\ &+ \left.\frac{dI}{dV}\right|_{V0} V_{\text{mod}}\left(\frac{1}{2}(\cos(2\omega t+\theta)+\cos(\theta))\right). \end{aligned} \tag{3.21}$$

Equation 3.16 composes three components, the DC components $\omega = 0$, ω component and 2ω component. Compared to equation 3.21, equation 3.16 can be treated as an ideal case when $\theta = 0$. Using the same method, one can obtain the relative phase dependent on the intensity of channel Y. Because of the low-pass filter, only the DC components are left. The relative phase-dependent DC components in both channels are collected as:

$$\begin{cases} X(t,\omega=0) = \left.\dfrac{dI}{dV}\right|_{V0}\cos(\theta) \\ Y(t,\omega=0) = \left.\dfrac{dI}{dV}\right|_{V0}\sin(\theta). \end{cases} \tag{3.22}$$

Thus, to obtain the maximum signal in channel X, it is essential to calibrate the phase θ before $\mathrm{d}I/\mathrm{d}V$ measurements. This calibration ensures that only channel X captures the signal, while channel Y contains only noise. As a result, the cross-talk between channel X and channel Y is reduced, and the sensitivity and accuracy to capture the signal are ensured.

3.3 Polar scanning probe microscope

3.3.1 Cryostat structure before and after 1K pot upgrading

The experimental data for this thesis were acquired using a Scienta-Omicron POLAR SPM Lab scanning tunnelling microscope. This machine was installed in the lab of the PGI-3 (Peter Grünberg Institute) at the Forschungszentrum Jülich in 2021, with the first measurements started at the beginning of 2022.

The Scienta-Omicron POLAR SPM Lab is an UHV STMsystem, which is supported by a set of four Pneumatic vibration isolators. This system involves one load-lock and two chambers: the load-lock allows the introduction of samples from the ambient conditions or from a vacuum suitcase to the UHV system and vice versa; the preparation chamber contains

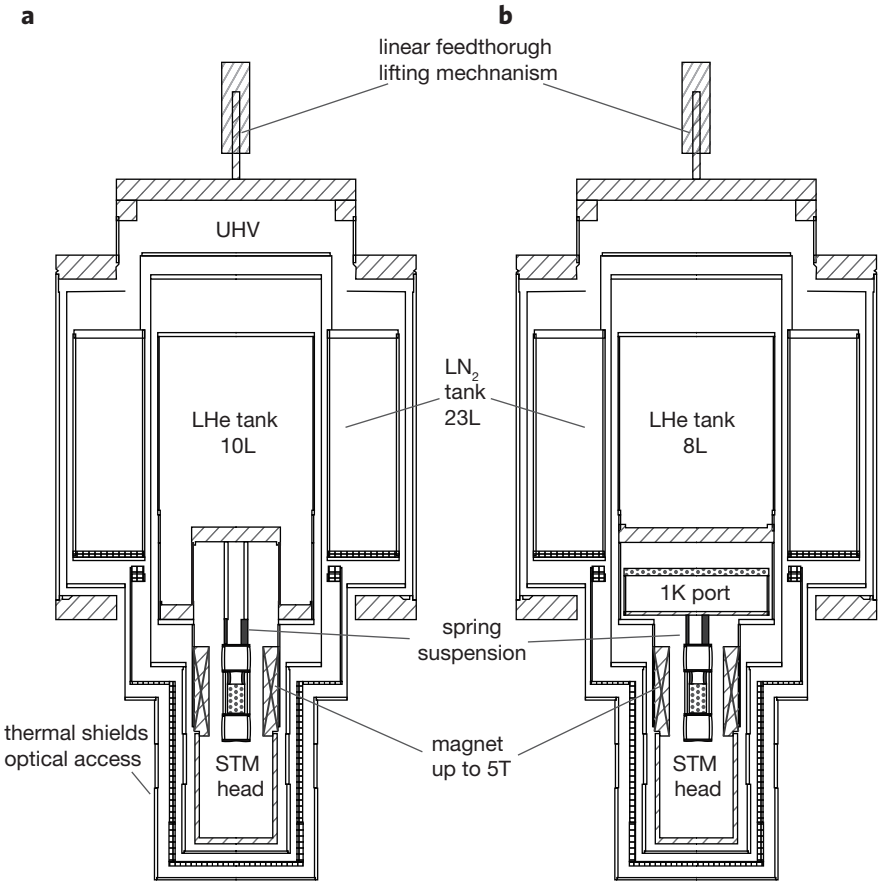

Figure 3.3: **Schematic showing of the polar scanning microscope. a,** Before installing the 1K pot, the base temperature was 6.5 K. **b,** After installing the 1K pot, the base temperature reaches down to 1.4 K.

a sputter gun, a filament annealing station (maximum ~ 500 °C), and a high-temperature heating oven (maximum ~ 1326 °C), all of which are used for obtaining a clean surface [84].

As shown in Fig. 3.3a, the machine consisted of two cryostats. The outer LN_2 cryostat was used to reduce the liquid helium consumption, by initially lowering the temperature to 77 K. The inner LHe cryostat further regulated the temperature to the boiling point of liquid helium, with the STM head attached to it. As a result, the base temperature of the STM head was 6.5 K. Inside the LHe cryostat, a superconducting magnet is able to generate an out-of-plane magnetic field of up to 5 T.

Following the initial setup, a 1K pot was upgraded at the beginning of 2023 and started running in August 2023. As shown in Fig. 3.3b, the main change of this machine involved installing the 1K pot inside the LHe cryostat, with the STM head connected. The 1K pot is a small liquid helium container, whose liquid helium supply is independent of the LHe cryostat. By continuously pumping the 1K pot, the boiling temperature of liquid helium is reduced. Through heat exchange with 1K pot, the STM head can reach a base temperature of 1.4 K from

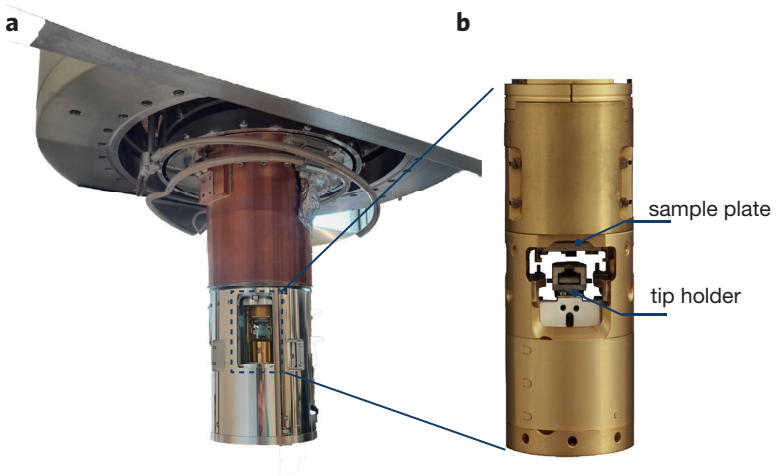

Figure 3.4: **The STM head of the Polar scanning probe microscope. a,** the optical image of the head mounted in the LHe shield. **b,** the zoom image of the head.

4.2 K.

3.3.2 STM head

Figure 3.4a shows that our STM head is protected by a LHe shield with a viewing window for exchanging sample plates and tip holders. The advantage of the STM head is to utilise a modular design. The sample plate and the tip holder can be changed independently. As shown in Fig. 3.4b, the sample plate is placed on the sample carriage with an upside-down orientation. The carriage is attached to the coarse XY piezo tube, which allows for moving roughly 7 mm in both X and Y directions. The multiple electric contact is connected to the sample carriage. By connecting the electric contacts to the sample plate, different functions such as the sample bias and the sample gating can be achieved.

Below the sample carriage is the tray for placing the tip holders. The tip holder tray is connected to the Z-piezo tube which drives tips approaching samples in a coarse motion. There are three electric contacts to the tip tray. One contact is for the tunnelling currents, and the other two contacts extend the machine to other scanning probe techniques including the Qplus atomic force microscopy and high-frequency applications.

4 Fabrication of sample of 2D van der Waals heterostructure

The content in section 4.2 of this chapter is published as a research article in *Advanced Material Interfaces* entitled "*Assembly of Arbitrary Designer Heterostructures withAtomically Clean Interfaces*" by the authors **Keda Jin**, Tobias Wichmann, Sabine Wenzel, Tomas Samuely, Oleksander Onufriienko, Pavol Szabó, Kenji Watanabe, Takashi Taniguchi, Jiaqiang Yan, F. Stefan Tautz, Felix Lüpke, Markus Ternes, and Jose Martinez-Castro.

4.1 Starting point: Assembling of 2D van der Waals heterostructure with clean surface

Developing a mechanical dry transfer technique compatible with surface-sensitive measurement is the starting point for this thesis, whose topic is to explore the 2D heterostructures by using STM. Currently, the dry pick-up assembly of 2D materials [85, 86] and related techniques [87, 88, 89, 90] are the most widely used methods for creating high-quality heterostructures.

These processes begin with a polydimethylsiloxane (PDMS) polymer stamp covered with a sticky polymer film, which is used to pick up 2D crystals exfoliated from bulk material

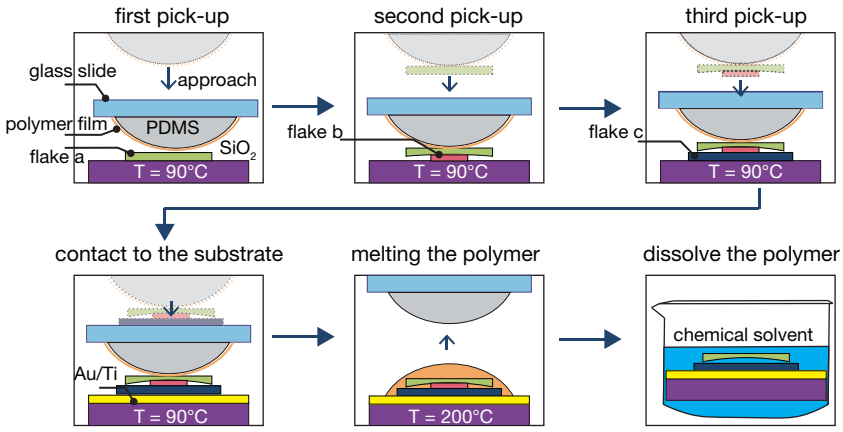

Figure 4.1: **Procedure of the polymer film supported by PDMS stamp transfer technique.**

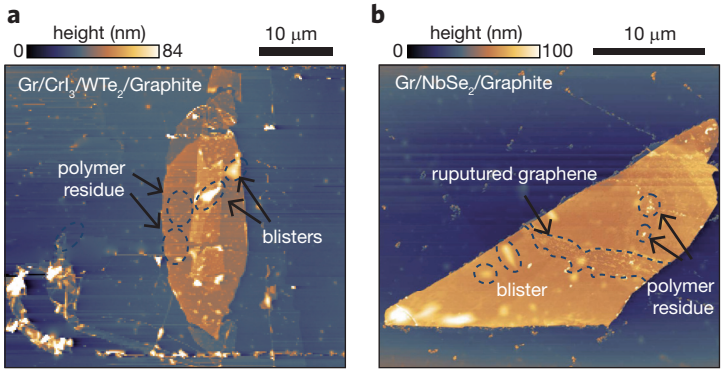

Figure 4.2: **AFM images of heterostructure assembled by the conventional PDMS polymer transfer technique. a,** graphene-encapsulated CrI_3/WTe_2 heterostructure on top of graphite. **b,** graphene-encapsulated $NbSe_2$ flake on top of graphite. Both images were acquired in the contact mode in the ambient condition with the setpoint of ~ 9 nN.

onto a substrate, typically Si/SiO_2. While the polymer film has a strong adhesion over a certain temperature range, the PDMS is soft, allowing controlled contact with the flakes and preventing them from damage.

As shown in Fig. 4.1, the heterostructure is layer-by-layer assembled from top (flake a) to bottom (flake c), starting with the material that will eventually form the topmost layer. In the final step, the heterostructure is released by contacting the target substrate and melting the polymer, followed by the chemical solvent cleaning. Alternatively, a polymer with thermoplastic properties that allow a melt-free release can be employed [89].

However, these standard dry pick-up assembly techniques require full contact between the heterostructure surface and the polymers, which inevitably leaves polymer residues on the final heterostructure surface. If the heterostructure surface consists of a reactive material, this polymer contact can degrade its surface quality. Overcoming these challenges is essential for achieving high-quality, clean surfaces.

A strategy to circumvent this problem is the use of a protective layer, i. e., an inert material that is placed as the topmost layer of the heterostructure to protect (encapsulate) the layers underneath from degradation [88, 91, 92, 93]. In this case, the polymer residues can be removed from the protective layer with a combination of solvents such as chloroform, acetone or isopropanol, and with AFM-based mechanical cleaning methods [94]. The combination of inert encapsulation layers with such cleaning methods has been demonstrated to allow contamination-sensitive surface science techniques to be applied successfully [95, 96]. Nevertheless, protective layers can pose a limit to the accessibility of the underlying material due to their finite thickness and electronic properties which can mask those of the underlying materials. Furthermore, as shown in Fig.4.2, even after cleaning with chemical solvents and AFM ironing, both graphene-encapsulated CrI_3/WTe_2 heterostructures transferred with nitrocellulose film/PDMS stamp and graphene-encapsulated $NbSe_2$ transferred with polyvinyl chloride (PVC) film/PDMS stamp still exhibit polymer residues and blisters on the surface.

These residual contaminants and surface defects cause challenges for STM measurements.

An alternative to avoid polymers coming into contact with the heterostructure surface is to assemble it in reverse order and to flip it over after the assembly process [97, 38, 98]. Using such techniques, the vdW heterostructure is typically released by melting the polymer layer (polypropylene carbonate, PPC) that is used during assembly, leaving a thick PPC layer underneath the finished heterostructure. The PPC is then removed by annealing at 250 °C in vacuum. Unfortunately, while the dry-transfer flip technique is a huge step forward, it has its limitations: 1) The assembled heterostructure must be annealed in a high vacuum for several hours to properly remove the residual PPC layer from underneath the heterostructure. Such extended annealing can cause atomic defects on the heterostructure surface [38]. 2) The required annealing temperature of 250 °C is incompatible with many 2D materials which degrade at this temperature [99]. 3) The large amount of PPC that must be evaporated makes it incompatible with ultra-high vacuum (UHV) environments, which are sensitive to organic contaminants.

This chapter will introduce a technique for the mechanical assembly of ultra-clean vdW heterostructures which overcomes the drawbacks of existing assembly methods. This suspended dry pick-up and flip-over technique does not require the use of a protective encapsulation layer, nor does it require additional cleaning. This suspended dry pick-up and flip-over technique is used as a sample fabrication technique in the projects described in the subsequent chapters.

4.2 Suspended dry pick-up and flip-over assembly

4.2.1 Description of the stamps for suspended dry pick-up and flip-over assembly technique

I begin by describing the suspended dry pick-up and flip-over assembly technique, starting with the preparation of two PDMS stamps. The first stamp (Stamp 1) is used to assemble the vdW heterostructure, while the second stamp (Stamp 2) is used to flip and controllably place the vdW heterostructure onto the target substrate. Figure 4.3a shows the preparation of Stamp 1. This stamp features a dome-shaped PDMS with an approximately $1 \times 1\,\mathrm{mm}^2$ square depression cut into its centre. It is supported by a glass microscope slide. Stamp 2, shown in Fig. 4.3b, consists of a flat, 5 mm thick PDMS block. This block has been cut into two pieces with a scalpel, resulting in a trench of approximately 200 µm width that exposes the supporting glass slide.

Next, I prepared the polymer films that will be used for pick-up, flip-over, and release of the vdW heterostructure. To this end, a commercial PVC film (RIKEN WRAP, Riken Fabro Corp) [89] is first annealed to 130 °C for one minute on a hot plate. This step is crucial because it prevents any uncontrolled thermal shrinkage of the PVC when mounted on the stamps and heated during subsequent steps. After annealing, I transferred the PVC film onto a $1 \times 1\,\mathrm{cm}^2$ square of standard double-sided scotch tape, taking care not to wrinkle the film. The double-

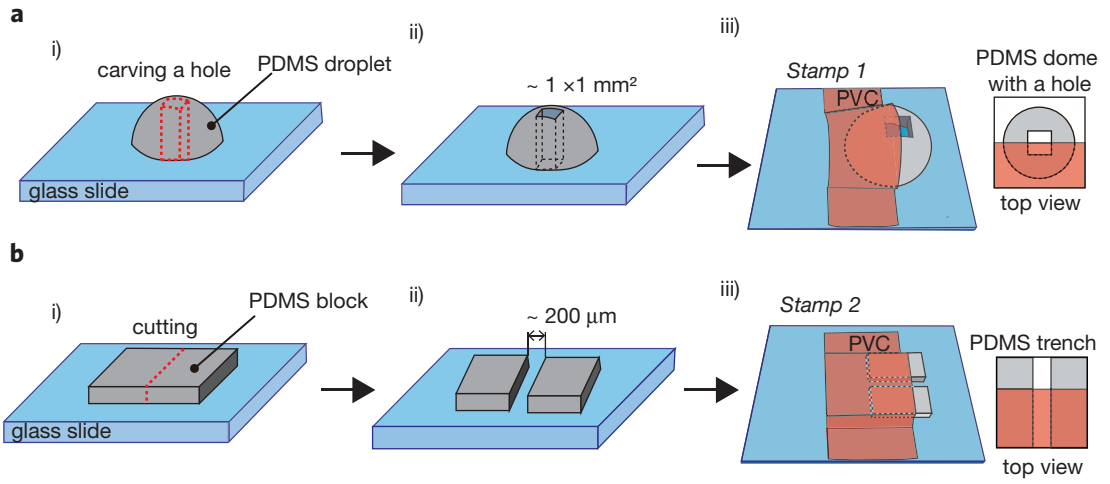

Figure 4.3: **Preparation of the transfer stamps. a,** Procedure of preparation of stamp 1. **b,** Procedure of preparation of stamp 2.

sided tape provides support and stability when manipulating the PVC film. Subsequently, I cut the PVC film into two pieces and placed one of them on PDMS stamp 1, and the other on PDMS stamp 2, covering half of the square depression and half of the trench as shown in Fig. 4.3. Note that, both, the detailed shape of the PDMS stamps as well as the total contact area of the PVC films with the PDMS determine the stiffness of the suspended PVC films. In detail, I have observed that stiffer films show stronger adhesion with 2D materials. Thus, by placing the PVC on the two stamps such that the suspended area on stamp 1 is larger than on stamp 2, I promote stronger adhesion between polymer and heterostructure on stamp 2 compared to stamp 1. This crucial feature enables the transfer of the assembled vdW heterostructure from Stamp 1 to Stamp 2 later in the process, despite them being chemically identical PVC films.

4.2.2 Procedure of suspended dry pick-up and flip-over assembly

Using the two prepared stamps, I assemble the vdW heterostructure in reverse order on a standard assembly stage (HQ graphene). The base flake, which should be thicker than approximately 40 nm, provides the necessary stiffness and mechanical support for the subsequent layers of the heterostructure. First, the base flake is contacted with Stamp 1 at 70 °C by touching roughly half of the flake with the PVC film (red) and then carefully lifting the stamp vertically(Fig.4.4a). Subsequent flakes are picked up by vdW interaction [87] at 70 °C to assemble the desired heterostructure (Fig.4.4b). During each pick-up step, I ensure that the flake does not extend beyond the edge of the base flake.

Once the assembly of the vdW heterostructure on stamp 1 is completed, the heterostructure is flipped using stamp 2. To do this, I place stamp 2 on the transfer stage and raise the temperature to 130 °C. I then carefully bring stamp 1 into contact with stamp 2, making sure that the PVC films on the two stamps only touch the base flake on opposite sides and not each other (Fig. 4.4c). Stamp 1 is then released by gently pressing and sliding it laterally (Fig. 4.4d).

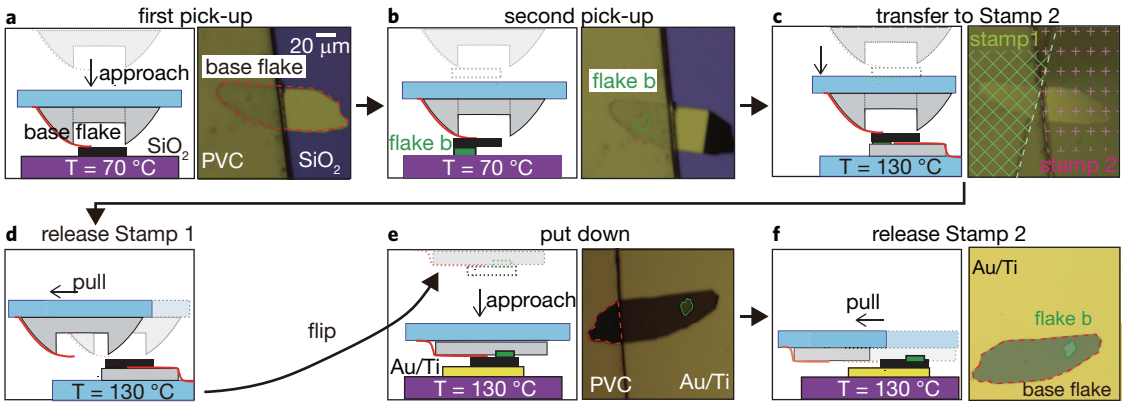

Figure 4.4: **Flow diagram of the heterostructure assembly. a,** Stamp 1 contacts the base flake (graphite, black) by touching half of it with the PVC film (red), then retracts vertically to pick it up. **b,** The heterostructure is assembled by contacting the exfoliated flake (WSe_2, green) on the SiO_2 substrate (purple) with the base flake under the PVC film. **c,** Stamp 1 contacts stamp 2, ensuring each stamp touches half of the base flake (white and red dashed lines). **d,** The heterostructure is transferred by sliding stamp 1 until the base flake is only in contact with stamp 2. **e,** After flipping, stamp 2 with the heterostructure is mounted on the micromanipulator stage and contacts the target substrate (Au/Ti on SiO_2, purple). **f,** The heterostructure is released from stamp 2 by sliding it sideways and retracting vertically.

Next, stamp 2 is flipped over by mounting it into the transfer stage. The heterostructure is then brought into contact with the target substrate at 130 °C (Fig.4.4e). Finally, I release the vdW heterostructure by slowly moving stamp 2 laterally (Fig. 4.4f).

4.2.3 Arbitrary designer heterostructures

By assembling example heterostructures composed of a wide variety of different vdW materials I have demonstrated the broad applicability of this suspended dry pick-up and flip-over assembly technique. The used base flakes of the heterostructures include common 2D materials typically used for optical, transport, and surface characterisation experiments, such as hexagonal boron nitride (hBN), graphite, or MoS_2 [100, 101, 102]. In addition, I have demonstrated that air-sensitive (reactive) materials, such as $NbSe_2$, can also be used as base flakes, although only the base flake surface area which did not come into contact with the PVC film is atomically clean. Figure 4.5 shows a summary of six example heterostructures

- (a) WSe_2 on graphite, the former being a transition metal dichalcogenide known to induce strong spin-orbit coupling into graphene [103];
- (b) bilayer graphene on hBN, the latter being an insulator which is typically used for gating purposes [104];
- (c) twisted-bilayer graphene on MoS_2, assembled from two separate graphene monolayers that have been sequentially picked up with a controlled twist angle between them, allowing the simultaneous study of the strongly correlated physics of twisted-bilayer

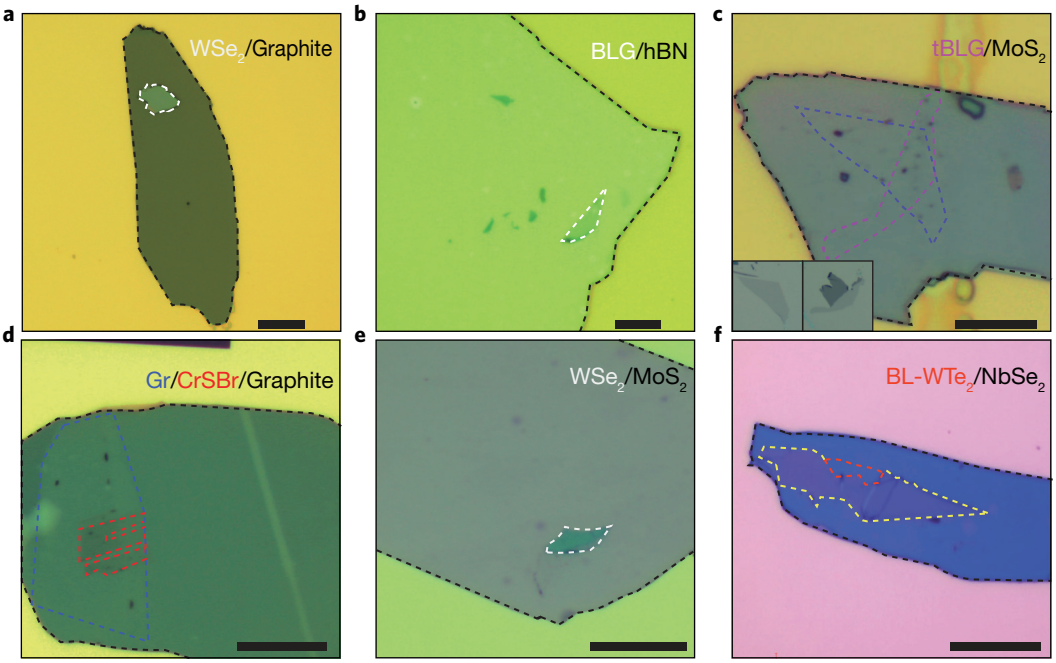

Figure 4.5: **Exemplary vdW heterostructures.** All panels show optical microscopy images of various assembled heterostructures on Au-coated SiO_2 substrates. The flake outlines are indicated as color-coded dashed lines. The scale bars are 20 µm in all panels.

graphene and the proximity-induced strong spin-orbit coupling by the transition metal dichalcogenide [105];

- (d) graphene on CrSBr, the latter being a 2D antiferromagnetic semiconductor whose electronic interlayer coupling can be magnetically controlled [106];
- (e) WSe_2 on MoS_2, a semiconductor heterostructure that has been intensively studied for its optoelectronic properties [107];
- (f) WTe_2 on $NbSe_2$, a heterostructure that realizes one-dimensional topological superconductivity [38, 39].

From the successful assembly of the heterostructures demonstrated here, I conclude that the suspended dry pick-up and flip-over assembly technique can be applied to a wide range of materials including most of the common materials used for optics, electronic transport, and surface science studies. If there are any additional principal limitations at all, they will most likely be found in the vdW heterostructure assembly process itself: A too-strong interaction between the exfoliated flakes and the SiO_2 substrate might prevent the pick-up by the base flake or previously picked-up layers on top of the base flake.

4.2.4 Surface and interface quality

To assess the quality of the assembled vdW heterostructures, I characterize the resulting surface and internal interface quality. To this end, I inspect the assembled vdW heterostructures

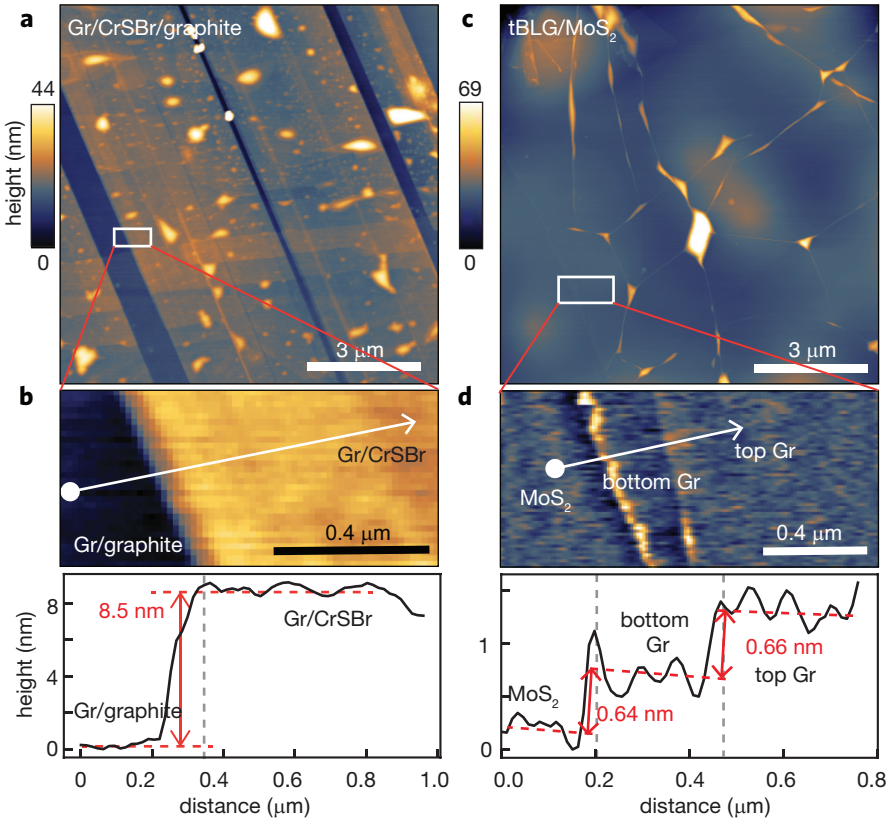

Figure 4.6: **AFM images of assembled vdW heterostructures. a,** AFM topography of graphene on CrSBr on graphite. **b,**Zoomed region of the white rectangle in **a**, with topography cross-section along the white arrow, showing CrSBr step thicknesses. **c,** atomic force microscopy (AFM) topography of twisted-bilayer graphene on MoS_2. **d,** Zoomed view of the white rectangle in **c** with a cross-section along the white arrow indicating graphene layer thicknesses. All the images were acquired in the contact mode in the ambient condition with the setpoint of ~ 9 nN.

with contact-mode atomic force microscopy (c-AFM) at ambient conditions, focusing here on those with top layers of either monolayer graphene (Fig. 4.6a, b) or twisted bilayer graphene (Fig. 4.6c, d), because compared to the thicker 2D materials, graphene is more prone to wrinkle and fold. Less-than-optimal transfer methods tend to produce more trapped blisters and wrinkles in the graphene, allowing a direct comparison between different mechanical assembly methods. I assess three different criteria:

1. The number and area of trapped blisters at the interface,
2. possible damage of the topmost layer, such as ruptures,
3. the amount of residue left on the surface.

In comparison to standard dry-transfer techniques, I find that a reverse assembly of vdW heterostructures generally results in a lower number of trapped blisters and protects the topmost surface from rupturing in agreement with earlier reports [108].

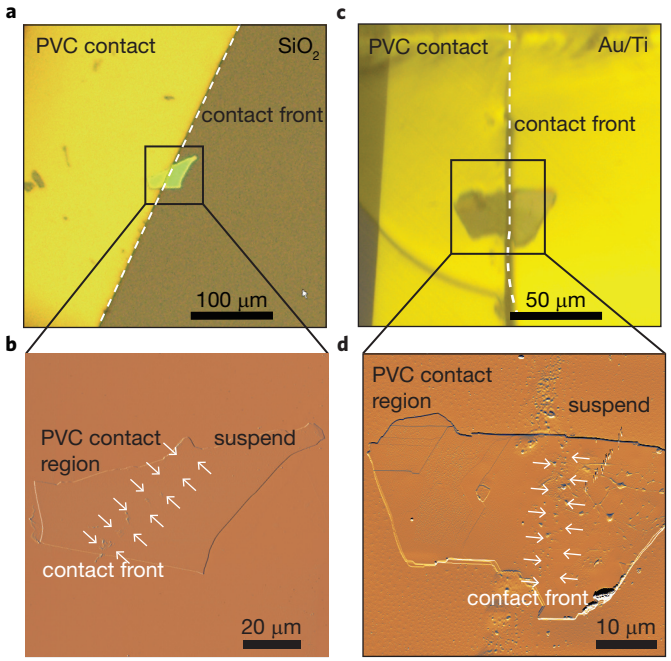

Figure 4.7: **Determination of polymer residue with contact atomic force microscopy. a,** Optical image of a partially suspended graphite flake prior to release. **b,** AFM regulation error-signal image of the graphite flake after transferring it to a SiO_2 chip. **c,** Optical image of the partially suspended tBLG/MoS_2 heterostructure. **d,** AFM regulation error-signal image of the tBLG/MoS_2 heterostructure after transferring it to a SiO_2 chip. White arrows in **b** and **d** indicate the location of the polymer residue coinciding with the PVC film contact.

Furthermore, the overall higher stiffness of the heterostructure provided by the base flake contributes to better interfaces, because it avoids inhomogeneities and stress arising from the flexing of the polymer film. Lastly, I do not observe any traces of residue or damage on the topmost graphene layer whatsoever.

To find out the residue distribution on graphite between the polymer contact region and the suspend region shown in Fig.4.7a, the AFM regulation error signal image in Fig.4.7b shows that residues are located in the contact front between the PVC and the base flake. A similar analysis can be applied to twisted bilayer graphene (tBLG)/MoS_2 heterostructure, where the polymer residues are found in the contact region of the base flake (MoS_2), but absent in the suspend region.

To further compare the surface quality achieved with our suspended dry pick-up and flip-over assembly technique to standard dry-transfer methods, I assembled a heterostructure following Ref. [89], where the heterostructure surface comes in full contact with the PVC polymer, *i.e.*, without flip. The surface of the resulting Gr/$NbSe_2$/graphite heterostructure (Fig.4.2b) exhibits substantial polymer residue as well as damaged regions where the graphene is partially ruptured. Additionally, the graphene/$NbSe_2$ interface shows a multitude of blisters, a signature of trapped polymer residues at the interface [109]. In contrast, the vdW heterostruc-

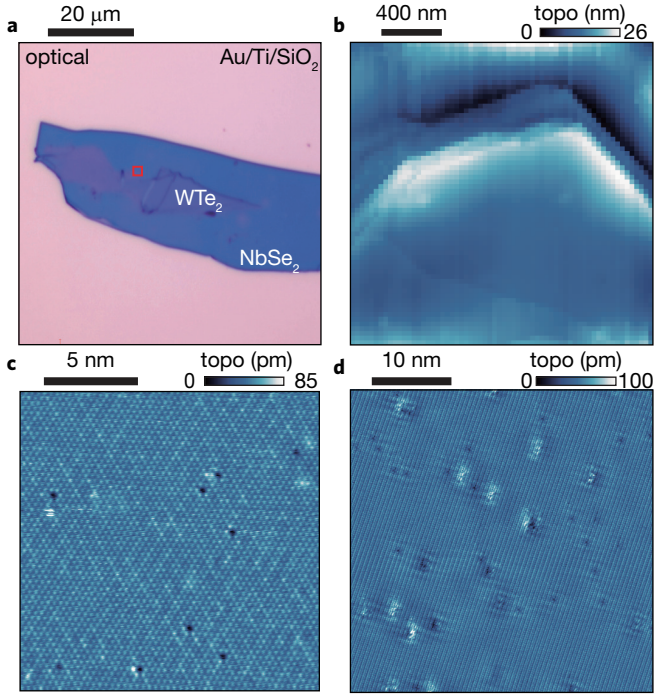

Figure 4.8: **Optical microscopy image and Scanning tunnelling microscopy images of a bilayer WTe_2 on $NbSe_2$ heterostructure. a,** Optical microscopy image of an assembled WTe_2/$NbSe_2$ heterostructure. The red square indicates the area corresponding to the STM topography. **b,** $2\times2\,\mu m^2$ STM topography of the $WTe_2/NbSe_2$ interface (V = 800 mV and I = 20 pA). **c,** Atomic resolution STM topography on bulk $NbSe_2$ ($V = 90$ mV and $I = 100$ pA). **d,** Atomic resolution STM topography on bilayer WTe_2 on bulk $NbSe_2$ ($V = 100$ mV, $I = 100$ pA).

tures assembled with our suspended assembly technique do not show damage or surface contamination. Moreover, these heterostructures exhibit a reduced number of blisters, which also have a smaller radius. A detailed analysis of the AFM topographies in Fig. 4.6b, d shows that their roughness is smaller than the noise of the c-AFM (RMS = 0.74 nm), demonstrating the flatness of the vdW heterostructures' interfaces assembled with this method.

4.2.5 Atomic clean surface proved by scanning tunnelling microscopy

Finally, I analyzed the surface quality and thus the compatibility of our suspended dry pick-up and flip-over assembly technique with contamination-sensitive surface science techniques like STM. For this, I have inspected the $WTe_2/NbSe_2$ vdW heterostructure shown in Fig. 4.5f. Since both $NbSe_2$ and WTe_2 are air-sensitive, the heterostructure was assembled in an argon-filled glovebox and transferred from there to the UHV chamber hosting the STM in a vacuum suitcase.

First, I analyzed the amount of polymer residue on the surface and the edge of bulk WTe_2 on $NbSe_2$. The red box in Fig.4.8a labels the probing region, where I measured a $2\times2\,\mu m^2$ STM image topography corresponding to the maximum scanning range at 4 K. Figure 4.8b points

to the absence of polymer residue at the micrometre scale. Second, for a detailed atomic-level evaluation of the surface cleanliness, measurements at two distinct sites were conducted: bulk $NbSe_2$, and bilayer WTe_2.

Figure 4.8c shows an atomically resolved image of $NbSe_2$—without any surface contaminants—and its 3×3 charge density wave, which emerges below $T_{CDW} = 32\,K$ and is known to be very sensitive to external perturbations [110]. In the same way, I was able to obtain atomically resolved images of the bilayer WTe_2 situated on the $NbSe_2$, again showing only single atomic defects (Fig. 4.8d).

4.3 Pre-patterned chip fabrication and the chip mounting

Following the procedure detailed in section 4.2.2, the assembled 2D vdW heterostructures are placed onto pre-patterned chips. These pre-patterned chips are fabricated by a two-step electron-beam lithography process at the Helmholtz Nano Facility (HNF). In the first step, a $500 \times 500\,\mu m^2$ electrode is created and the second step patterns a guide bar with the width of $1\,\mu m$ on top of the electrode. This guide bar is used to navigate the probe tip to the sample spot and will be explained in the next section (section 4.4).

As illustrated in Fig.4.9, in both steps, typical two-layer polymethyl methacrylate (PMMA) is spin-coated as the electron beam resist (top layer: AR-P 679.04 950k, bottom layer: AR-P 649.04 200k). After exposure, a Methyl isobutyl ketone (MIBK)/isopropanol (IPA)-based developer (AR 600-56) is used to remove the PMMA region which is exposed by the electron beam.

Subsequently, for the first step, 20 nm Ti and 80 nm Au are deposited for the electrode. For the second step, 5 nm Ti and 15 nm Au are deposited for the guide. After metal deposition, an acetone-based lift-off process (AR 600-71) is performed, followed by oxygen plasma etching to clean any PMMA residue.

4.4 Navigate the probing tip to the 2D vdW heterostructures

To transfer the chips with the 2D heterostructure into the UHV chamber for the STM measurement, the chips need to be mounted onto an Omicron sample plate (Fig.4.10a), where the chip is mechanically clamped by two champing sheets. Silver epoxy (EPO-TEK H20E) is used to establish an electrical connection between the sample plate and the chip electrode (Fig.4.10b).

After mounting the sample to the sample plate and connecting the electrode, I transfer the sample from an Argon-filled glovebox into the UHV chamber with a vacuum suitcase, in order to avoid air exposure. I anneal the sample at 120 °C for 15 min at $< 1 \times 10^{-9}$ mbar in the preparation chamber before I transfer the sample into the cryostat. This process removes adsorbed gas molecules and water from the sample surface. The layout of the 2D vdW heterostructure is shown in Fig.4.10c, where I put the 2D vdW heterostructure at the corner

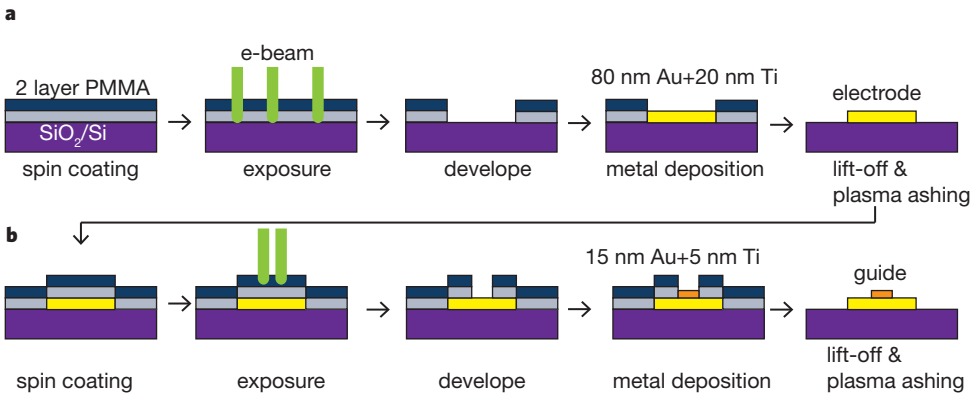

Figure 4.9: **Procedures for fabricating the pre-patterned chips a,** First e-beam lithography step: The substrate is spin-coated with an electron-sensitive resist (PMMA) and exposed to a focused electron beam to define the initial pattern. After development, 20 nm of titanium (Ti) binding layer and 80 nm of gold (Au) are deposited onto the substrate. The mask is subsequently removed using an acetone-based lift-off process. **b,** Procedure for the second e-beam lithography step. Following the initial patterning, a second layer of resist is applied, and the substrate undergoes another e-beam exposure to define the guide. A resist layer is coated, and the substrate undergoes another e-beam exposure to define additional features. A 5 nm Ti and 15 nm Au are deposited, again followed by the removal of the mask through a lift-off.

of the landing pad, and there is a guide bar pointing to this position. Omicron Polar SPM provides two optical windows, by mounting a long focus distance microscope and a camera out of the chamber, I can approach the electrode near the 2D vdW heterostructure with an etched tungsten tip (Fig.4.10d).

The procedure for navigating of the tip towards the sample is described as follows:

1. Use the optical camera to approach the probe tip as close as possible to the landing pad.
2. Use the coarse motion function to move the tip in the +X direction to the edge without crashing the tip. The edges of the landing pattern are aligned with the X and Y directions of the scanner as shown in Fig.4.10b.
3. Automatically approach the tip to the landing pad using a large bias voltage and small tunnelling current of V = 3 V and I = 20 pA.
4. Scan a line with the maximum range of 2.2 µm in X direction. If the guide is not found, retract the tip and perform a coarse motion of 1.5 µm in the +X direction. The line profile of the polycrystalline gold with and without a guide is shown in Fig.4.10e.
5. Repeat step 4 until the guide is found. The topography of the guide is shown in Fig.4.10f.
6. Scan a line with the maximum range of 2.2 µm in Y direction. If I do not find the heterostructure, retract the tip and perform a coarse motion of 1.5 µm in the +Y direction.
7. Repeat step 6 until the heterostructure is found.

Before walking the probe tip to the heterostructure, I check the tunnelling current-sample bias (I-V) characteristic curve of the tip-polycrystalline gold junction. The remaining chapters of this thesis will discuss the experimental results after the tip has been navigated to the

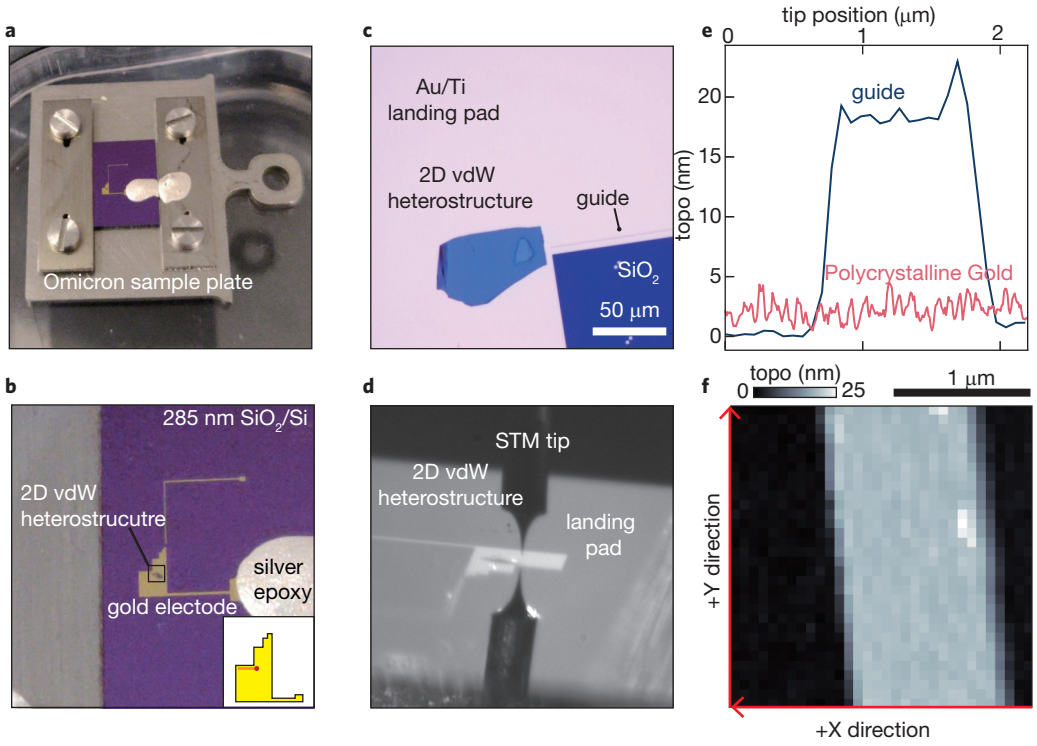

Figure 4.10: **Mounting the sample and navigating the STM probe tip to the sample. a,** Gold patterned silicon chip ($7 \times 7\,\mathrm{mm}^2$) is mechanically clamped onto the Omicron sample plate. **b,** Zoom-in view of the chip mounted on the sample plate, showing the 2D vdW heterostructure on the gold landing pad as the electrode. The insert panel shows the layout of the heterostructure (red spot) and the guide (orange) on the gold landing pad (yellow). **c,** Optical image of the 2D vdW heterostructure on the gold patterned chip prior to transferring to the UHV chamber. **d,** Optical image of the tip approach to the 2D sample inside the cryostat. The tip is above the chip, while a reflection of the tip is below. A long-focus distance microscope takes this image. **e,** Line scan of the polycrystalline gold surface with (blue) and without (red) the guide ($V = 3\,\mathrm{V}$, $I = 20\,\mathrm{pA}$). **f,** STM image of the guide ($V = 3\,\mathrm{V}$, $I = 20\,\mathrm{pA}$).

heterostructure.

5 Proximity-induced doped Mott physics in 1T-$NbSe_2$/2H-$NbSe_2$ heterostructures

5.1 Introduction

$NbSe_2$ is a famous member of the TMD family, renowned for its versatile electronic properties that vary with its crystal structure [113]. In its trigonal prismatic (hexagonal, H-phase) configuration, $NbSe_2$ presents a coexistence of metallic phase and 3×3 CDW below 30 K, and as further cooling down below the critical temperature of 7.2 K, $NbSe_2$ reveals the coexistence of superconductivity and 3×3 CDW (Fig. 5.1a) [114].

On the contrary, the octahedral setting (tetragonal, T-phase) $NbSe_2$ exhibits a different $(\sqrt{13} \times \sqrt{13})$R13.9° CDW, which reconstructs the formation of SoD-like clusters (Fig. 5.1b). The theoretical study [115] suggests that for the free-standing monolayer, the formation of the SoD clusters results in a half-filling flat band near the Fermi level. According to classic band theory, a half-filled band should lead to metallic behaviour; however, experimental STS measurements reveal an insulating gap at the Fermi level, indicating that 1T-$NbSe_2$ is an insulator, not a metal [116]. At first, this insulating behaviour was thought to arise from a Hubbard-Mott gap, suggesting a Mott-insulating state. In this scenario, the small intercluster hopping amplitude within the flat band would be dominated by the on-site Coulomb interaction hindering hopping, splitting the band into two Hubbard bands and opening an energy gap between them (Fig. 5.1c). The band above the Fermi energy is denoted as the upper Hubbard band (UHB), while the band below is the lower Hubbard band (LHB). This Mott insulating state emerges from strong electron-electron interactions that localise charge carriers, thereby preventing metallic conduction despite the half-filled band [**?**].

The formation mechanism of the Star of David CDW in 1T-$NbSe_2$ differs from the Peierls instability. Density functional theory calculations suggest that the $\sqrt{13} \times \sqrt{13}$ reconstruction arises from a combination of electron-phonon coupling and strong electron correlations [115**?**]. Unlike its 2H phase, where Fermi surface nesting plays a role, the 1T-phase CDW is driven by energy minimisation of the correlated electronic state within the flat band.

Furthermore, recent experimental measurements of 1T-$NbSe_2$ on bilayer graphene [117, 118] argued that the observed gap in the $\mathrm{d}I/\mathrm{d}V$ spectrum corresponds to the charge transfer insulator rather than the Mott insulator. The LHB of the SoD clusters is merged with the

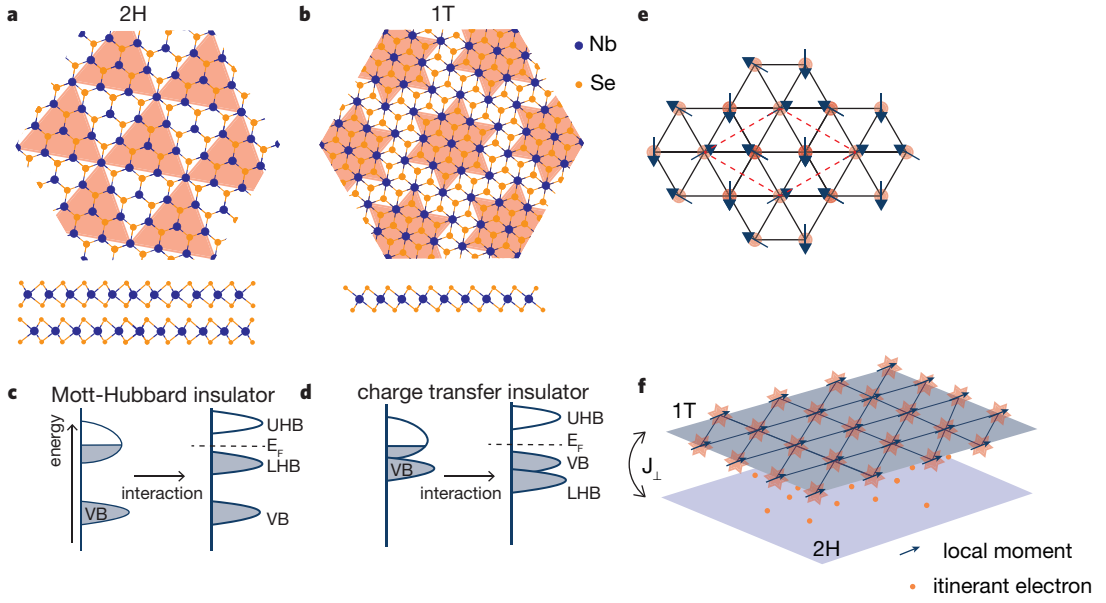

Figure 5.1: **Schematic illustrations of 1T and 2H polymorphs of $NbSe_2$. a,** Schematic crystal structure of 2H-$NbSe_2$. The 3×3 CDW is highlighted in the 2H phase. **b,** Schematic crystal structure of 1T-$NbSe_2$. The $(\sqrt{13} \times \sqrt{13})$R13.9° CDW modulation is highlighted in the 1T phase. **c,** Schematic illustration of energy levels for the Mott insulator driven by electron interaction. **d,** Schematic illustration of energy levels for a charge transfer insulator driven by electron interaction. (Adapted from [111]) **e,** frustrated magnetism in a hexagonal lattice. The red dotted lines show the $\sqrt{3} \times \sqrt{3}$ superlattice. (Adapted from [112]) **f,** Schematic of stacking 1T-$NbSe_2$ on 2H-$NbSe_2$. Each SoD site in the 1T-$NbSe_2$ layer is filled with one local electron, and the 2H-$NbSe_2$ layer hosts the itinerant electrons. The coupling strength of the two layers is given by $J_\perp$.

valence band of the $NbSe_2$ crystal, while the UHB of the SoD clusters is isolated above the valence band maximum, creating a gap in the electronic density of states (Fig. 5.1d). This gap is maintained by strong electron-electron correlations and charge transfer interactions between the localised *d*-electrons on the central niobium atom within each SoD cluster structure.

Additionally, each *d*-electron localised on the SoD cluster carries a local magnetic moment, raising a question about the spin-spin coupling between adjacent SoD clusters within the hexagonal superlattice. The observed $\sqrt{3} \times \sqrt{3}$ pattern in respect to CDW superlattice at the bias corresponding to the UHB suggests a possible 120° antiferromagnetic coupling (Fig. 5.1e) [119]. The antiferromagnetic coupling in the hexagonal lattice could develop into a frustrated antiferromagnetic lattice, hinting that 1T-$NbSe_2$ is a promising platform for realising a quantum spin liquid.

The Crommie group first reported observing a quantum spin liquid in the phenomenologically similar system of 1T-$TaSe_2$. By stacking 1T-$TaSe_2$ on top of 1H-$TaSe_2$, they found zero bias peaks, which were attributed to the interaction between the local magnetic momentum at the SoD inthe 1T-$TaSe_2$ layer and the itinerant electrons in the 1H-$TaSe_2$ layer. In

addition, the observation of an incommensurate pattern with respect to the CDW lattice in 1T-$TaSe_2$ on bilayer graphene was attributed to the separation of the elementary excitations [**?**]. This separation is evidence of the quantum spin liquid [120, 121]. Following the same methodology, 1T-$NbSe_2$ was also reported as a candidate for hosting a quantum spin liquid. This claim is supported by the long wavelength modulation of the CDW superstructure and the observation of a spinon Kondo resonance peak at the edge of the UHB when magnetic manganese-phthalocyanine (MnPc) molecules are deposited onto 1T-$NbSe_2$ [122].

During the preparation of this thesis, a new preprint paper measuring the heterostructure of 1T-$NbSe_2$ on 1H-$NbSe_2$ argued that 1T-$NbSe_2$ become a doped Mott insulator due to the charge transfer from the 1H-$NbSe_2$. This study revealed that the doping level is spatially inhomogeneous at the microscopic level [123]. In addition, the quasi-one-dimensional Kondo lattice was reported in the strip CDW phase of 1T-$NbSe_2$, which is the distorted SoD CDW [124].

Thus, the interest in the CDW in 1T-$NbSe_2$ arises from two aspects. First, 1T-$NbSe_2$ exhibits strong correlation effects that can be tuned by the choice of substrate. When placed on bilayer graphene, 1T-$NbSe_2$ displays intrinsic insulating behaviour. However, on 1H-$NbSe_2$, it reveals a range of correlation effects associated with exotic quantum phenomena. In particular, this tuning allows the exploration of phenomena represented in the Doniach phase diagram for the hexagonal lattice [125, 126], which maps the competition between Kondo screening and magnetic order in correlated systems. Second, by combining 1T-$NbSe_2$ with other 2D vdW materials, such as graphene, the strong charge modulation of the CDW in 1T-$NbSe_2$ can be used to engineer and manipulate the electronic properties of the system. The details of the second aspect will be discussed in the next chapter.

As 1T-$NbSe_2$ is meta-stable, it can currently be prepared by molecular beam epitaxy at elevated substrate temperature or by applying voltage pulses (typical $0.1 \rightarrow 3$ V, duration 100 ms) to 2H-$NbSe_2$ with an STM tip, which induces a phase transition in the topmost layer to the 1T-phase. In this chapter, we employed the bias pulsing method to prepare 1T-$NbSe_2$ on 2H-$NbSe_2$ (Fig. 5.1f). Given the surface-sensitive nature of the tunnelling signals measured by STM and the hybridisation of 1T-$NbSe_2$ with 2H-$NbSe_2$ predominantly occurring at their interface, with minor dependence on the thickness of the 2H-$NbSe_2$ substrate, the STM measurement on 1T-$NbSe_2$/2H-$NbSe_2$ offers a promising platform for investigating the coupling between these two phases. The observed inhomogeneity in the low-energy features aligns with the interpretation that 1T-$NbSe_2$ behaves as a doped Mott insulator, where the doping level varies at the nanometer scale, transitioning from hole-doped to electron-doped regions.

5.2 Engineering of 1T phase

We placed a 2H-$NbSe_2$ flake with a thickness of about 80 nm on the pre-patterned gold coating chip and probe with a tungsten tip(Fig. 5.2a). The topography of the 2H-$NbSe_2$ flake reveals a typical $NbSe_2$ atomic resolution modulated by 3×3 CDW (Fig. 5.2b). Fourier transformation

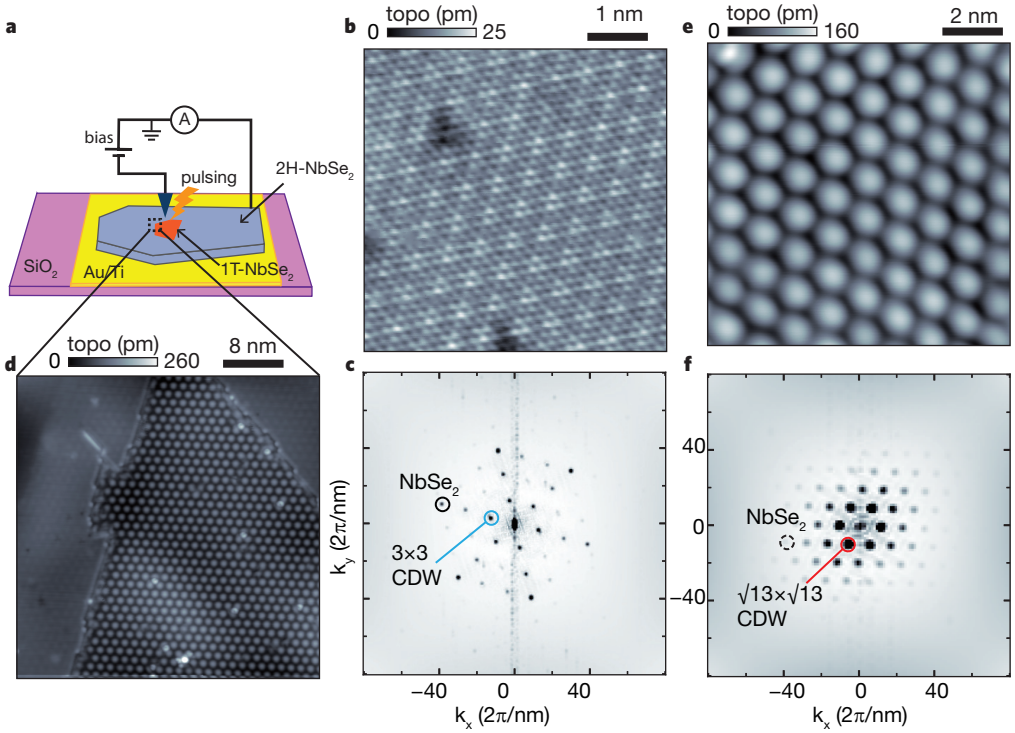

Figure 5.2: **Nanoscale engineering of 2H-$NbSe_2$ to 1T phases. a,** Schematic of the setup for using the probing tip to pulse the sample. **b,** Topography of 2H-$NbSe_2$ bulk. (V = 0.5 V, I = 500 pA). **c,** Corresponding FFT of 2H-$NbSe_2$ revealing 3 × 3 CDW . **d,** Topography of the boundary between 1T-$NbSe_2$ and 2H-$NbSe_2$. (V = 50 mV, I = 100 pA.) **e,**Topography of 1T-$NbSe_2$ on 2H-$NbSe_2$ bulk. (V = 0.3 V, I = 100 pA). **f,** Corresponding FFT of 1T-$NbSe_2$ on 2H-$NbSe_2$ bulk revealing $(\sqrt{13}\times\sqrt{13})$R13.9° CDW.

of the topographic image (Fig. 5.2c) shows the clear sets of Bragg peaks corresponding to the lattice constant of $NbSe_2$ (a_{NbSe_2} = 0.344 nm), and the 3 × 3 CDW of the $NbSe_2$ with 1.032 nm.

By applying voltage pulses to the probing tip, we locally induce a transition of the topmost $NbSe_2$ layer from the hexagonal structure (2H-phase) into a new phase over regions spanning tens of nanometers. The resulting phase boundary between the 2H-phase and this new phase is shown in Fig. 5.2d, where the new phase is embedded within the 2H-$NbSe_2$ flake. In the same scanning image, the 2H-$NbSe_2$ areas maintain well-resolved atomic structures modulated by the 3 × 3 CDW. In contrast, the new phase regions exhibit a cluster hexagonal superstructure, rendering the atomic structure of the new phase unresolved with STM probing.

Figure 5.2e presents a zoomed-in topography of the newly formed phase region. We observe this cluster superstructure with significantly larger amplitude and intensity. The FFT image reveals that this superstructure corresponds to the well-known $(\sqrt{13}\times\sqrt{13})$R13.9° (Fig. 5.2f), which characterises the 1T-$NbSe_2$ phase [119]. Thus, despite the inability to directly resolve the atomic structure of the new phase via STM, the $(\sqrt{13}\times\sqrt{13})$R13.9° periodicity and strong charge modulation of this commensurate CDW confirm the induction of the phase

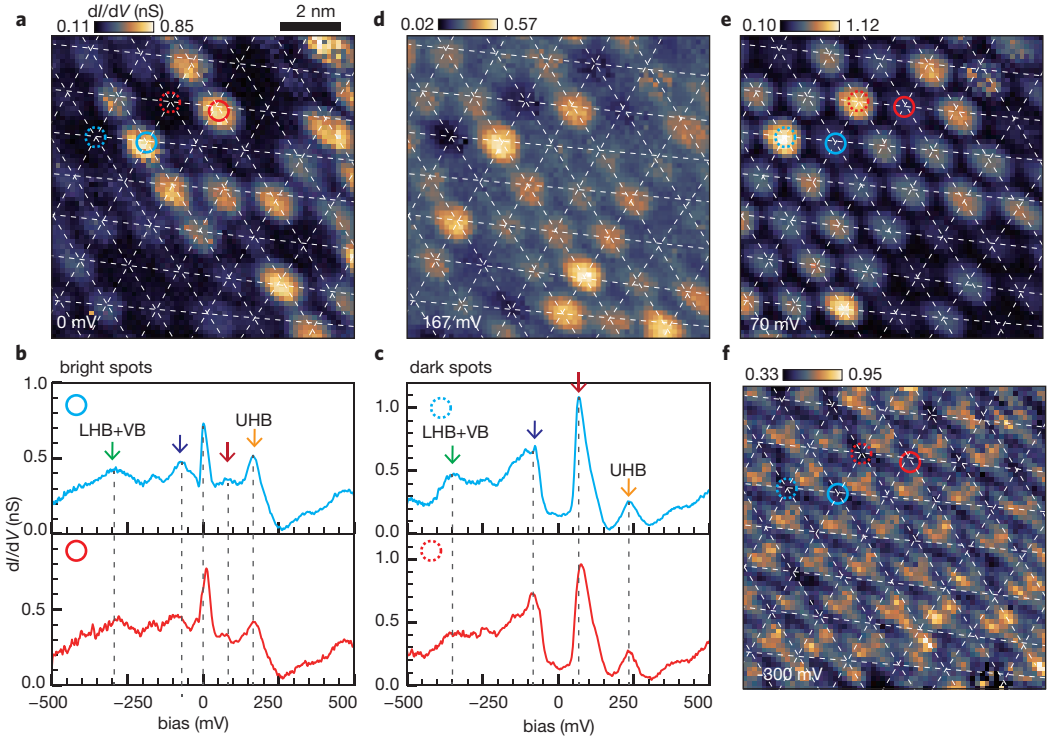

Figure 5.3: **electronic structure of 1T-$NbSe_2$ on 2H-$NbSe_2$. a,** STS grid at 0 mV, showing dark and bright spots in the differential conductivity. **b,** STS spectra were measured at bright spots. Both of the spectra exhibit a prominent peak close to the Fermi energy. (V = 500 mV, I = 100 pA, V_{mod} = 5 mV) **c,** STS spectra were measured at dark spots, both of which show a dip-like feature near the Fermi energy. (V = 500 mV, I = 100 pA, V_{mod} = 5 mV) **d,** STS grid slicing at 167 mV. **e,** STS grid slicing at 70 mV, where the bright spots lose intensity and the dark spots become bright. **f,** STS grid slicing at −300 mV, where the bright spots lose intensity and the dark spots become bright.

transition from 2H-$NbSe_2$ to 1T-$NbSe_2$.

5.3 Electronic structure

5.3.1 Spatially inhomogeneous distribution

Although in the topography image in Fig. 5.2e, CDW reveals homogeneous modulation, the dI/dV grid slicing at the Fermi level (0 mV) is not uniform (Fig. 5.3a), and we did not observe long-range order. Some clusters exhibit higher differential conductivity (bright spots) while others exhibit lower differential conductivity (dark spots) at E_F. STS spectra taken at the bright spots exhibit a multiple-peak feature: a sharp peak approximately centred at zero bias known as Kondo resonance peak [55, 127], and four side peaks at −300 mV, −90 mV, 70 mV, and 168 mV(Fig. 5.3b). For the bright spots, the peak located at −90 mV is more prominent than the peak at 70 mV.

In contrast, the STS spectra taken at the dark spots exhibit the disappearance of the zero bias peak and show a gap-like feature centred at zero bias (Fig. 5.3c). The bottom of the gap has finite differential conductivity, which is attributed to the 2H-$NbSe_2$ substrate underlying the 1T-$NbSe_2$. This gap is flanked by two peaks at −90 mV and 70 mV. Additionally, the peaks located at −300 mV and 167 mV are also observed at the dark spots. Density functional theory calculation involving the electron-electron interaction predicted that the UHB of the free-standing 1T-$NbSe_2$ is located at 200 mV, and the merging of LHB with the valence band (VB) is approximately located at −300 mV [122]. Accordingly, we assign the observed peak at −300 mV to the LHB+VB, and the peak at 168 mV to the UHB.

The STS grid slicing at a bias V= 167 mV (Fig. 5.3d) shows similar behaviour as the pattern slicing at zero bias (Fig. 5.3a), with the clusters showing the higher (or lower) differential conductance at zero bias also exhibiting the higher (or lower) conductivity at the UHB. However, the STS grid slicing at 70 mV(Fig. 5.3e) shows the inverse conductivity distribution relative to the grid slicing at 167 mV and zero bias, where the dark spots become bright and the bright spots become dark. Additionally, the energy position of this peak at 70 mV varies across the sample. The spectrum shown in the lower panel of Fig. 5.3c reveals a shift closer to the Fermi level compared to the upper panel. The STS grid slicing at −300 mV(Fig. 5.3f) shows a uniform clover-shaped pattern which is distinct from the inhomogeneous cluster pattern observed at other energy slices.

5.3.2 Doped charge-transfer insulator and the Kondo coupling

This non-uniform electronic structure in the microscopic scope can not be attributed to the disorder in the 1T-$NbSe_2$ lattice structure as evidenced by the topography. Also, a similar observation of lack of homogeneity was also reported in molecule beam epitaxy growth 1T-$NbSe_2$ on 1H-$NbSe_2$ [123]. A plausible explanation lies in the proximity effect between 2H-$NbSe_2$ and 1T-$NbSe_2$, which depends on the stacking configuration of the 3×3 CDW in 2H-$NbSe_2$ and the $\sqrt{13} \times \sqrt{13}$ CDW in 1T-$NbSe_2$. These stacking configurations are inherently incommensurate, leading to the spatial inhomogenous in electronic interactions. This proximity effect involves an interplay of the Kondo coupling between the local magnetic moment in the 1T-$NbSe_2$ with the electron reservoir of 2H-$NbSe_2$ and the charge transfer between them, leading to the doped Mott physics [128].

The Kondo coupling is well studied in the 1T-TaS_2 on 1H-TaS_2 and 1T-$TaSe_2$ on 1H-$TaSe_2$. There are rich correlated phenomena reported, including heavy fermions [129] and coherent 2D Kondo lattice [125, 130]. However, different from Tantalum-based chalcogenide, 1T-$NbSe_2$ is a charge transfer insulator, and doping the 1T-$NbSe_2$ results in the doped charge-transfer insulator instead of a doped Mott insulator [123].

The difference between the doped Mott insulator and the doped charge transfer insulator is detailed in ref. [131]. Here, I provide a brief explanation of the difference. First, we start with the doping of a band insulator (Fig. 5.4a). In a band insulator, all electronic states in the valence band are fully occupied, while the conduction band remains empty, with a well-defined energy

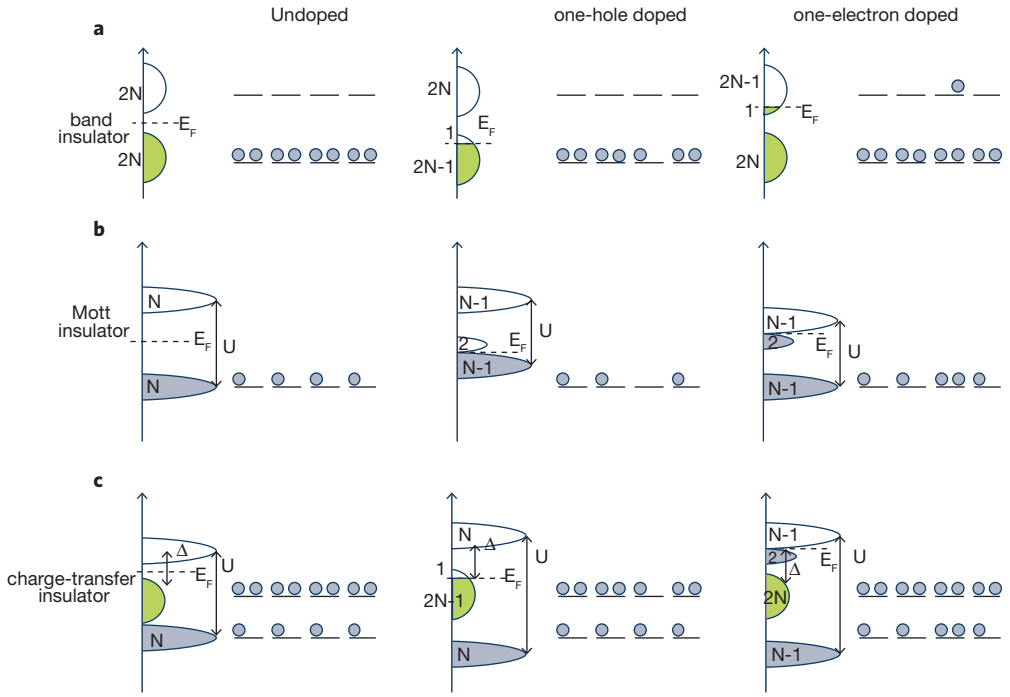

Figure 5.4: **Schematic of doping effects in different insulators. a,** Undoped, one hole-doped, and one electron-doped configurations of a band insulator. **b,** Undoped, one hole-doped, and one electron-doped configurations of a Mott insulator. **c,** Undoped, one hole-doped, and one electron-doped configurations of a charge transfer insulator, showing the on-site Coulomb energy U and charge transfer energy Δ. Lines represent sites, and dots represent electrons. (Adapted from [131])

gap separating the two. This arrangement is described by a single-electron model. With N sites in the solid, there are $2N$ occupied states and $2N$ unoccupied states, accounting for both spin up and spin down. When a band insulator is hole-doped, the chemical potential shifts into the previously occupied valence band, creating an imbalance with $2N-1$ electron states and $2N+1$ hole states. This electron-adding spectrum involves two parts: a small part of the unoccupied valence band states and the empty conduction band. This process only involves the Fermi level shifting, and there is no redistribution of the spectral function. When a band insulator is doped with electrons, the Fermi surfaces shift to the conduction band, and there is no redistribution of the spectral function.

For a Mott-Hubbard insulator (Fig. 5.4b), the insulating behaviour originates from strong electron-electron Coulomb interactions rather than an energy gap between filled and empty bands. The electron-removal spectral weight is equal to the number of occupied levels, while the electron-addition spectral weight is equal to the number of unoccupied levels. At half-filling, the electron-removal spectrum and electron-addition spectrum are both equal to N. When doped with a hole, the electron removal weight reduces to $N-1$ due to one electron reduction, and the electron addition spectrum for UHB becomes $N-1$, representing possible electron additions to singly occupied sites. Additionally, the unoccupied site created by the

hole doping can accept two electrons, thus the electron addition spectrum for this site is 2 [132].

In a charge transfer insulator (Fig. 5.4c), the electronic structure comprises correlated bands separated by an uncorrelated valence band. Upon doping, charge transfer insulators display asymmetric behaviours depending on whether electrons or holes are added. Electron doping causes a transfer of spectral weight from high to low energy, similar to the redistribution observed in Mott insulators. In contrast, hole doping behaves similarly to a band insulator, where no significant spectral weight transfer occurs. This asymmetry between electron and hole doping is a unique feature of charge transfer insulators, different from Mott insulators [131, 132].

The electronic properties observed in the 1T-$NbSe_2$/2H-$NbSe_2$ heterostructure arise from the incommensurate coupling between the 3×3 CDW in 2H-$NbSe_2$ and the $\sqrt{13} \times \sqrt{13}$ SoD CDW in 1T-$NbSe_2$. This coupling is complex because both CDWs exhibit spatial sensitivity. For the 3×3 CDW in 2H-$NbSe_2$, measurements of iron adatoms reveal that the exchange interaction is site-dependent, aligning with the periodicity of the 3×3 CDW structure [133], and the charge density modulation landscape is strongly influenced by the positions of local magnetic moments [134]. Similarly, for the $\sqrt{13} \times \sqrt{13}$ SoD CDW in 1T-$NbSe_2$, insights from an analogous system, 1T-Ta_2 bulk, show that insulating and metallic behaviours depend critically on the stacking order of the SoD clusters [135]. Thus, the Kondo coupling and the doping effect of 1T-$NbSe_2$ with 2H-$NbSe_2$ will have a complicated spatial distribution. For sites where the Kondo coupling is relatively weak, and the doped Mott physics dominates the system, we may see the spectrum as shown in Fig. 5.3c. There, the two side peaks marked by blue and red arrows show strong intensity, which arises due to the doping of the charge transfer insulator, and the peak marked by the blue arrow is wider than the peak marked by the red arrow, due to the hybridising of the LHB with the VB. On the contrary, for the sites dominated by Kondo coupling, we observed strong zero-bias peaks. In the next section, a method to evaluate the doping level by analysing the Kondo peaks is presented

5.3.3 Evaluation of the Kondo resonance

When localised moments in 1T-$NbSe_2$ are coupled to conduction electrons in 2H-$NbSe_2$, the Kondo effect can arise, where the conduction electrons screen the magnetic moments, forming a Kondo singlet state at low temperatures. This screening leads to the appearance of a sharp resonance at the Fermi level in the density of states, known as the Kondo resonance. The origin of this resonance, often observed as a Fano-like line shape near the Fermi level, is explained in detail in section 2.1.1. According to Fermi liquid theory, this Kondo resonance is fitted by a Fano line as [136, 55]:

$$\frac{\mathrm{d}I}{\mathrm{d}V} \propto \frac{\left(q+\epsilon'\right)^2}{1+\epsilon'^2} + \left(1+\beta\epsilon'\right)\rho_0. \tag{5.1}$$

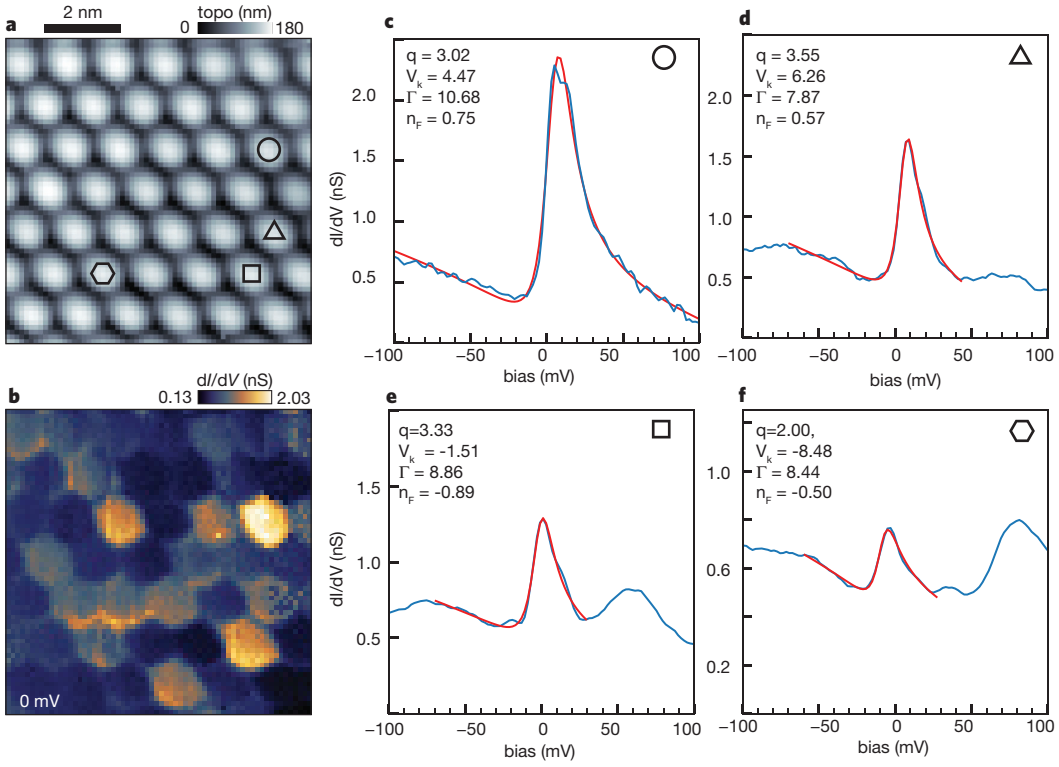

Figure 5.5: **Evaluation of the peak close to the Fermi level. a,**Topography image shows the homogenous structure of the 1T-$NbSe_2$. ($V = 0.2$ V, $I = 100$ pA). **b,**STS grids slicing at zero bias ($V = 0.2$ V, $I = 100$ pA, $V_{\mathrm{mod}} = 2$ mV). **c-f** STS spectra (blue lines) recorded at various positions($V = 0.2$ V, $I = 100$ pA, $V_{\mathrm{mod}} = 2$ mV) and the Fano-shape fitting (red lines).

In equation 5.1, $\left(1+\beta\epsilon'\right)\rho_0$ is the conductivity background with β as a background slope,q characterizes the Fano line shape, which is given by the direct and indirect tunnelling at the resonance bias, and ϵ' is normalized bias given by $\epsilon' = (V - V_k)/\Gamma$, with V_k the resonance position and Γ the half-width of the resonance peak. The width of the Kondo resonance Γ is determined by the Kondo temperature and the experimental temperature by [55]

$$e\Gamma = \frac{1}{2}\sqrt{(\alpha k_{\mathrm{B}} T)^2 + (2k_{\mathrm{B}} T_{\mathrm{k}})^2}. \tag{5.2}$$

The filling factor can be related to the ratio of the position of the resonance V_K to the resonance width Γ as [55]:

$$\frac{V_{\mathrm{k}}}{\Gamma} = \tan\left(\frac{\pi}{2}(1 - n_{\mathrm{f}})\right). \tag{5.3}$$

Thus equation 5.3 gives us a method to extract the filling factor by fitting the Kondo resonance close to zero bias from the STS spectra.

Similar to the large-scale bias measurement, figure 5.5a shows the uniform topography image recorded simultaneously with the dI/dV signal, where each SoD clusters have a dot-like structure. However, the STS grid slicing at zero bias (Fig. 5.5) exhibits different patterns, where

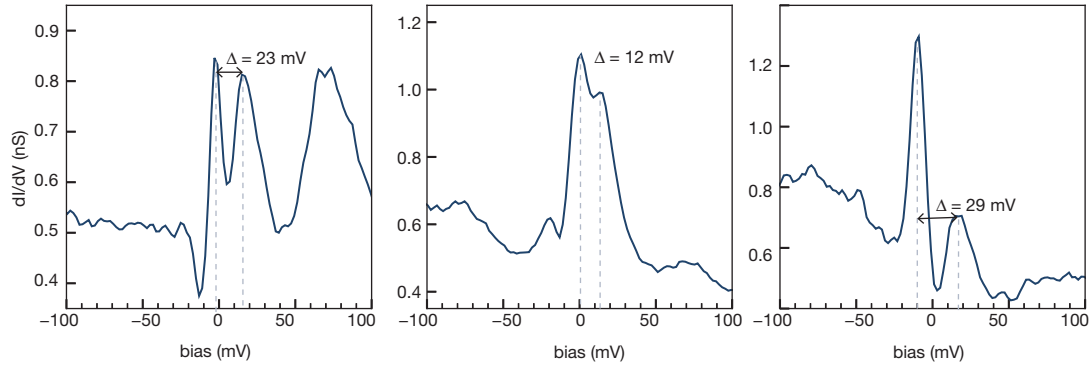

Figure 5.6: **Splitting of the zero bias peak.** The separations of the peaks are indicated by Δ.

each SoD cluster shows the homogenous hexagonal Mosaic pattern, but the electric property of the inter-clusters is different, indicating the localisation of the momentum is inside each SoD cluster. The inhomogeneity of the inter-clusters can be seen in the peak position V_k, the peak width Γ and the shape of the peak q. Using equation 5.3, we can derive the filling factor, which varies from -0.85 to 0.75, indicating the highly inhomogeneous doping level. According to equation 5.2, and adapting $\alpha = \pi$ [124], the Kondo temperature is 86 K given the experimental temperature of 6.5 K for the spectrum in Fig. 5.5c, and $T_k = 63$ K for the spectrum shown in Fig. 5.5d. According to the single impurity Anderson model, the Kondo coupling J_K is related to the Kondo temperature T_K, given by

$$k_B T_K = \sqrt{2\Delta \frac{U}{\pi}} \exp\left(J_K \rho\right)$$

where Δ is the hybridization, U is on-site Colomb interaction, and ρ is the density of states [137]. Varying the Kondo temperature indicates that the Kondo coupling is also not spatially homogeneous.

Furthermore, when the Kondo coupling and the doping effect are comparable, we observed some complex spectra shown in Fig. 5.6. There we observed that this zero-bias peak is separated into a doublet peak, and the separation width of these two peaks near the zero bias varies from 12 mV to 29 mV. These spectra need further work to develop a more advanced model to explain the splitting.

From our Fano fitting analysis, we extract filling factors ranging from $n_f = -0.85$ to $n_f = 0.75$, corresponding to a charge transfer of approximately ± 0.4 electrons per Star of David cluster. This variation suggests that different stacking configurations lead to charge transfers ranging from strong hole doping to moderate electron doping, consistent with recent DFT calculations [123].

Our observations of spatially inhomogeneous electronic structure and variable Kondo temperatures support the doped charge-transfer insulator interpretation [123] over the quantum spin liquid scenario [122]. Several key observations differentiate these scenarios.

A quantum spin liquid would exhibit uniform spinon excitations across the sample [138]. In contrast, we observe strong spatial inhomogeneity in the zero-bias conductance (Fig. 5.3a), inconsistent with a homogeneous spin liquid ground state. The variable filling factors and Kondo temperatures directly indicate spatially varying charge doping levels. This inhomogeneity arises from the incommensurate stacking of the 3×3 CDW in 2H-$NbSe_2$ underneath and the $\sqrt{13} \times \sqrt{13}$ CDW of 1T-$NbSe_2$, creating different local chemical potentials and charge transfers.

In conclusion, this chapter demonstrates that by applying voltage pulses to 2H-$NbSe_2$, we can successfully prepare a 1T-$NbSe_2$/2H-$NbSe_2$ heterostructure. 1T-$NbSe_2$ is a charge transfer insulator, and when layered atop a metallic substrate, it exhibits an intricate interplay between Kondo coupling and charge doping. We employed STS to investigate the electronic structure of the 1T-$NbSe_2$/2H-$NbSe_2$ heterostructure and found that these interactions give rise to a complex, spatially inhomogeneous insulator-to-metal transition. In certain SoD clusters with strong Kondo coupling, we observed a single zero-bias peak, which splits due to doping effects related to Mott physics. Conversely, in SoD clusters with weaker Kondo coupling, a gap-like feature appears at the Fermi level, suggesting a more insulating electronic structure. By fitting the Kondo peak to a Fano line shape, we determined both the filling value and Kondo temperature, providing essential parameters for future modelling of this system. In the following chapter, we further customize this system by placing a graphene layer atop the 1T-$NbSe_2$. This adjustment produces a uniform pattern that breaks the C_3 rotational symmetry, in contrast to the previously observed absence of long-range order.

6 Superlattice engineering in graphene and 1T-$NbSe_2$

6.1 Superlattice engineering in 2D vdW heterostructure

The weak vdW interlayer interaction in layered materials such as graphite and TMDs enables their exfoliation down to 2D limits. When reassembled into vdW heterostructures, these layers retain their intrinsic properties due to the weak vdW interaction. However, the proximity effect allows the electronic properties to couple across layers, giving rise to new quantum phenomena which do not exist in the individual layers. Using this effect, physicists can select 2D layers with tailored properties to realise specific quantum effects [139].

Furthermore, stacking two sheets of material with a small twist angle between their atomic lattices creates a moiré periodicity [14]. This misalignment leads to a variation in the interlayer tunnelling strength, which depends on the local stacking configuration. As a result, the tunnelling strength follows the moiré periodicity, generating non-Abelian gauge potentials commonly referred to as moiré potentials [140, 141]. Introducing moiré periodicity into a 2D heterostructure creates a superlattice that modulates the periodic potential within the system. In addition to moiré potentials, various other methods have been applied to engineer superlattices. However, the interest always remains in tuning the electronic structure, particularly in achieving a band with flat dispersion, as electrons in the bands with flat dispersion will experience suppressed kinetic energy and enhanced electron-electron interactions.

An intuitive way to understand the construction of bands with flat dispersion involves constructing a system of weakly coupled quantum dot states [139]. The bandwidth of the resulting quasi-particle combined states is determined by the coupling strength between the quantum dots, and the weaker coupling strength leads to a flat dispersion. This concept is realised through superlattice engineering. For example, in twisted TMD systems, the interlayer hybridisation follows the moiré periodicity. Locally modulated stacking order induces spatial variation in the band edges, which results in the opening of energy gaps at the high-symmetry band edges [142]. Such a gapped system can localise electrons in certain regions, resembling an array of quantum dots [143, 144].

6.1.1 Spontaneous symmetry-breaking

In flat bands, the suppression of electron kinetic energy enhances the relative significance of electron-electron interactions, making these systems prone to correlated quantum phases. In the framework of solid-state physics, Bloch's theorem provides a single-particle approximation where the symmetry of the Bloch wave function reflects the symmetry of the underlying lattice structure. However, flat bands deviate from this paradigm, as the electron dynamics are dominated by a many-particle Hamiltonian rather than single-particle approximations.

The dominated electron-electron interactions in flat bands often drive the system to mitigate the energetic costs of Coulomb interactions through correlation effects, which are prone to spontaneous symmetry breaking. By breaking a symmetry, the system transitions into a new phase, where correlation-induced energy gaps form. This process lowers the free energy and stabilises the newly ordered state by shifting occupied states to lower and unoccupied states to higher energy [145].

Experimentally, carefully tuning the Fermi level across flat bands has revealed spontaneous C_3 rotational symmetry breaking in a hexagonal lattice, leading to the emergence of a C_2 stripe phase, also known as the nematic phase. This phenomenon has been observed in 2D systems with flat bands, such as twisted bilayer graphene [146], twisted double bilayer graphene [147], and the Kagome lattice [148, 149]. These symmetry-broken phases are often associated with the emergence of unconventional superconductivity [150, 151, 26, 152]. Consequently, an approach for discovering new unconventional superconductors involves engineering flat bands through superlattice design, identifying symmetry-broken phases, and fine-tuning these systems near the symmetry-breaking regime to explore novel superconducting states.

6.1.2 Proximity graphene to Star of David charge density wave

Recently, Eva Andrei's group has reported an interesting case of stacking graphene on 1T-TaS_2, where charge modulations in the overlying graphene were attributed to periodic band hybridisation with the underlying 1T-TaS_2, forming a proximity-induced CDW, rather than simple screening effects or trivial co-tunnelling mechanisms [41]. Inspired by the powerful role of moiré periodicity as a tuning knob for electronic structures in vdW heterostructures, our idea is extended to explore the interplay between proximity effect and twist-angle control.

In this chapter, we developed a new method of superlattice engineering that combines the interplay of moiré physics and proximity effects. By stacking graphene on 1T-$NbSe_2$/2H-$NbSe_2$ and precisely controlling the twist angle, we engineered new superlattice structures. STM was employed to study the energy-resolved local electronic density of states with atomic resolution, enabling direct observation of the electronic features in these systems.

At a twist angle of approximately 9°, a near-commensurate super-moiré structure was achieved, where the commensurate graphene superlattice was approximately aligned with the 2×2 CDW superstructure of 1T-$NbSe_2$. Rotating the graphene to a twisted angle of 27° resulted in the formation of a $\sqrt{3}\times\sqrt{3}$ near-commensurate super-moiré. In both samples, the proximity

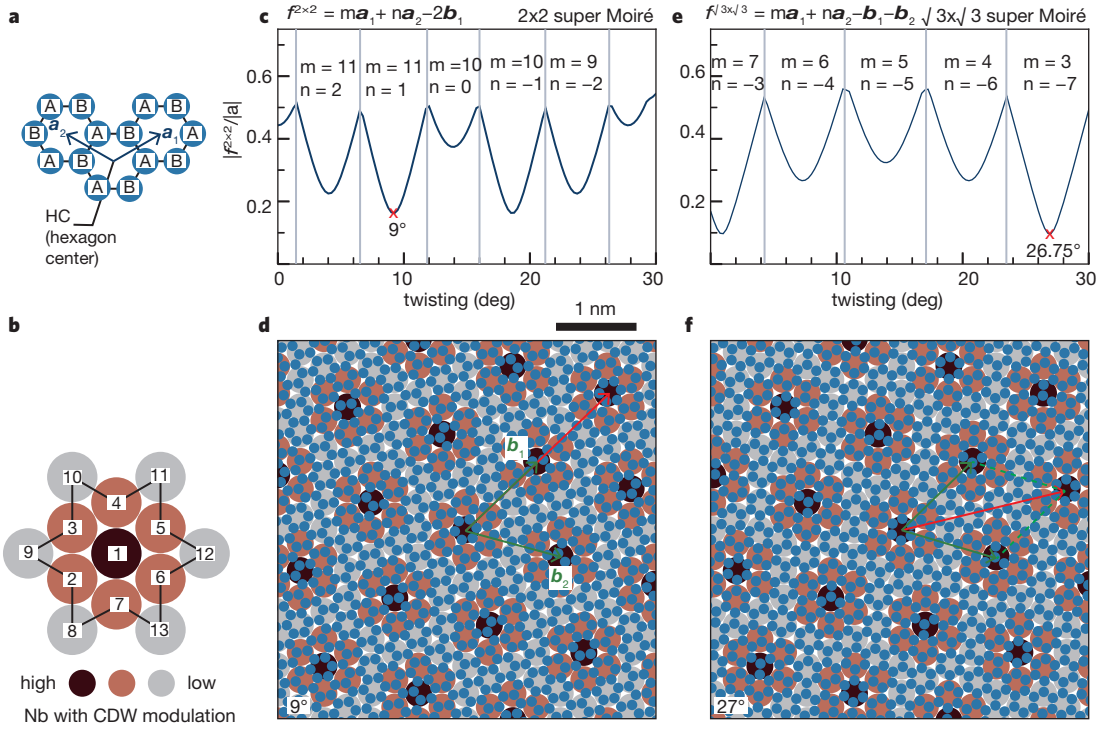

Figure 6.1: **Schematic illustration of the moiré pattern of graphene and 1T-$NbSe_2$. a,** Schematic structure of graphene, where A (B) labels the carbon atom at the A (B) sublattice-sites. **b,** Schematic structure of the Star of David cluster, which includes 13 Nb atoms at three different equivalent sites. **c,** Evaluation of the twisted angle dependent $f^{2\times2}$, with $f^{2\times2} = \min_{(m,n)} |m\mathbf{a}_1 + n\mathbf{a}_2 - 2\mathbf{b}_1|$. **d,** Evaluation of the twisted angle dependent $f^{\sqrt{3}\times\sqrt{3}}$, with $f^{\sqrt{3}\times\sqrt{3}} = \min_{(m,n)} |m\mathbf{a}_1 + n\mathbf{a}_2 - \mathbf{b}_1 - \mathbf{b}_2|$. **e,** Stacking configuration of graphene and 1T-$NbSe_2$ with a twist angle of 9° between graphene and $NbSe_2$. The green vectors $\mathbf{b}_1$ and $\mathbf{b}_2$ represent the primitive lattice vectors of the CDW superlattice. The red vector represents $2\mathbf{b}_1$. **f,** Stacking configuration of graphene and 1T-$NbSe_2$ with 27° twisted angle between graphene and $NbSe_2$. The red vector represents $\mathbf{b}_1 + \mathbf{b}_2$. Selenium atoms are omitted for clarity.

effect from 1T-$NbSe_2$ induced localised electronic states in graphene. Interestingly, a stripe phase with C_2 rotational symmetry was observed only in the $\sqrt{3} \times \sqrt{3}$ near-commensurate super-moiré at 27°, suggesting that the interplay of proximity effects and moiré periodicity can lead to exotic phenomena and tunable electronic behaviours.

6.2 Structural property of graphene on $NbSe_2$

6.2.1 Formation of the super moiré between the graphene and the CDW modulated $NbSe_2$

The formation of moiré patterns between two layers in 2D heterostructures arises from their relative misalignment. The most famous example is twisted bilayer graphene, which consists

of two graphene layers with a honeycomb lattice structure. Each unit cell in graphene contains two sublattices: A and B (Fig.6.1a). In twisted bilayer graphene, the local stacking configuration can be described by a parameter with two components, representing the relative alignment of the sublattices in the two layers. For instance, AA stacking refers to the alignment of the A-sublattice in the first layer directly above the A-sublattice in the second layer. In contrast, AB stacking occurs when the A-sublattice in the first layer aligns with the B-sublattice in the second layer.

The resulting moiré periodicity is defined as the distance between two regions with identical stacking configurations, such as one AA stacking region to the nearest AA stacking region. This periodicity depends on the twist angle between the two layers, making it a tunable parameter for engineering unique electronic and structural properties in 2D heterostructures.

In our heterostructure, $NbSe_2$ layer contains Nb atoms sandwiched between two Se atoms (see Fig.6.3a). This arrangement forms a triangular lattice, where the unit cell consists of one Nb atom and two Se atoms. When graphene is stacked on $NbSe_2$ without a CDW, the resulting graphene/$NbSe_2$ heterostructure requires a two-component parameter to describe its local stacking configurations, analogous to the approach used in twisted bilayer graphene.

In this heterostructure, the two components specify the relative alignment between the graphene layer and the $NbSe_2$ lattice. For example, the configuration (A, Nb) represents the alignment of the A-site sublattice of graphene directly above Nb atoms in the $NbSe_2$ layer, while (Hc, Nb) describes the hexagon centre of graphene positioned above an Nb atom. To investigate rotational symmetry in this system, the moiré periodicity is defined as the distance between two identical stacking configurations, such as the distance from one (Hc, Nb) alignment to the next (Hc, Nb) alignment.

In the previous chapter, we demonstrated that 1T-$NbSe_2$ exhibits a $(\sqrt{13} \times \sqrt{13})$R13.9° CDW, leading to the formation of SoD clusters. The presence of the CDW introduces spatial charge modulations that reduce the translational symmetry of the $NbSe_2$ lattice. As shown in Fig.6.1b, an SoD cluster consists of 13 Nb atoms exhibiting three distinct CDW modulation levels. The Nb atom at the centre of the SoD cluster, labelled Nb_1, displays the highest modulation. Surrounding Nb_1 are the six nearest neighbours with medium modulation, while the remaining Nb atoms at the edges of the SoD cluster exhibit the lowest modulation.

This CDW modulation complicates the stacking configuration in the Gr/$NbSe_2$ heterostructure, as the alignment has to consider the Nb atoms influenced by the CDW. For instance, the configuration (Hc, Nb_1) represents the graphene hexagon centre aligned with the Nb_1 atom at the centre of the SoD cluster, which has the highest charge modulation. Consequently, a super moiré periodicity in this heterostructure can be defined as the distance between successive (Hc, Nb_1) alignments. This super moiré periodicity differs from the conventional moiré periodicity, which considers only the misalignment between the graphene and the $NbSe_2$ lattice without accounting for the impact of the CDW.

6.2.2 Twisted angle dependent super moiré periodicity

To mathematically describe the twist angle-dependent super moiré periodicity, we start by defining the translation symmetry in graphene. The translation from one hexagon centre in graphene to another is given by:

$$\mathbf{a}_{\text{super}}(m,n) = m\mathbf{a}_1 + n\mathbf{a}_2, \tag{6.1}$$

where m and n are arbitrary integers multiplied by the primitive lattice vectors of graphene $\mathbf{a}_1$ and $\mathbf{a}_2$. Similarly, the translation between SoD cluster centres Nb_1 in 1T-$NbSe_2$ is defined by the CDW superlattice:

$$\mathbf{b}_{\text{super}}(j,k) = j\mathbf{b}_1 + k\mathbf{b}_2, \tag{6.2}$$

where j and k are arbitrary integers, and $\mathbf{b}_1$ and $\mathbf{b}_2$ are the primitive lattice vectors of the CDW superlattice in 1T-$NbSe_2$, which are registered by the supermatrix in respect to the $NbSe_2$ primitive lattice vectors of $\mathbf{c_1}$ and $\mathbf{c_2}$:

$$\begin{bmatrix}\mathbf{b}_1\\ \mathbf{b}_2\end{bmatrix} = \begin{pmatrix}3 & 1\\ -1 & 4\end{pmatrix}\begin{bmatrix}\mathbf{c}_1\\ \mathbf{c}_2\end{bmatrix}.$$

To achieve a commensurate super moiré pattern, the vectors $\mathbf{a}_{\text{super}}(m,n)$ and $\mathbf{b}_{\text{super}}$ have to satisfy the diophantine equation [153]:

$$\mathbf{a}_{\text{super}}(m,n) - \mathbf{b}_{\text{super}}(j,k) = 0.$$

However, in systems where the periodicities of the two lattices differ significantly and the interlayer interaction is weak, commensurate super moiré patterns are rarely observed. Instead, near-commensurate super moiré patterns are considered, satisfying:

$$\mathbf{a}_{\text{super}}(m,n) - \mathbf{b}_{\text{super}}(j,k) \approx 0.$$

To quantify the degree of commensurability, a parameter f is defined as

$$f\left(j,k\right) \equiv \min_{m,n} |\mathbf{a}_{\text{super}}(m,n) - \mathbf{b}_{\text{super}}(j,k)|.$$

Here, $f(j,k)$ characterizes how closely a graphene superlattice $\mathbf{a}_{\text{super}}(m,n)$ can match the given CDW superlattice $\mathbf{b}_{\text{super}}(j,k)$. In the extreme case of $f(j,k) = 0$, a perfectly commensurate super moiré superlattice is achieved.

We examine low-order (j,k) pairings to evaluate near-commensurate super moiré patterns between graphene and the CDW superlattice in 1T-$NbSe_2$. Beginning with $(j,k) = (2,0)$, denoted as $f^{2\times2} = f(2,0)$, the commensurability depends on the twist angle θ as the graphene layer is rotated relative to the $NbSe_2$ lattice:

$$f^{2\times2}(\theta) = \min_{m,n} |R(\theta)\,\mathbf{a}_{\text{super}}(m,n) - \mathbf{b}_{\text{super}}(2,0)|, \tag{6.3}$$

where $R(\theta)$ is rotating operator. Substituting equations 6.1 and 6.2 into above equation 6.4 gives:

$$f^{2\times2}(\theta) = \min_{m,n}|mR(\theta)\mathbf{a_1} + nR(\theta)\mathbf{a_2} - 2\mathbf{b_1}| \tag{6.4}$$

The numerical evaluation of equation 6.4 is shown in Fig.6.1c, which exhibits a zig-zag structure. At a twist angle of approximately 9°, $f^{2\times2}$ reaches a local minimum of 0.16 $|a|$, where $|a| = 0.24$ nm is the graphene lattice constant. This local minimum indicates the formation of a near commensurate condition as shown in Fig.6.1d. Next, we consider $f(1,1)$, which is denoted as $f^{\sqrt{3}\times\sqrt{3}}$. Similarly to equation 6.4, the twist angle dependence is given by:

$$f^{\sqrt{3}\times\sqrt{3}}(\theta) = \min_{m,n}|mR(\theta)\mathbf{a_1} + nR(\theta)\mathbf{a_2} - \mathbf{b_1} - \mathbf{b_2}|. \tag{6.5}$$

The result for $f^{\sqrt{3}\times\sqrt{3}}(m,n)$, shown in Fig.6.1d, also exhibits a zig-zag structure. At a twist angle approximately 27°, $f^{\sqrt{3}\times\sqrt{3}}$ reaches a local minimum of $0.09|a|$. In summary, the geometric stacking between graphene and the CDW modulation in 1T-$NbSe_2$ indicates the formation of near-commensurate super moiré patterns at specific twist angles. At 9°, the super moiré pattern is approximately aligned with the 2×2 CDW super moiré, while at 27°, the alignment is approximately with the $\sqrt{3}\times\sqrt{3}$ CDW super moiré.

6.3 Preparing 27° and 9° twisted graphene/$NbSe_2$ samples

In the previous section, we discussed that at twist angles of 9° and 27°, graphene and 1T-$NbSe_2$ with CDW modulation can form 2×2 and $\sqrt{3}\times\sqrt{3}$ near-commensurate super moiré structure, respectively. This section shows the experimental approach for studying these two angles. The samples are assembled using the method detailed in section 4.2. Both samples consist of monolayer graphene sheets placed on bulk 2H-$NbSe_2$, denoted as Gr/2H-$NbSe_2$. At first glance, both samples exhibit atomically clean surfaces, as evidenced by the atomic resolved STM topography(Fig.6.2a and b).

The FFT patterns for both Gr/2H-$NbSe_2$ samples (Fig.6.2c and d) reveal Bragg peaks corresponding to the graphene lattice, the $NbSe_2$ lattice, and the moiré pattern arising from the lattice mismatch between the two materials. We analysed the corresponding FFT patterns using the method described in Appendix A. The lengths of the reciprocal vectors of the moiré pattern in the three directions were found to be (11.065, 11.037, 11.097) nm^{-1} for the first sample corresponding to the moiré periodicity length (0.764,0.766,0.762)nm in real space and (14.528, 14.526, 14.451) nm^{-1} for the second sample corresponding to the periodicity length (0.501,0.502,0.504)nm in real space. From analyzing the moiré periodicity, the twist angles θ_s between the $NbSe_2$ and graphene lattices were determined to be 8.7° and 26.4°, respectively (Fig.6.2e and f). Accordingly, we labelled these samples as 9° sample and 27° sample . The uniaxial heterostrain values for these two samples were determined to be 0.17 % for 9° sample and 0.30 % for 27° sample . The strain could have been introduced during the sample preparation process, including mechanical exfoliation and stacking processes. These

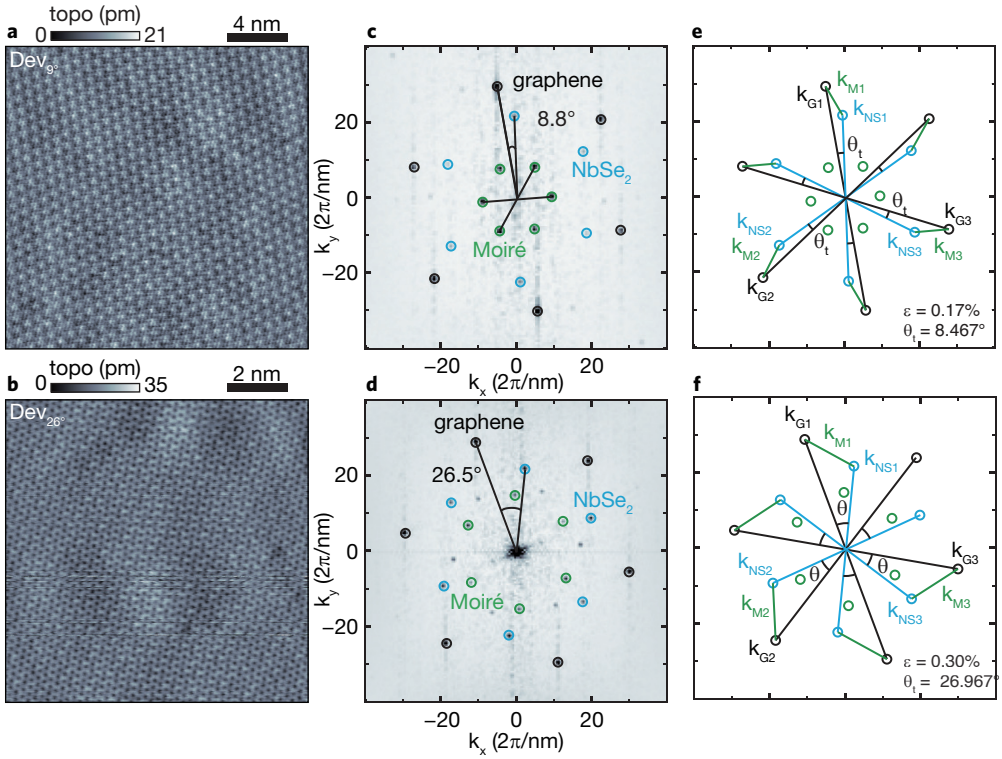

Figure 6.2: **Atomically resolved STM topographic images of the** 9° **sample and** 27° **sample in the** $NbSe_2$ **2H-phase**. **a,** STM topographical image of $Dev_{9°}$ (V = 50 mV, I = 100 pA). **b,** STM topographical image of $Dev_{26°}$ (V = 300 mV, I = 200 pA). **c,** FFT image of 9° sample showing the Bragg peaks corresponding to graphene, the 2H-$NbSe_2$ lattice, and the super moiré superlattice. **d,** FFT of 27° sample displaying similar Bragg peaks. **e** Analysis of the moiré pattern for 9° sample . **f,** Analysis of the moiré pattern for 27° sample . The top graphene layer is rotated with respect to the underlying 2H-$NbSe_2$, resulting in a new periodicity characterised by the reciprocal vectors connecting the individual reciprocal lattice vectors.

strain values are comparable to those observed in twisted bilayer graphene samples prepared using similar exfoliation and stacking techniques [154, 79].

To achieve the target structure of graphene stacking on 1T-$NbSe_2$, we applied voltage pulses ranging from 2 to 5 V across the STM tip-sample junction, following the method detailed in chapter 5. This procedure induces the structural transition of 2H-$NbSe_2$ underneath the graphene, resulting in the graphene being placed atop a single layer of $NbSe_2$ in the 1T phase on bulk 2H-$NbSe_2$ (Fig.6.3a). For clarity, we denote this stacking of heterostructure as Gr/1T-$NbSe_2$.

Figure 6.3b and c illustrate the phase boundary between Gr/2H-$NbSe_2$ and Gr/1T-$NbSe_2$ regions. In the Gr/2H-$NbSe_2$ region, the topography reveals a moiré pattern that changes with variations in the twist angle, reflecting the lattice mismatch and alignment between graphene and 2H-$NbSe_2$. In contrast, the Gr/1T-$NbSe_2$ region exhibits a "dots-like" hexagonal superlattice, indicating strong modulation of the graphene sheet by the underlying 1T-$NbSe_2$.

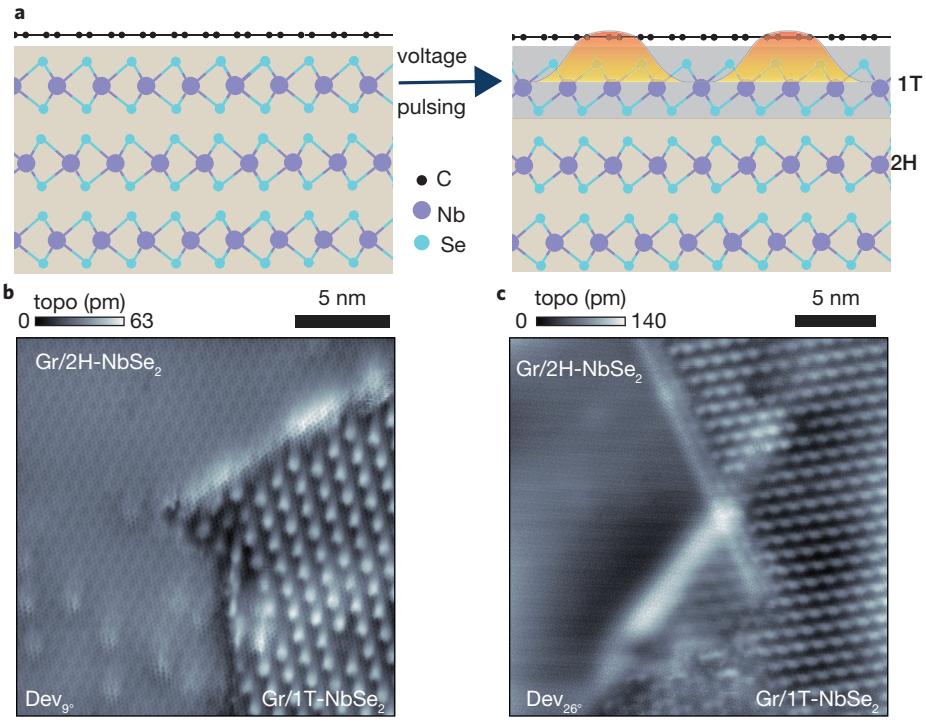

Figure 6.3: **Phase transition from Gr/2H-$NbSe_2$ to Gr/1T-$NbSe_2$. a,** Schematical side view showing the vertical structure before and after voltage pulsing. **b,** STM topography of the phase boundary between graphene/2H-$NbSe_2$ and graphene/1T-$NbSe_2$/2H-$NbSe_2$ of the sample with twisted angle of 9° (9° sample) (V = 650 mV, I = 100 pA). **c,**STM topography of phase boundary between graphene/2H-$NbSe_2$ and graphene/1T-$NbSe_2$ of the sample with twisted angle of 27° (27° sample) (V = 300 mV, I = 200 pA).

.

This hexagonal superlattice has a periodicity distinct from the moiré pattern observed in Gr/2H-$NbSe_2$.

6.4 Structure property of graphene on 1T-$NbSe_2$

To confirm that the target samples of graphene on 1T-$NbSe_2$ with twist angles of 9° and 27° are successfully achieved, we examine the structural and property features of both samples. The atomically resolved topography of Gr/1T-$NbSe_2$ is shown in Fig.6.4a and b. Analysis of the FFT patterns for both Gr/1T-$NbSe_2$ samples, as shown in Fig.6.4c and d, reveals that the periodicity of the observed modulation within the graphene layer corresponds to the $(\sqrt{13}\times\sqrt{13})$R13.9° of the 1T-$NbSe_2$. This observation indicates that the dots-like hexagonal superlattice modulating the graphene originates from the underlying CDW in the 1T-$NbSe_2$ phase, confirming the expected structural characteristics of the samples.

In comparison to the topography of 1T/2H-$NbSe_2$ shown in Fig.5.2 in Chapter 5, where the strong intensity of the CDW hinders the resolution of the atomic structure via STM probing,

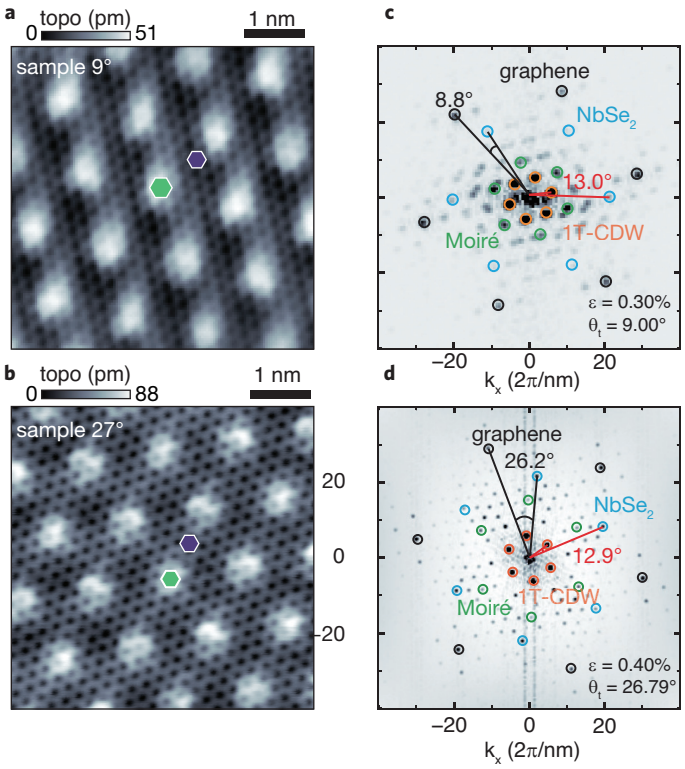

Figure 6.4: **Atomically resolved STM topographic images of the** 9° **sample and** 27° **sample in the** $NbSe_2$ **1T-phase. a,** STM topographical image of 9° sample ($I = 200$ pA, $V = 0.5$ V). A green hexagon shows the A-site, where the CDW reaches its maximum. A blue hexagon shows the B-site, located midway between two neighbouring A-sites. **b,** STM topographical image of 27° sample ($I = 60$ pA, $V = 0.3$ V). **c,** FFT image of 9° sample of $NbSe_2$ in 1T-phase. **d,** FFT image of 27° sample of $NbSe_2$ in 1T-phase.

the stacking of graphene on top of 1T/2H-$NbSe_2$ enables the resolution of both graphene and $NbSe_2$ atomic structures. This is evident as Bragg peaks corresponding to both lattices are present in the FFT patterns (Fig.6.4c and d). The atomically resolved topography enables us to determine the heterostrain values and the twisted angle by using the strain analysis method similar to the Gr/2H-$NbSe_2$. In both samples, the uniaxial heterostrain in Gr/1T-$NbSe_2$ was found to be comparable to that in Gr/2H-$NbSe_2$ prior to voltage pulsing. This structural analysis suggests that, due to the vdW interaction between graphene and $NbSe_2$, the phase transition of $NbSe_2$ underneath the graphene does not introduce significant strain to the graphene layer, nor does it alter the twist angle between graphene and $NbSe_2$.

6.5 Probing the electronic structure

In subsection 6.2.2, theoretical geometric stacking configurations demonstrate that graphene and 1T-$NbSe_2$ with a twisted angle of 9° correspond to the 2×2 near-commensurate super moiré structure, while a twisted angle of 27° aligns with the $\sqrt{3} \times \sqrt{3}$ near-commensurate

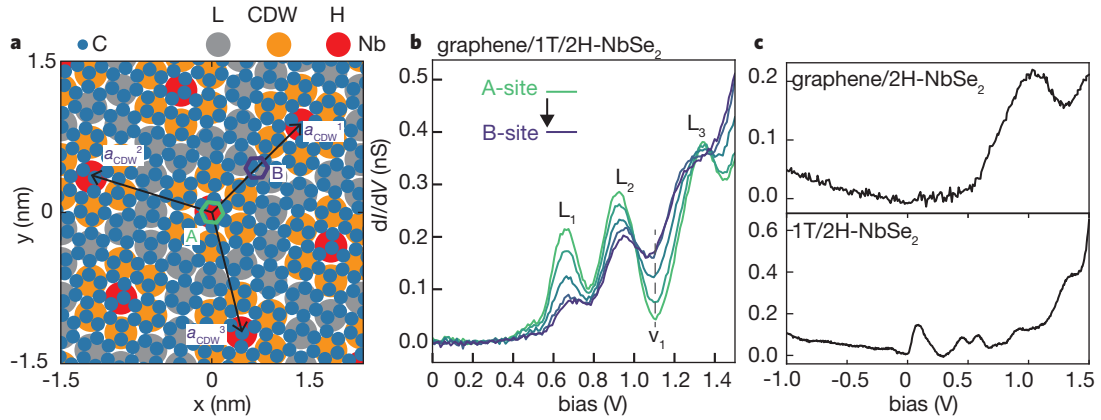

Figure 6.5: **STS Spectra on Gr/1T-$NbSe_2$ of 27° sample.** **a,** Schematic modelling of graphene/1T-$NbSe_2$ heterostructure, showing the A-site indicating the CDW maximum, and the B-site indicating the CDW minimum. **b,** STS spectra taken from the A-site to the B-site. (I = 100 pA, V = 1.5 V, and V_{mod} = 10 mV).**c,** STS spectra of graphene on 2H-$NbSe_2$ (upper) and 1T-$NbSe_2$ on 2H-$NbSe_2$ (lower). (upper: I = 100 mV, V =1.5 V and V_{mod} = 10 mV; lower: I = 200 mV, V =1.5 V and V_{mod} = 10 mV).

moiré structure. Having successfully achieved two samples with these two target angles, this section focuses on examining their electronic structures.

6.5.1 Probing electronic structure in 9° sample

To investigate the electronic structure of 9° sample , within the supercell of the CDW in 1T-$NbSe_2$, we define the A-site as the location where the CDW modulation reaches its maximum and the B-site as the position with the minimum CDW modulation, situated midway between two adjacent A-sites. A schematic representation of the A-site and B-site positions with twisted angle of 9° is provided in Fig.6.5a, with the corresponding positions in the STM topography indicated by green and blue hexagons in Fig.6.4a. STS spectroscopy, whose intensity is proportional to the LDOS, was conducted to probe these features.

Figure 6.5b shows the dI/dV spectra obtained by scanning from the A-site to the B-site. At the A-site, the dI/dV spectrum features three strong peaks above the Fermi energy. These three peaks can be fitted with the sum of three Gaussian peaks centred at 0.658 V, 0.923 V and 1.360 V with respective full width at half maximum (FWHM) of 0.173 V, 0.175 V and 0.332 V. We labelled these three peaks at the A-site as electronic level-1 (L_1), level-2 (L_2) and level-3 (L_3). Additionally, the valley position v_1 is located at the midpoint between L_2 and L_3 of 1.14 V.

As the probing tip moves from the A-site to the B-site, the differential conductivity of the three peaks decreases monotonically. However, at the B-site, the differential conductivity within the bias range of 1.0 V to 1.2 V, corresponding to the valley position between peaks L_2 and L_3, becomes stronger than that observed in the same bias range at the A-site. Consequently, the spatial distribution of the differential conductivity reverses, transitioning from being relatively higher at the A-site (weaker at the B-site) to higher at the B-site (weaker at the

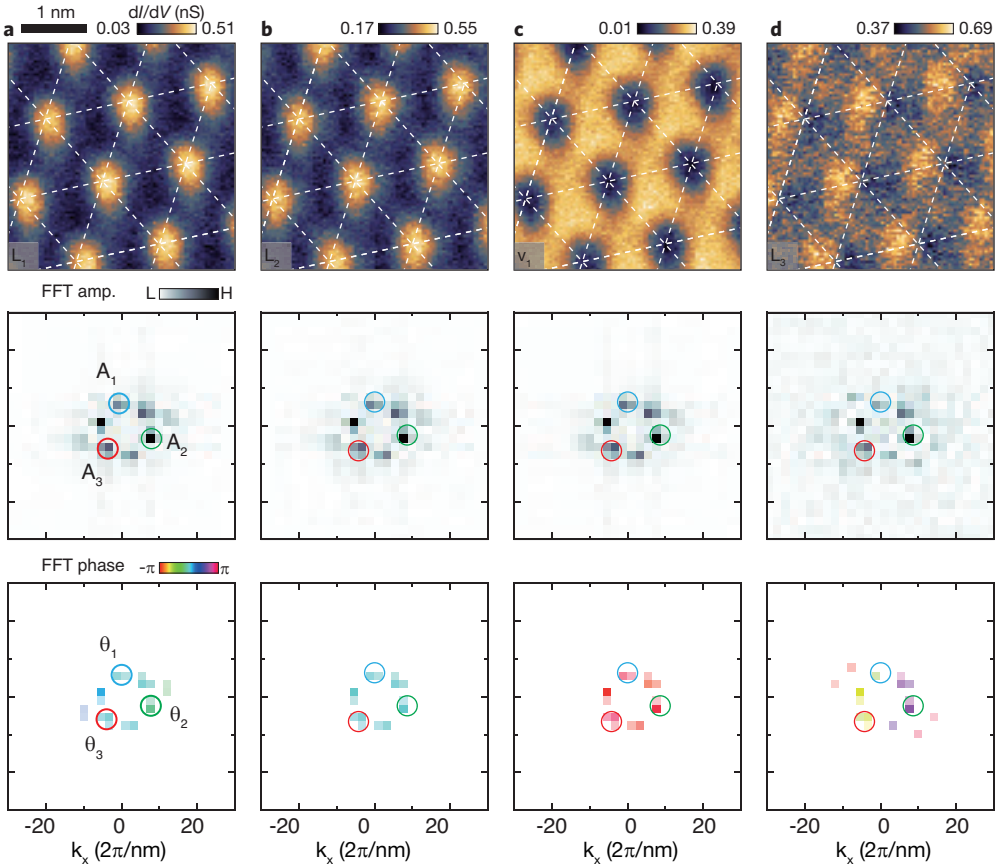

Figure 6.6: **STS grid measurement of** 9° **sample with the corresponding FFT amplitudes and FFT phases.a,** slicing at L_1 (0.66 V), **b,** L_2 (0.92 V), **c**, v_1 (1.14 V), and **d** L_3 (1.36 V). Their positions are indicated in Fig.6.5b.

A-site). This reversal in intensity corresponds to a π shift, which will be further examined in subsection 6.5.3. The observation of these three strong peaks in graphene on 1T-$NbSe_2$/2H-$NbSe_2$ is distinctive. These peaks are absent in the control measurements conducted on a 1T-$NbSe_2$/2H-$NbSe_2$ sample without graphene and a Gr/2H-$NbSe_2$ sample, where the CDW characteristic of 1T-$NbSe_2$ is not present (Fig.6.5c). This observation suggests that the unique electronic structure results from the interplay between the graphene layer and the underlying CDW modulation of 1T-$NbSe_2$.

Next, we examine the spatial distribution of the dI/dV signals corresponding to these energy levels. At the bias associated with L_1 and L_2, the dI/dV grids (Fig.6.6a and b) exhibit localised structures, with high differential conductivity concentrated at the A-sites. In contrast, at v_1, the differential conductivity pattern undergoes an inversion, transitioning from a localised structure to a mesh-like structure (Fig.6.6c), where the A-sites exhibit the lowest conductivity. Furthermore, at L_3, the spatial distribution of conductivity reverts to a localised structure, albeit with a noticeable offset from the A-site (Fig.6.6d).

We analysed the form factors corresponding to these energy levels and the valley position

using the form factor extraction method described in Section 2.4. The extracted amplitude and phase of the Bragg peaks are presented in the second and third rows of Fig.6.6. The FFT amplitude patterns consistently display a hexagonal arrangement, corresponding to the periodicity of the CDW in 1T-$NbSe_2$.

However, the FFT phase patterns exhibit variations among the energy levels. For L_1 and L_2, the phase of the form factors is $\{0,0,0\}$, corresponding to a dot-like structure. From L_2 to v_1, a π-shift occurs. The valley position v_1 exhibits a phase of $\{-\pi,-\pi,-\pi\}$, corresponding to the mesh-like structure. At L_3, the phase of the form factor changes to $\{-\pi/2,--\pi/2,\pi/2\}$. Considering the preservation of Hermitian symmetry, the phase at L_3 can be unwrapped to $\{-\pi/2,-\pi/2,-\pi/2\}$ for simplifying the interpretation.

6.5.2 Probing electronic structure in 27° sample

Before presenting the $\mathrm{d}I/\mathrm{d}V$ spectroscopy measurements of 27° sample , which corresponds to the $\sqrt{3}\times\sqrt{3}$ near-commensurate super moiré, we first examine the bias-dependent topographies in 27° sample (Fig.6.7). At a low bias of 0.3 V, the topography, which is the same image shown in Fig.6.4b, reveals the atomic resolution of the graphene layer, $NbSe_2$ lattice, and the CDW.

As the bias increases, the atomic resolution of the graphene and $NbSe_2$ layers becomes less distinct, and the CDW pattern undergoes a series of transformations. These changes include transitions from a dots-like pattern at 0.3 V to an ellipse-like pattern at 0.7 V, followed by a hexagonal pattern at 1 V, a striped pattern at 1.2 V, and a ring-like feature at 1.8 V. The bias-dependent evolution of the topography is corroborated by the corresponding FFT patterns. These patterns reveal the gradual disappearance of the graphene and $NbSe_2$ Bragg peaks with increasing. Additionally, they show changes in the intensity of the Bragg peaks associated with the CDW of 1T-$NbSe_2$, with a pronounced modulation in a specific direction, suggesting a breaking of C_3 rotational symmetry for the CDW superlattice.

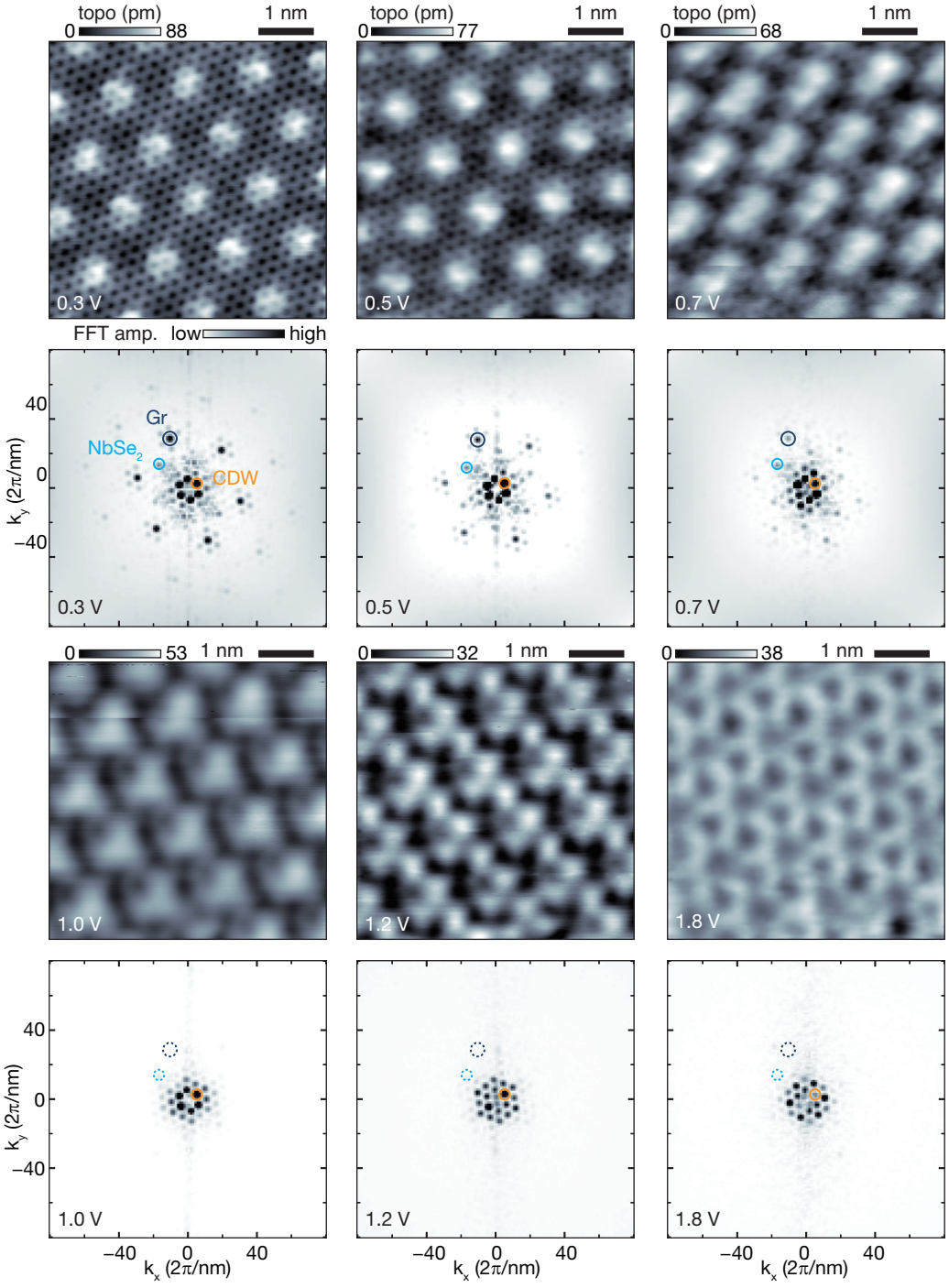

Figure 6.7: **Bias dependent topography of graphene on 1T-$NbSe_2$ of 27° sample . and the corresponding FFT images.** Black, blue and orange circles mark the Bragg peaks of graphene, $NbSe_2$ and the CDW of 1T-$NbSe_2$. (I = 60 pA and biases are indicated for each measurement.)

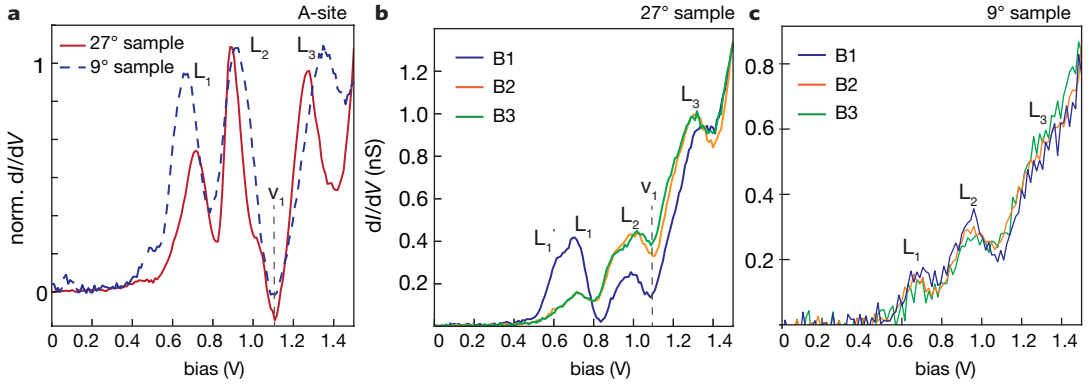

Figure 6.8: **Comparison of the STS spectra of the two samples. a,** dI/dV spectra taken at the A-sites in 9° sample (dotted blue line) and in 27° sample (solid red line). **b,** dI/dV spectra taken at B1 (blue), B2 (orange) and B3 (green)-sites separated by 120° of the 27° sample . (I = 500 pA, V = 1.5 V, V_{mod} = 10 mV). **c,** dI/dV spectra taken at B1 (blue), B2 (orange) and B3 (green)-sites separated by 120° in 9° sample (I = 100 pA, V = 1.5 V, and V_{mod} = 10 mV).

To investigate the electronic structure associated with the rotational symmetry breaking observed in the bias-dependent topography measurements of 27° sample , we first performed dI/dV spectroscopy at the A-site, which corresponds to the position where the CDW modulation of 1T-$NbSe_2$ reaches its maximum. The dI/dV spectrum at the A-site in 27° sample exhibits three prominent peaks, similar to those observed in 9° sample (Fig.6.8a). These peaks are located at approximately the same energy positions as in 9° sample . The reproducibility of these spectral features across varying twist angles between graphene and $NbSe_2$ indicates the dominant influence of the CDW modulation on determining the electronic structure of the heterostructure. However, variations in the stacking configuration due to the super moiré structure can subtly shift the energy positions of these peaks at the A-site.

To further analyze the C_3 rotational symmetry breaking, spectra were taken at the B1, B2, and B3 sites, which are rotated by 120° with respect to each other around the A-site (Fig.6.8b). The spectrum at B1 displays a side peak at lower energy than L_1, which we label as L_1'. Additionally, the spectrum at B1 exhibits higher differential conductivity at L_1 and L_1' compared to the spectra at B2 and B3. Conversely, at the L_2 position, the spectrum at B1 shows weaker conductivity than those at B2 and B3. Between L_1 and L_2, the spectra at B2 and B3 display almost identical conductivity. However, in the range from L_2 to L_3, these three spectra exhibit different slopes, resulting in no overlap in this region. Among the three spectra, the one at B1 has the lowest conductivity between L_2 and L_3. At the bias above L_3, all three spectra exhibit approximately the same conductivity. For control measurement, the corresponding dI/dV spectra measured at the B1, B2, and B3 sites in 9° sample are presented in Fig.6.8c. These spectra show nearly identical behaviour, with similar conductivities and trends across the energy range, unlike the distinct variations observed in 27° sample .

To further investigate the symmetry breaking, we performed STS grid measurements in 27° sample , as shown in Fig.6.9. Due to the presence of the anisotropy at B-sites, the dI/dV

grids of 27° sample show more complex bias-dependent dI/dV spatial distribution compared to the dI/dV grids measurements in 9° sample (Fig.6.6). This complex pattern is challenging to direct interpretation in real space. However, the Fourier transform is particularly effective for analyzing such complex spatial patterns because it decomposes the real-space distribution into its frequency components.

In the FFT images, six prominent peaks correspond to the Bragg peaks of the CDW of 1T-$NbSe_2$, associated with the reciprocal vectors $G_i (i = 1,2,3)$. Since the FFT is a complex-valued function, both the FFT amplitude and FFT phase patterns are presented in Fig.6.6. It is noteworthy that the phase plays a crucial role in analyzing the observed real-space patterns. For example, at a bias of 0.71 V, the FFT amplitude patterns show stronger intensities at G_1 compared to G_2 and G_3. This amplitude distribution is similar to that observed at 1.06 V. However, due to the phase difference between them, the corresponding real-space dI/dV patterns are completely distinct.

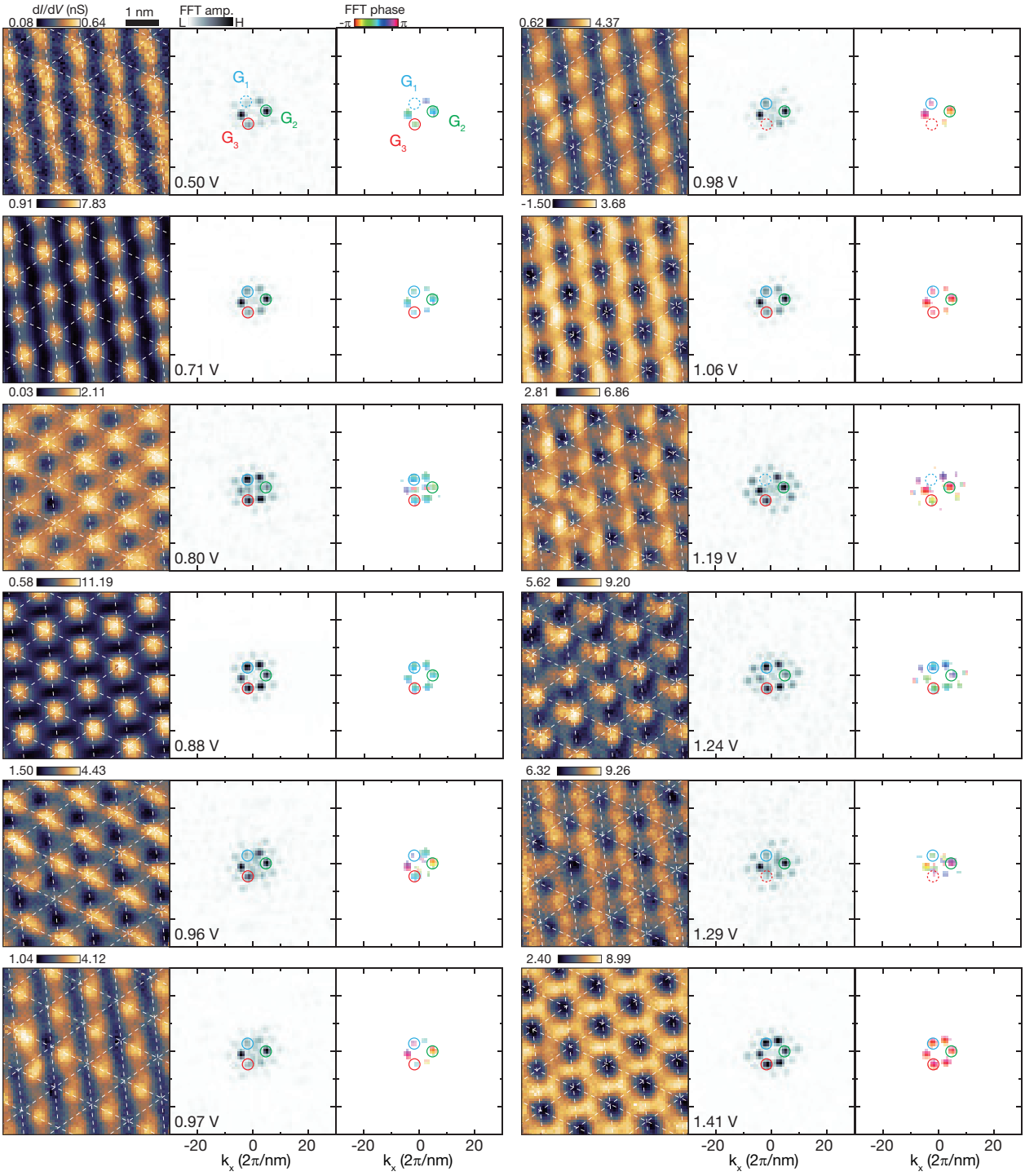

Figure 6.9: **STS grid measurement of 27° sample with the corresponding FFT amplitudes and FFT phases.**

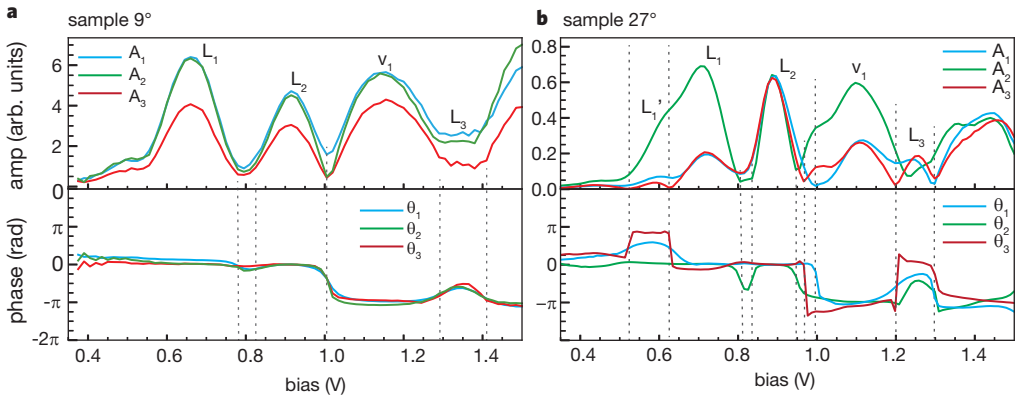

Figure 6.10: **form factors as a function of bias. a,** form factors for the 9° sample. **b,** form factors for the 26° sample.

Table 6.1: **Summary of amplitude relationships, phases of form factors, and corresponding symmetries of** 27° **sample .**

position	amplitudes relation	$\{\theta_1,\theta_2,\theta_3\}$	symmetry
L_1'	$A_2 > A_1 > A_3$	$\{\pi/2,0,\pi\}$	
L_1	$A_2 > A_1 = A_3$	$\{0,0,\approx 0\}$ [a]	C_{2v}
L_2	$A_2 = A_1 = A_3$	$\{0,0,0\}$	C_{3v}
v_1	$A_2 > A_1 = A_3$	$\{-\pi,-\pi,-\pi\}$	C_{2v}
L_3	$A_3 > A_1 > A_2$	$\{-\pi/4,-\pi/2,0\}$	
above L_3	$A_1 \approx A_2 \approx A_3$	$\{-\pi,\approx -\pi,\approx -\pi\}$	C_{3v}

[a] The symbol ≈ indicates that $\theta_3 \approx 0$; it does not satisfy a strict equivalence.

6.5.3 Evaluation of the form factors

Quantitative analysis was conducted by extracting the form factors at each bias along the three directions which are rotated by 120° with respect to the $k = [0,0]$, Γ point of the FFT, denoted as $\{\psi_1,\psi_2,\psi_3\}$. The form factor for each direction is expressed as:

$$\psi_i(V) = A_i(V)\exp\left(i\theta_i(V)\right)(i = 1,2,3), \tag{6.6}$$

where $A_i(V)$ and $\theta_i(V)$ are the amplitude and phase as functions of bias, respectively. The amplitudes and phases as functions of bias for 9° sample and 27° sample are shown in Fig.6.10a and b, respectively. For 9° sample , the Bragg peaks associated with these three form factors are highlighted by cyan, green, and red circles in Fig.6.6. Similarly, for 27° sample , the Bragg peaks corresponding to the form factors are marked with the same colours in Fig.6.9.

For 9° sample , the amplitudes A_1 and A_2 remain nearly equal across the bias range from 0 V to 1.5 V, while A_3 consistently exhibits a lower value compared to the other two (Fig.6.10a). This anisotropy may arise from thermal drift or tip artefacts. The amplitudes A_1, A_2, A_3 exhibit a "three-peak" structure, with bias positions corresponding to L_1, L_2, and v_1 as observed in

the $\mathrm{d}I/\mathrm{d}V$ spectra (Fig.6.5b).

In 9° sample , the three form factors exhibit approximately similar values at each bias value, allowing us to use a single form factor to represent all three directions. The amplitude values of these form factors are related to the differential conductivity contrast between the A-site and B-site: $(\mathrm{d}I/\mathrm{d}V)|_{\text{A-site}} - (\mathrm{d}I/\mathrm{d}V)|_{\text{B-site}}$. At L_1 and L_2, the patterns are highly localised at the A-site, as the phase values remain close to 0. In the valley position v_1, the phase transitions from 0 to $-\pi$, leading to a stronger $\mathrm{d}I/\mathrm{d}V$ signal at the B-site compared to the A-site. For L_3, the contrast between the A-site and B-site becomes less pronounced, which explains the absence of a peak feature in the form factor as a function of bias. However, the phase jump from $-\pi$ to $-\pi/2$ indicates a shift in the maximum conductivity position from the B-site to a location between the A-site and B-site. These two-phase jumps between L_2 and v_1 and between v_1 and L_3 align with the local minimum of the amplitude. A Similar phenomenon in the phase jump coinciding with the amplitude reaching a local minimum has also been observed in the Kagome lattice [155]. This detailed analysis aligns with the real-space $\mathrm{d}I/\mathrm{d}V$ grid observations presented in Fig.6.6, confirming the consistency between the form factor analysis and $\mathrm{d}I/\mathrm{d}V$ grids.

At the amplitude minimum, the system undergoes a transition between two distinct electronic configurations. The amplitude $|A_i(V)|$ of the form factor quantifies the contrast in the local density of states between high-symmetry positions (A-sites and B-sites), while the phase $\theta_i(V)$ determines which position exhibits higher LDOS. When the amplitude approaches zero, the LDOS at A-sites and B-sites become nearly equal, creating a critical point where the system can smoothly switch between configurations at minimal energetic cost.

Similar physics has been observed in Kagome metals [155], where the interplay between van Hove singularities and electronic correlations drives analogous phase transitions, and in twisted bilayer graphene systems [79], where competing stacking configurations produce comparable effects.

The sharpness of the phase jumps in our measurements suggests that the transition occurs over a narrow energy range (< 50 meV), indicating relatively weak mixing between the two configurations. This observation is consistent with the weak van der Waals coupling between graphene and 1T-$NbSe_2$, which allows both layers to largely retain their intrinsic properties while still exhibiting hybridisation-induced modifications at specific energies.

The interesting results come from the form factors of 27° sample , where the three form factors exhibit distinct behaviours. Unlike 9° sample , where a single form factor is sufficient to describe the observed $\mathrm{d}I/\mathrm{d}V$ grid patterns, 27° sample requires all three form factors. The amplitudes of these form factors also show a "three-peak" feature in the same bias range. However, the "first peak" and the "third peak" display an asymmetry that contrasts with the symmetric peaks observed in 9° sample . This asymmetry of the "first peak" originates from the emergence of a side peak at a lower energy position than L_1, which aligns with the energy position of L_1' (Fig.6.8).

At L_1', the phase of ψ_3 undergoes sharp jumps, transitioning from approximately 0 to π

and then back to 0. These phase jumps align with the positions of the valley (local minimum) in the amplitude A_3. For ψ_2, the phase exhibits a smooth transition from 0 to $\pi/2$ and back to 0, without any abrupt jumps. For ψ_1, the phase remains constant at 0 within this range. At L_1, the amplitude of ψ_3 equals the amplitude of ψ_1, while ψ_2 has a significantly larger amplitude than the other two. As the bias increases, all three form factors at L_2 converge to exhibit the same amplitude and phase of 0. Between L_2 and υ_1, a phase jump from $\{0,0,0\}$ to $\{-\pi,-\pi,-\pi\}$ occurs, similar to the behaviour in 9° sample . However, in 27° sample , these phase jumps occur at slightly different energy positions: ψ_2 starts its transition at the lowest bias, followed by ψ_3, and finally ψ_1 at the highest bias. These staggered jumps correspond to the three distinct valley positions in the amplitudes. As the bias continues to increase, a new phase jump from $\{-\pi,-\pi,-\pi\}$ to $\{-\pi/4,-\pi/2,0\}$ occurs at 1.2 V, corresponding to L_3, and then reverts to $\{-\pi,-\pi,-\pi\}$ at 1.3 V. Beyond L_3, all three form factors exhibit approximately the same amplitudes and phases.

As discussed in Section 2.4.1, the relationship between the form factors and spatial symmetry enables us to evaluate the spatial symmetry of the electronic structure at various biases. These results are summarized in Table 6.1. At L_1' and L_3, differences in amplitudes and phases among the form factors lead to symmetry breaking. At L_1 and υ_1, the symmetry is reduced from the original $C_{3\upsilon}$ to $C_{2\upsilon}$, with $A_1 = A_3$. The phases are $\{0,0,0\}$ for L_1 and $-\{\pi,-\pi,-\pi\}$ for υ_1. At L_2 and biases above L_3, the system retains $C_{3\upsilon}$ symmetry as $\psi_1 = \psi_2 = \psi_3$.

6.6 Candidate Theoretical modellings

After presenting the experimental observations, this section discusses the theoretical perspectives from the DFT and tight-binding models. The calculations presented in this section are done by our collaborator Dr.Lennart Klebl. The observed symmetry-breaking states, located several hundred mV away from the Fermi level, challenge the idea that these phenomena arise from electron correlations or Peierls transitions, as both mechanisms typically observed a few $k_B T$ around the Fermi level.

6.6.1 DFT modelling

We begin with the DFT calculations, considering a system comprising graphene positioned atop 1T-$NbSe_2$ with its SoD CDW structure. In the initial configuration, the centre of the graphene hexagonal ring is aligned with a niobium atom, which means the rotational centre of the graphene coincides with the rotational centre of the 1T-$NbSe_2$ lattice (Fig.6.11a). This alignment preserves the C_{3V} symmetry of the system. However, when the graphene layer is shifted relative to the 1T-$NbSe_2$ lattice, the alignment of the rotational centres is disrupted, resulting in a broken C_{3V} symmetry (Fig.6.11b).

Figure 6.11c presents the calculated band structure of 1T-$NbSe_2$ within the mini-Brillouin zone corresponding to the SoD supercell. This calculation aligns well with the results reported

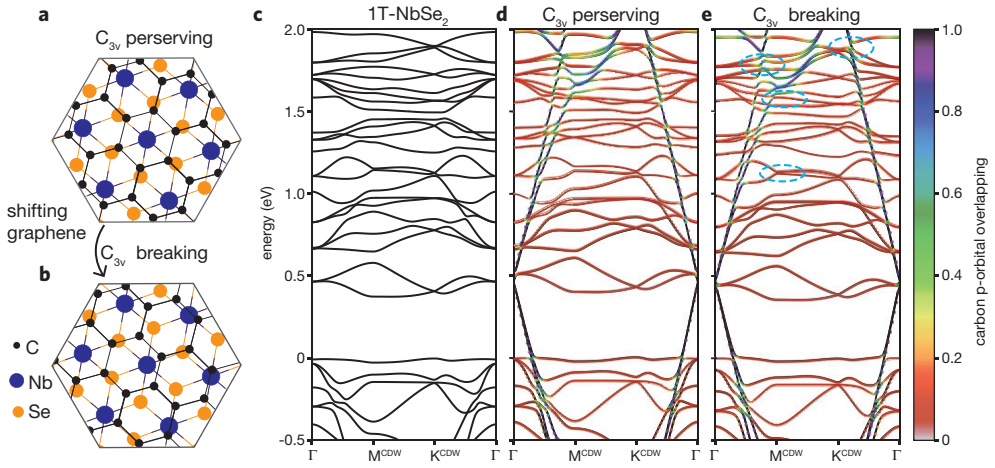

Figure 6.11: **DFT-calculated band structure of graphene on 1T-NbSe$_2$. a,** Stacking configuration of grahene on 1T-NbSe$_2$ preserving the C_{3V} symmetry. **b,** Stacking configuration of grahene on 1T-NbSe$_2$, where Shifting the graphene relative to the 1T-NbSe$_2$ lattice breaks the C_{3V} symmetry. **c,** DFT calculated band structure of 1T-NbSe$_2$ along the path $\Gamma - M^{\mathrm{CDW}} - K^{\mathrm{CDW}} - \Gamma$ connecting the high-symmetry points of the mini-Brillouin zone corresponding to the SoD supercell. **d,** DFT calculated band structure of graphene on 1T-NbSe$_2$ with preserved the rotational C_{3V} symmetry. **e,** DFT calculated band structure of graphene on 1T-NbSe$_2$ with broken the C_{3V} rotational symmetry.

in Ref.[156]. The flat band at the Fermi level is a famous feature of the SoD CDW, associated with Nb-d_{z^2} orbital, which hybridizes with Se-p orbitals around the Γ point. Our interest is in a series of bands within the energy range of 0.4-1.5 V. These bands are attributed to two hybridization Nb-$d_{yz} + d_{xz}$ orbitals with Se-p orbitals near the Γ point, and Nb-$d_{xy} + d_{x^2-y^2}$ orbitals with Se-p orbitals.

The band structure of graphene is characterized by its linear dispersion, commonly referred to as the Dirac cone. When graphene is placed on 1T-NbSe$_2$, the Dirac cone is folded into the mini-Brillouin zone, positioning the Dirac point at the Γ point (Fig.6.11d). Due to the weak vdW interaction, the coupling between graphene and 1T-NbSe$_2$ is weak, allowing both layers to largely retain their intrinsic electronic structures. However, at points where the Dirac cone of graphene intersects with the bands of 1T-NbSe$_2$, hybridization occurs between the p-orbitals of carbon atoms and the bands of 1T-NbSe$_2$, leading to the opening of a gap at the intersection. This interaction introduces subtle modifications to the electronic properties of the heterostructure. Additionally, when the graphene layer shifts relative to the 1T-NbSe$_2$ lattice, further modifications in the electronic structure are observed, as highlighted by the blue dotted circle in Fig.6.11e.

Figure 6.12a presents the DFT-calculated LDOS spectra at the A-site (centre of the SoD) and the B-site (valley position). Both positions exhibit five prominent peaks at identical energy levels, labelled as L_0 through L_4. Notably, the LDOS intensity at the A-site is higher than that at the B-site for all five levels. Consequently, the LDOS maps at these energy levels manifest

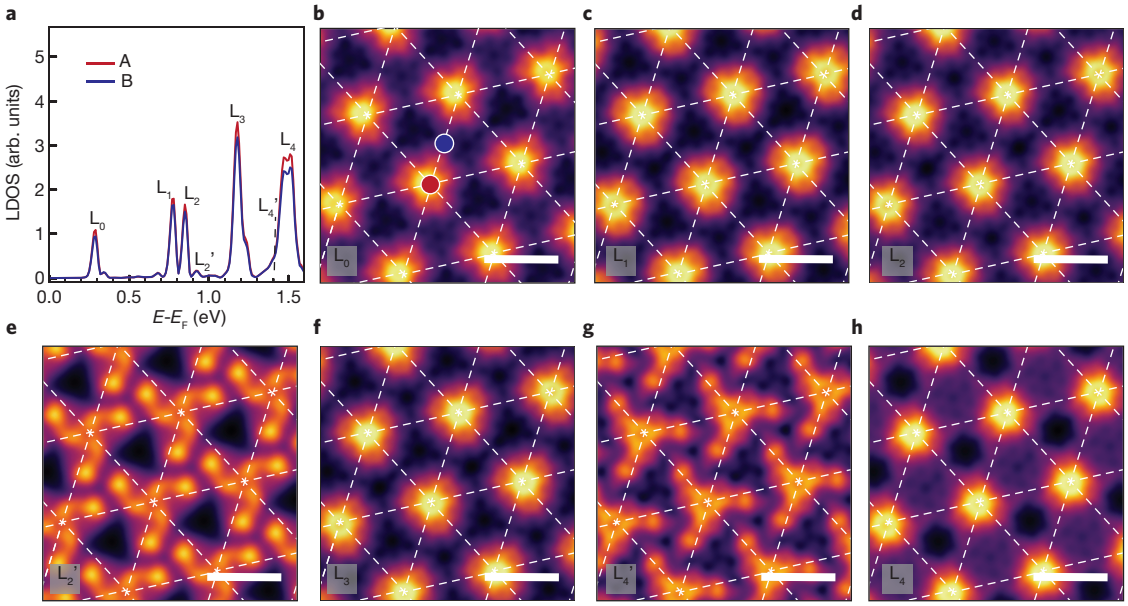

Figure 6.12: **DFT calculation of the LDOS of the C_{3v} symmetry preserving configuration. a,** DFT calculations of the LDOS on the center of SoD, and the valley position. These two positions are indicated by red (centre) and blue (valley) dots in panel **b**. **b-h** LDOS map at various energies indicated in panel **a** (Scale bars 1 nm).

localized dots-like features. These dots-like structures correspond well with the experimental dI/dV measurements observed at biases of 0.65 V and 0.92 V (Fig.6.6).

At an energy slightly above L_2, an additional small peak, labelled L_2', emerges. The LDOS map at this energy reveals a Triskelion-like structure that reduces the C_{3v} symmetry to C_3. A similar Triskelion pattern is observed at the energy level L_4', situated slightly below L_4. The alternating occurrence of dots-like and Triskelion structures is reminiscent of patterns reported in twisted double bilayer graphene [147], where the first remote conduction band exhibits Triskelion-like features, while the second remote conduction band shows dots-like structures.

As a result of the minor changes in the band structure caused by shifting the graphene relative to 1T-$NbSe_2$, the LDOS spectrum at the centre of the SoD (Fig.6.13a) remains largely similar to the spectrum shown in Fig.6.12a. To investigate the symmetry breaking, three valley sites separated by 120° are analyzed, with their corresponding spectra shown in Fig.6.13b. Among these, the LDOS spectra at valley 2 and valley 3 are identical, whereas valley 1 consistently exhibits a higher intensity compared to the other two valley postions. This anisotropy in LDOS intensity indicates that the system no longer retains C_3 rotational symmetry, instead exhibiting C_2 rotational symmetry.

The LDOS maps also show localized dots-like structures corresponding to these strong electronic levels. This suggests that these localized dots-like features are stable and robust against the relative shifting of the graphene layer. However, the LDOS maps at L_2' and L_4' reveal

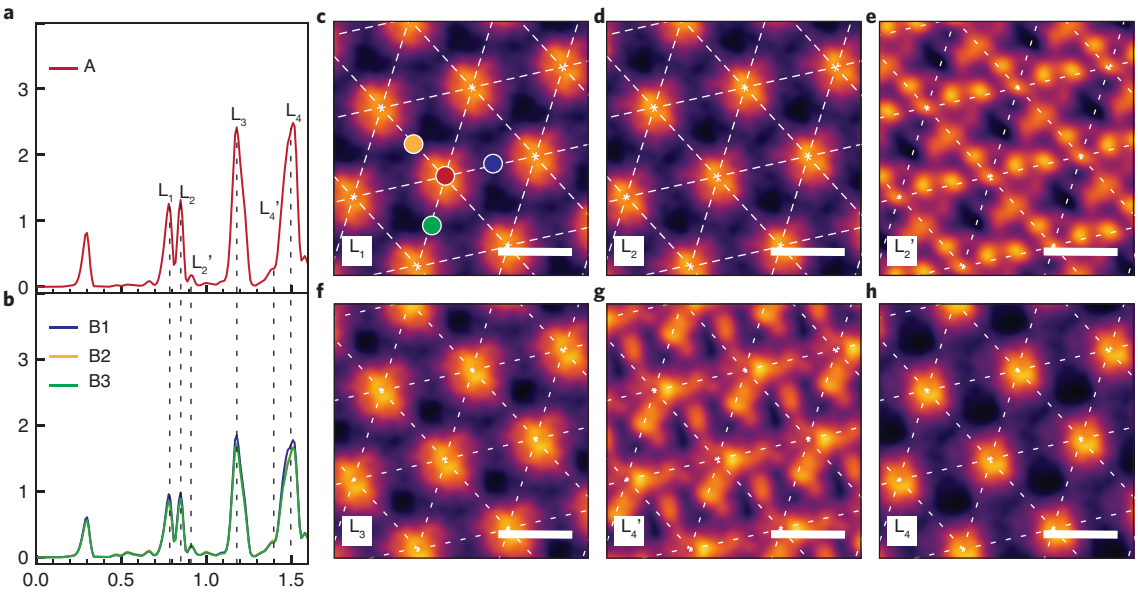

Figure 6.13: **DFT calculation of the LDOS of the C_{3v} symmetry breaking configuration. a,** DFT calculations of the LDOS on the center of SoD. The position is indicated by a red dot in panel **c**. **b,** the LDOS on the three valley positions separated by 120°. The spectrum of valley 2 overlaps with the spectrum of valley 3. These valley positions are indicated by orange, green and blue dots in panel **c**. **c-h** LDOS map at various energies indicated in panel **a** (Scale bars 1 nm).

more complex patterns, indicating that these specific states are highly sensitive to the shifting of the graphene.

6.6.2 Insights and unanswered questions from DFT

The DFT calculations provide insights into explaining the spectroscopic features observed in the experiments. One key observation is the appearance of strong peaks in the dI/dV spectrum, which are present only when graphene is placed on 1T-$NbSe_2$ and are absent in graphene on 2H-$NbSe_2$ or in bare 1T-$NbSe_2$. The results from DFT calculations attribute this phenomenon to the weak coupling between graphene and $NbSe_2$, where each layer largely retains its intrinsic electronic properties. However, at points where the Dirac cone of graphene intersects with the bands of 1T-$NbSe_2$, hybridization occurs, leading to the opening of a gap at these intersections. This hybridization flattens the bands and results in the strong peaks observed in the dI/dV spectrum, localized at the sites of the SoD clusters.

Furthermore, these localized patterns exhibit stability; shifting the graphene layer does not change their presence. However, alongside the prominent dots-like structure, some non-localized patterns are sensitive to the stacking configuration. As the graphene layer is shifted, these patterns evolve into more complex structures. This finding qualitatively explains why the localized dots-like feature is consistently observed across various samples with different

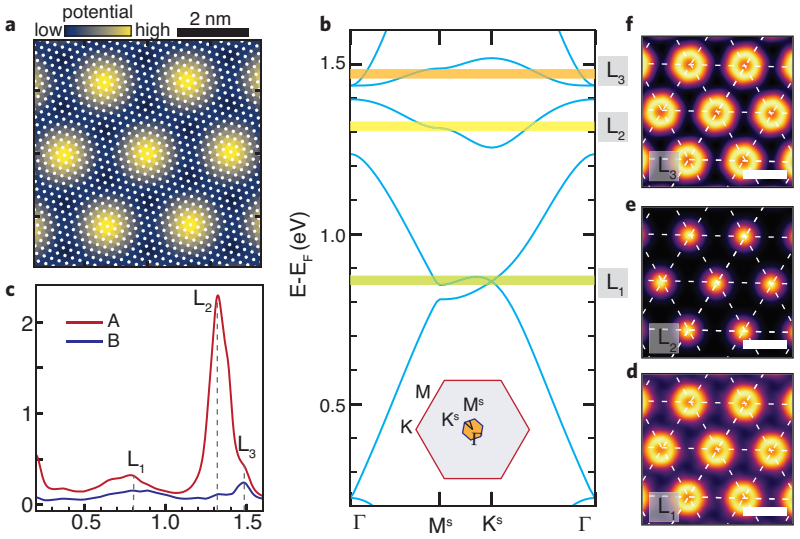

Figure 6.14: **Tight binding model for the C_{3v} symmetry potential. a,** potential modulation map on the graphene sheet. **b,** tight-binding calculated band structure along the high symmetry points of the mini-Brillouin zone. The insert shows the Brillouin zone of the graphene lattice and the mini-Brillouin zone induced by the potential modulation. **c,** LDOS spectra at A-site and B-site. **d** LDOS maps take at L_1, **e,** at L_2, and **f,** at at L_3 (Scale bars 1 nm).

twist angles, while the stripe phase with C_2 rotational symmetry is only detected in 27° sample .

However, there are several questions that DFT calculations cannot answer. First, while the DFT results predict five prominent peaks in the energy range of interest, only three strong peaks are observed experimentally in the dI/dV spectrum. One possible explanation is that the DFT calculations do not account for electron-electron interactions. When such interactions are considered, it is possible that the L_0 energy level participates in the formation of Hubbard bands, altering the characteristics of this band. Additionally, the L_4 peak is located at a higher energy position compared to the DFT prediction. This position is beyond the experimental measurement range.

Additionally, the DFT calculations fail to reproduce the phase shifts of π observed experimentally at approximately 1.0 V, where the LDOS intensity at the A-site is consistently greater than at the B-site. Furthermore, due to limitations in the unit cell size used for the calculations, the DFT method cannot be employed to construct the $\sqrt{3}\times\sqrt{3}$ or 2×2 supercells. Most significantly, while the DFT calculations do suggest minor C_{3v} rotational symmetry breaking when the graphene layer is shifted, this symmetry breaking is far less pronounced compared to what is observed experimentally.

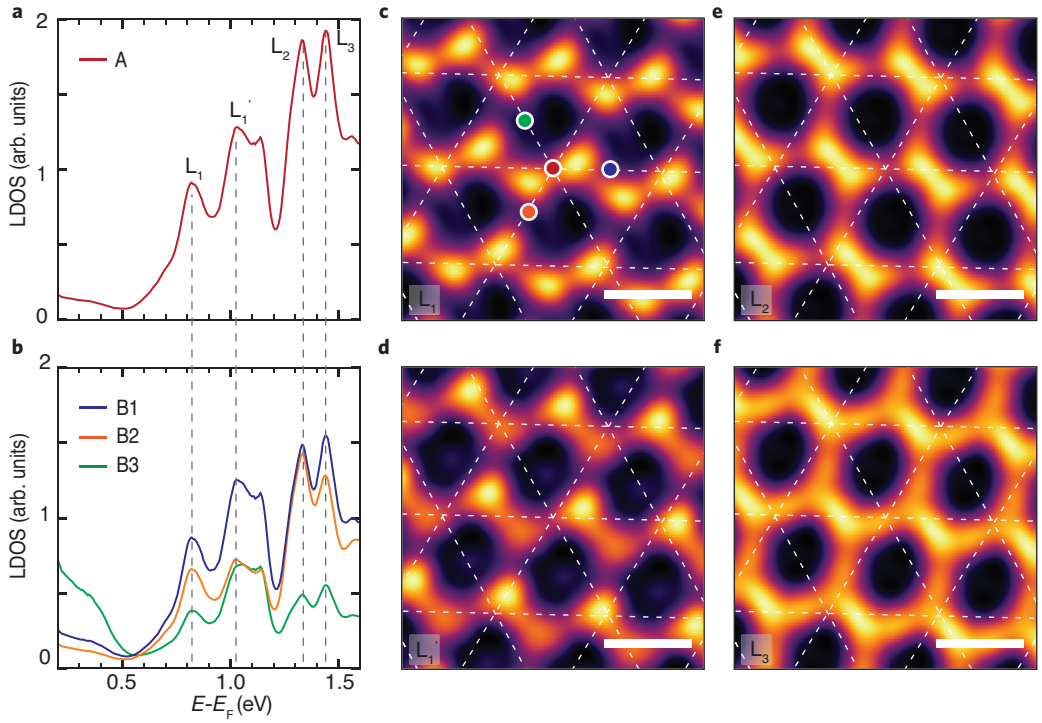

Figure 6.15: **Tight binding calculation of the distorted potential modulation. a,** Calculated LDOS spectrum at the A-site. The position is marked by a red dot in panel **c**. **b,** Calculated LDOS spectra at B-sites, separated by 120°, indicated by blue, orange, and green dots in panel **c**. **c,** LDOS map sliced at L_1, **d,** at L_1', **e,** at L_2, and **f,** at L_3' (Scale bars 1 nm).

6.6.3 Tight-binding model

Mimicking the moiré potential and inspired by the DFT calculations indicating weak coupling between the graphene layer and 1T-$NbSe_2$, we construct a tight-binding model that focuses solely on the graphene layer. In this model, the CDW in the underlying 1T-$NbSe_2$ provides a periodic onsite potential to the overlying graphene sheet, as illustrated in Fig.6.14a. This potential modulation creates a supercell in real space, corresponding to a mini-Brillouin zone in reciprocal space. The corresponding band structure is presented in Fig.6.14b. Three flat dispersions labelled as L_1, L_2 and L_3 are labelled. Among them, L_2 is isolated from other bands. The LDOS spectrum at the A-site (Fig.6.14c) reveals three prominent peaks corresponding to these three levels. Interestingly, these peaks are absent in the LDOS spectrum at the B-site, suggesting that the states are highly localised at the A-site. The LDOS maps corresponding to these three levels are presented in Fig.6.14d-f. Among these states, the LDOS distribution for L_2 (Fig.6.14e) displays a more pronounced dots-like structure compared to the other two levels, where L_1 and L_3 exhibit ring-like structures.

To reproduce the experimentally observed stripe-like electronic structure, the onsite potential in the tight-binding model was manually distorted. The corresponding LDOS spectrum at the A-site (Fig.6.15a) displays multiple prominent peaks, deviating from the results obtained

with the symmetric onsite potential. A new peak, denoted as L_1', emerges between L_1 and L_2, while the intensity of L_3 becomes significantly stronger compared to the symmetric potential case. The LDOS spectra at three different B-sites exhibit similar peaks as those at the A-site, but with weaker intensities (Fig.6.15b). Among these B-sites, the LDOS at the B1-site consistently shows the highest intensity, while the B3-site displays the weakest intensity across the energy range of interest. The spatial distribution of the LDOS corresponding to these electronic levels is shown in Fig.6.15c-f. Unlike the localised dot-like structures observed with the symmetric onsite potential, the LDOS maps for the distorted potential exhibit stripe-phase electronic structures. The intensities are no longer localised at the A-site but are distributed across the lattice, reflecting the breaking of the symmetry and the emergence of stripe phases in the electronic structure.

6.6.4 Insights and unanswered questions from tight-binding model

The tight-binding model, which focuses on the graphene sheet with superlattice potential modulation, qualitatively captures some spectroscopic features observed in the experiments. Using a symmetric potential, the model successfully reproduces the localised dot-like electronic structures. However, it fails to account for the delocalized electronic structure observed in the experiments. Introducing distortions to the on-site potential in the model transforms the localised structures into a stripe phase, which no longer remains localised at the A-site. This adjustment enables the model to replicate the delocalized electronic structure of the stripe phase.

Despite its ability to reproduce certain experimental features, the tight-binding model leaves several questions unanswered. First, experimental observations reveal the coexistence of localised electronic structures corresponding to the phase of (0,0,0) and delocalized stripe phases associated with (π,π,π) within the same sample. While the symmetric potential landscape in the model reproduces the localised states, the distorted potential is required to replicate the delocalized stripe phase. The coexistence of these phases remains unexplained within the current framework. Additionally, the origin of the distorted potential itself is unclear. One plausible hypothesis is that the formation of a $\sqrt{3}\times\sqrt{3}$ superlattice enhances the interaction between graphene and 1T-$NbSe_2$. This enhanced interaction may distort the CDW in 1T-$NbSe_2$, resulting in the observed delocalized stripe phase.

In conclusion of this chapter, we introduce a new method for constructing the superlattice in graphene by proximity to the 1T-$NbSe_2$. The localised electronic structure can be achieved in graphene. These localised electronic states can be further tuned by adjusting the twisted angle. Such tailored superlattice engineering can pave the way for exploring exotic quantum states and tunable electronic properties in van der Waals heterostructures. However, the coexistence of localised and stripe-like electronic structures remains an open question, calling for further theoretical and experimental exploration to unravel the mechanisms behind the observed symmetry breaking and potential distortions in the charge density wave of 1T-$NbSe_2$. These findings provide a foundation for advancing superlattice design and understanding

correlated quantum phenomena in two-dimensional systems

7 Investigating electronic property of CrSBr on 2H-$NbSe_2$

7.1 Introduction

7.1.1 2D magnets

According to the Mermin-Wagner theorem [157], ferromagnetic ordering is theoretically prohibited in 2D systems at finite temperatures. This theorem states that in spin-rotational invariant systems with short-range interactions, long-range magnetic order cannot be sustained below three dimensions due to thermal fluctuations. However, in 2017, experimental observations of ferromagnetic ordering in CrI_3 and $Cr_2Ge_2Te_6$ [158] down to the 2D limit demonstrated that magnetic anisotropy can stabilise long-range order in 2D systems [159]. The magnetic anisotropy breaks the continuous spin rotational symmetry, thereby circumventing the restriction imposed by the Mermin-Wagner theorem[160].

In monolayer CrI_3, each chromium cation carries a magnetic moment of $S = 3/2$, while the halide ligands (iodine anions) are non-magnetic. The magnetic interactions between chromium cations, separated by non-magnetic ligands, arise from the super-exchange interaction proposed by Anderson [161]. The stabilisation of the ferromagnetic order requires

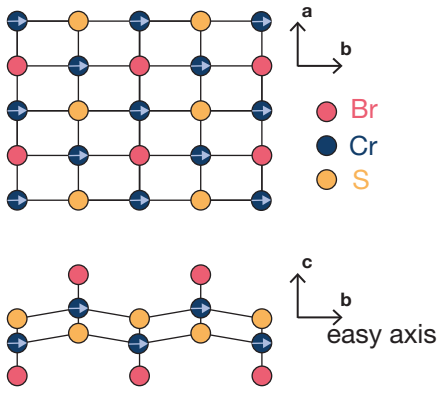

Figure 7.1: **Top view (ab-plane) and side view (bc-plane) of the lattice structures of a monolayer CrSBr.** The blue arrows show every Cr atom holding a spin along the b-direction.

magnetic anisotropy induced by spin-orbit coupling (SOC) from the halide ligands [162]. By substituting the iodine ligands with bromine or chlorine, the SOC strength can be reduced, leading to different magnetic ground states. CrI_3 with highest SOC exhibits a strong out-of-plane ferromagnetic order, consistent with the Ising model; $CrBr_3$ lies near the boundary between out-of-plane and in-plane ferromagnetic order, described well by a Heisenberg model; and $CrCl_3$ has the weakest SOC and exhibits in-plane magnetic order consistent with the so-called XY-model due to it has smallest SOC [163, 164]. This trend in magnetic ground state changes, as spin-orbit coupling provided by the ligands decreases, raises the question of whether the magnetic ground states in 2D magnets could be further tuned by stacking a monolayer 2D magnet on a substrate with strong SOC [165]. The SOC effect from the substrate could influence the 2D magnet order through proximity coupling, potentially modifying the spin texture in the 2D magnet and introducing more complex magnetic configurations [166].

$CrCl_3$ is our first interest to achieve this goal due to its weakest SOC provided from chromium ligands; however, the strong interlayer interaction prevents the exfoliation to a monolayer, and the $CrCl_3$ flakes are very difficult to apply vdW transfer by using graphite or other 2D flakes. These two drawbacks prevented us from assembling the $CrCl_3$- based heterostructures. Fortunately, another interesting 2D magnet is CrSBr, which is also a layered vdW 2D magnetic semiconductor with the FeOCl structure type of halogen halides [167]. Different from the chromium trihalide (CrX_3) in which the chromium cations form a hexagon lattice, CrSBr shows a rectangular lattice (Fig.7.1). The atomic arrangement will be discussed in section 7.2. Bulk CrSBr exhibits a Curie temperature of approximately 132 K [168], and at our measurement temperature of 1.4 K, the system is deep within the ferromagnetic phase. In monolayer CrSBr, the chromium cations are ferromagnetically coupled to their neighbours, forming an in-plane ferromagnetic order along the *b*-axis. Due to the weak SOC provided by the light sulfide and bromide ligands, CrSBr is expected to be highly sensitive to external SOC proximity effects introduced by the substrate. A typical substrate used for providing SOC in vdW heterostructures is 2H-$NbSe_2$ [169, 170]. Therefore, in this chapter, we focus on the heterostructure of monolayer CrSBr on the 2H-$NbSe_2$ bulk substrate to explore its electronic structures.

7.1.2 Heterostructure of ferromagnetic and superconductor

Interestingly, after the upgrade of the 1K pot (more details see chapter 3), our STM base temperature reaches 1.4 K. At this temperature, 2H-$NbSe_2$ shows superconducting behaviour at this temperature. Stacking CrSBr on top of 2H-$NbSe_2$ makes a hybrid system of ferromagnetism and superconductivity. Ferromagnetism and superconductivity are two fundamental concepts in modern solid-state physics. Ferromagnetic order requires spins to align in the same direction, while conventional superconductivity favours paired electrons with opposite spins, known as singlet Cooper pairs. When a ferromagnetic material comes into contact with a superconductor, these competing tendencies lead to exotic physical effects at their interface [171, 172]. On the one hand, the exchange field in the ferromagnet aligns electron spins parallel to each other, thereby suppressing singlet Cooper pairing. On the other hand,

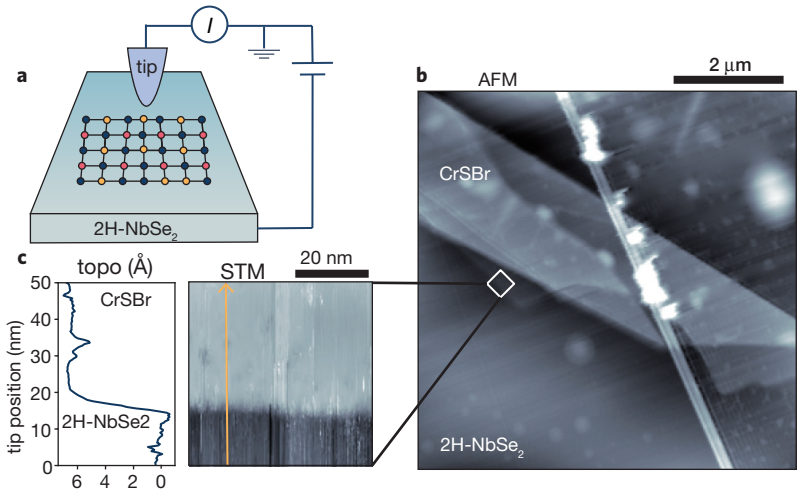

Figure 7.2: **Stacking CrSBr on 2H-$NbSe_2$. a,**Schematic of the heterostructure showing the monolayer CrSBr on bulk 2H-$NbSe_2$. **b,** constant force AFM topography of the sample (setpoint force: 6.5 nN). **c,** right panel: STM topography measured at the edge of CrSBr and $NbSe_2$ (V =1.5 V, I = 20 pA). Left panel: line cut along the edge shows the height of the monolayer of CrSBr on NbSe2 is 6 Å.

the superconductor proximity effect enables Cooper pairs to penetrate the ferromagnetic layer. However, the exchange field disrupts the singlet pairing typical of conventional superconductivity, causing superconducting correlations in the ferromagnet to decay rapidly, much faster than at a normal-metal-superconductor interface [173].

Interestingly, under certain conditions, the heterostructure of a ferromagnet on a superconductor can generate triplet Cooper pairs with parallel-aligned spins [174, 175]. This triplet pairing can penetrate the ferromagnet over longer distances, unlike conventional singlet pairs, which are rapidly suppressed. Additionally, the heterostructure of ferromagnetic on superconductor is proved to achieve topological superconductivity, a promising platform for realizing Majorana zero modes, which hold significant potential for quantum computing applications [176].

7.2 Stacking CrSBr on 2H-$NbSe_2$

Due to its semiconducting nature with a band gap of 1.2 V, CrSBr have to be thinned down to a monolayer or bilayer to enable tunnelling in an STM for the investigation of the low-energy electronic structure at the interface between CrSBr and $NbSe_2$. For this purpose, we prepared a heterostructure consisting of atomically thin CrSBr atop bulk 2H-$NbSe_2$ for the STM measurements (Fig.7.2a) in the glovebox filled with Argon and transferred to the STM by a vacuum suitcase. The method of the sample preparation is detailed in the chapter 4. The AFM topography shown in Fig.7.2b indicates that the sample is clean and that there is a little residue at the edge of the flakes. The step height of CrSBr on $NbSe_2$, measured by STM, is approximately 6 Å, which matches the expected thickness of monolayer CrSBr [167].

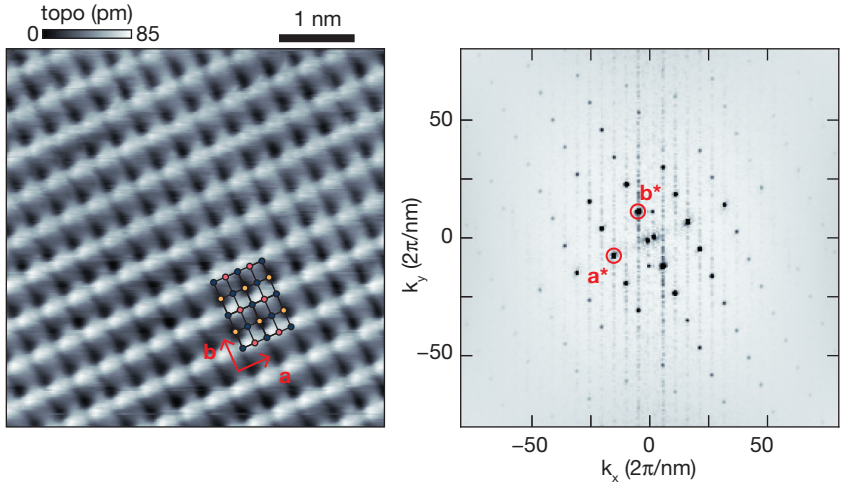

Figure 7.3: **Structure property of CrSBr. a,** STM topographies of CrSBr on $NbSe_2$ resolving the atomic resolution (V = 0.6 V, I =200 pA). **b,** corresponding FFT image of CrSBr on $NbSe_2$.

The atomic resolved CrSBr on $NbSe_2$ is shown in Fig.7.3a. The topograph shows a rectangular lattice assigned to the CrSBr lattice. The absence of any moiré pattern could stem from the weak hybridisation between CrSBr and $NbSe_2$. A single layer of CrSBr sheet consists of four atomic sub-layers: the top and bottom capping layers are anionic bromide layers, while two chromium sulfide (Cr-S) layers are sandwiched between them (Fig.7.2). The topmost bromide anion layer manifests as bright spots in the topography, representing sites of high apparent height. Once the bromide positions are identified, the atomic arrangement can be mapped according to the lattice structure shown in Fig.7.1. The bridge positions between two bromine anions correspond to chromium cations, while along the b-axis, the darker spots between the chromium cations correspond to sulfide anions. This arrangement is overlapped on the topography in Fig.7.3a. The FFT pattern shown in Fig.7.3b confirms that the rectangular lattice of CrSBr lattice with the lattice constants of $|\mathbf{a}| = 0.350\,\text{nm}$ and $|\mathbf{b}| = 0.476\,\text{nm}$.

7.3 Visualization of quasi-1D electronic structure of CrSBr

The STS spectroscopy taken at the CrSBr exhibits semiconducting behaviour (Fig.7.4), where we see a hard gap from approximately −1.4 V to 0.2 V. Above the Fermi level, a hump-like feature occurs in the range from 0.2 V to 0.5 V and the conductivity increases dramatically starting at 0.95 V and maximises at 1.2 V. DFT+ U calculation pointed out that the band structure of the monolayer CrSBr is very similar to the bulk CrSBr but with a slightly larger band gap due to the dimensional reduction[179]. The statement can be proved by comparing our measurement with previous STS taken on bulk CrSBr at 137 K [168], which has shown a similar feature consistent with ours, where the finite conductivity was observed at approximately the same level. This allows us to assign the bottom edge of the conduction band (CB) of CrSBr close to the Fermi level.

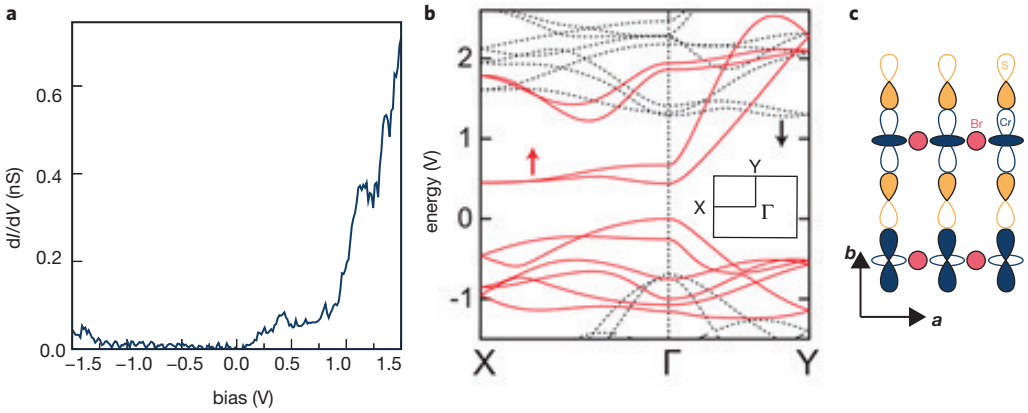

Figure 7.4: **Electronic structure of CrSBr. a,** Large scale STS spectroscopy on CrSBr (V = 1.5 V, I = 300 pA). **b,** The theoretically calculated band structure of monolayer CrSBr. The red solid and black dashed lines represent bands formed by spin-up and spin-down states, respectively (Adapted from ref.[177]). **c,** Schematic illustration of the orbital character of the conduction band. For clarity, only one Cr site per unit cell is shown (Adapted from ref.[178])

The hallmark of the CrSBr is its quasi-one-dimensional electronic structure [177, 180]. This is characterised by two spin-polarised CB, which are splitting at Γ point. These bands exhibit anisotropic dispersion, remaining flat along the $\Gamma \rightarrow X$ direction, which corresponds to the **a**-axis in real space while being highly dispersive along $\Gamma \rightarrow Y$ direction corresponding to the **b**-axis in real space (Fig.7.4b).

Theoretical studies [180] attribute this strong anisotropy to the hybridisation of chromium-sulfide chains that run along the **b**-axis, while bromine orbitals play a minor role (Fig.7.4c). This hybridisation predominantly contributes to the formation of the two CBs above the Fermi level. As a result, the bands exhibit high dispersion along the **a**-axis, but flat dispersion along the **b**-axis. The orbital composition of these bands further underscores this behaviour: for the lower CB: 64% Cr,32% S, and 4% Br and for the upper CB: 86%Cr, 9% S, and 5% Br. Consequently, a reasonable expectation is that the lower CB is expected to exhibit a chain-like spatial distribution along **a**-axis. In contrast, the upper CB should be more localised around chromium sites. Despite these theoretical predictions, experimental confirmation at the atomic scale remains absent. Until the preparation of this thesis in the second half of 2024, all existing measurements of these anisotropy bands have been limited to macroscopic transport properties. Angle-resolved photoemission spectroscopy hinted to a quasi-one-dimensional electronic structure at the Fermi level, but could not yet resolve these two flat dispersion bands along $\Gamma \rightarrow X$ direction [181]. Direct visualisation of the predicted flat dispersion and its spatial characteristics at the atomic level has yet to be achieved.

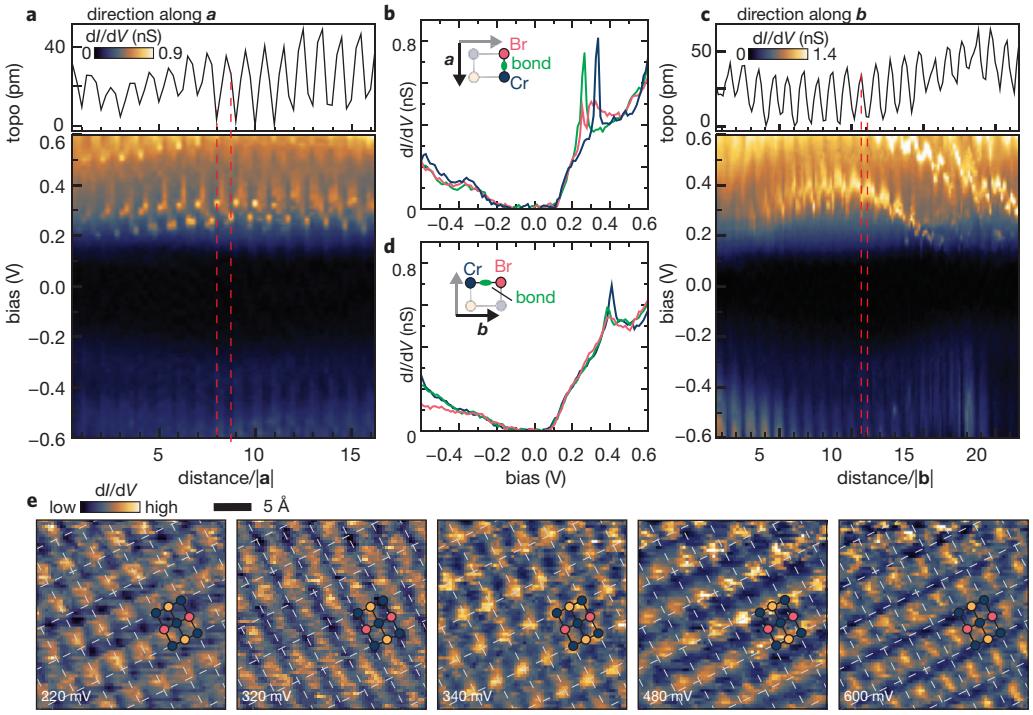

Figure 7.5: **Quasi one-dimensional electronic structure. a,** Constant current dI/dV spectroscopy linescan and the corresponding topography profile recording along -Cr-Br-Cr. The distance is normalized by the lattice constant of |**a**| = 3.64 Å(V = 0.6 V, I = 200 pA). **b,** dI/dV spectra recorded at the Br position, Cr position and bond between Br and Cr along **a** direction. **c,** Constant current dI/dV spectroscopy linescan and the corresponding topography profile recorded along Cr-Br-Cr. The distance is normalized by the lattice constant of |**b**| = 4.90 Å(V = 0.6 V, I = 200 pA). **d,** dI/dV spectra recorded at the Cr position, Br position and the bond between Br and Cr along the **b** direction. **e,** Constant height dI/dV maps recorded at the given biases.

7.3.1 Visualzation of the quasi-one-dimensional electronic structure

Figure 7.5a shows the dI/dV spectra recorded along the -Cr-Br-Cr chain in the **a**-axis. At each pixel, the stabilisation conditions, including the tunnelling current and the bias, were kept constant. Consequently, the relative tip positions (topography) required for stabilisation at each spectroscopy were recorded, revealing a zig-zag feature. Based on the analysis of the lattice structure in section 7.2, the peak in the topography profile corresponds to the Br anion position, while the valleys align with Cr positions. The dI/dV spectra exhibit a strong atomic corrugation. At the topography peak position (Br-position), the spectra show a hard gap between −100 mV and 100 mV, with a hump-like feature observed between 200 mV and 400 mV. Notably, two sharp peaks at 220 mV and 320 mV emerge (Fig.7.5b). Both peaks are highly localised along **a**-axis in real space: the lower peak at 220 mV sits at the bond position between the Cr and Br, while the upper sharp peak at 320 mV is located at the Cr site. Along the a-axis, these two sharp peaks appear with the periodicity of the lattice constant |**a**|.

The dI/dV spectra recorded along the Cr-Br-Cr chain of the **b**-axis reveal two features (Fig.7.5c). First, a single sharp peak is observed, whose intensity gradually increases as the tip moves from the Br-site (topographic peak) to the Cr-site (topographic valley), reaching a maximum at the Cr-site (Fig.7.5d). Second, the energy positions of this peak exhibit a modulation with a relatively long wavelength. This modulation will be discussed later in Subsection 7.3.4.

To further investigate the LDOS distribution of these two flat CBs, which is directly related to the spatial distribution of differential conductivity, we performed constant-height dI/dV maps with an open feedback loop (Fig.7.5e). Grid lines overlaid on the maps indicate the bright spots observed at 340 mV, which are identified as the Cr sites. At the 220 mV, the LDOS is spatially localised at the bond states between Cr and Br along the **b**-axis, while at 320 mV, a strip pattern is observed, which are aligned with the S-Cr-S chains. This observation of the strip pattern aligns well with the theoretically predicted quasi-one-dimensional CB as shown in Fig.7.4c. At higher biases, the LDOS distribution evolves further: at 480 mV, the LDOS becomes localized at the S-sites and further at 600 mV; the Cr cations connected to S anions along **b**-axis shows the pronounced LDOS with a dumbbell shape.

7.3.2 Magnetic dependent atomic corrugation

Next, we examined the electronic structure under an out-of-plane magnetic field of 1 T applied along the hard **c**-axis. The spatially resolved dI/dV along the **a**-axis in Fig.7.6a, reveals significant differences compared to the zero-field measurements. Notably, the sharp peak detected at the Cr site without a magnetic field is absent under the magnetic field (Fig.7.6b). Instead, at the bond site between Cr and Br, a doublet-peak feature emerges, with the peaks separated by 55 mV.

Along the **b**-axis, the spatially resolved dI/dV spectra under the magnetic field reveal strong atomic corrugation at 360 mV (highlighted by green dotted box) and an oscillation above 500 mV (highlighted by red dotted box), both periodic with the lattice constant |**b**| (Fig.7.6c). The dI/dV spectra recorded at the Br site, Cr site, and the bond position along the **b**-axis all exhibit a sharp peak, with the intensity maximised at the bond position (Fig.7.6d). Compared to the zero-field spectra (the dotted curve), the peak intensity becomes stronger under the magnetic field, while the energy position remains unchanged.

To visualise how the LDOS distribution is modified by the magnetic field, we conducted constant-height dI/dV mapping at various biases (Fig.7.6e). Compared to the zero-field maps (Fig.7.5e), the LDOS at 220 mV and 260 mV forms a zig-zag strip pattern, running diagonally between Cr atoms at opposite corners of the unit cell. This zig-zag pattern breaks the mirror symmetry along the **b**-axis. As the bias increases to 320 mV, the LDOS evolves into elongated dot-like structures along the Cr-S-Cr chains, recovering the mirror symmetry.

At 400 mV, the LDOS is localised at Cr cations along the Cr-Br-Cr chains. At 420 mV, the pattern reverses, showing higher LDOS at Cr-sites along the Cr-S-Cr chains. By 460 mV, the pattern shifts back to the configuration observed at 400 mV. At 600 mV, the LDOS becomes

dominated by a dots-like pattern corresponding to the Br anions.

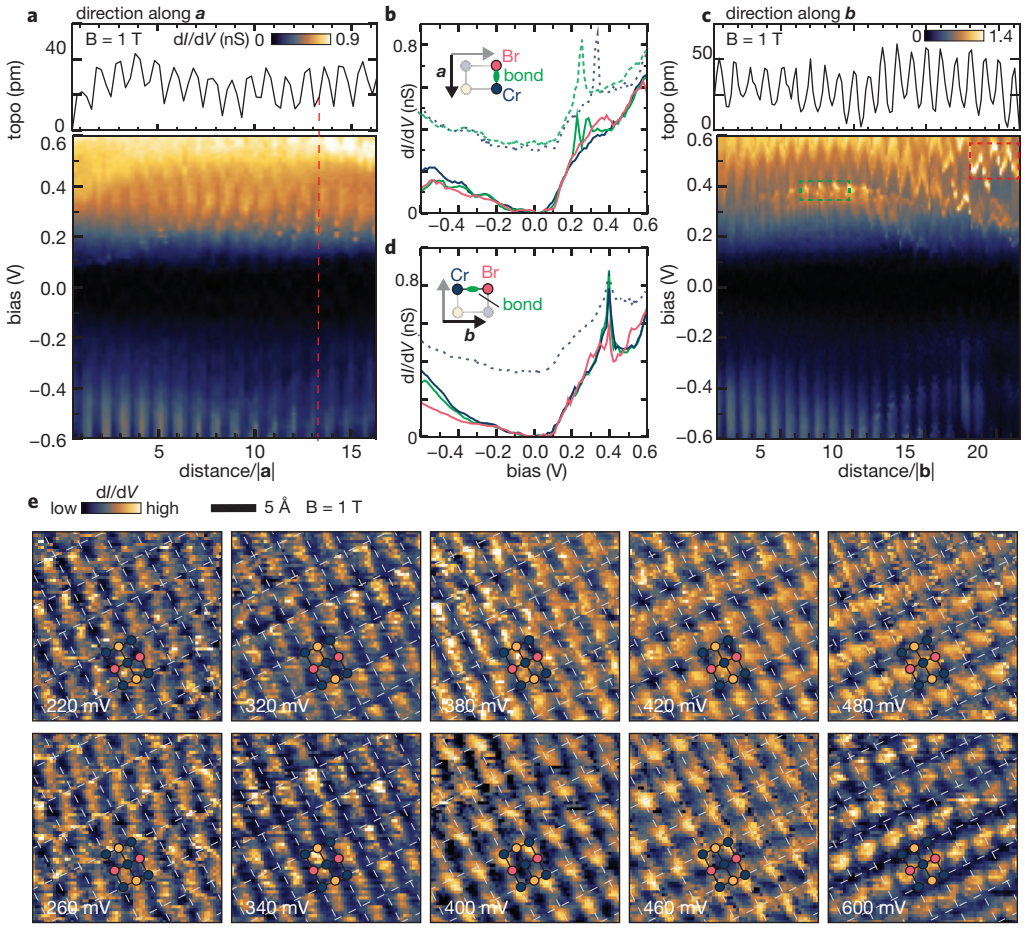

Figure 7.6: **Electronic structure with the out-of plane magnetic field of** 1 T**. a,** Constant current dI/dV spectroscopy linescan and the corresponding topography profile recorded along Cr-Br-Cr. The distance is normalized by the lattice constant of $|\mathbf{a}| = 3.64\,\text{Å}$($V = 0.6\,\text{V}$, $I = 200\,\text{pA}$). **b** dI/dV spectra recorded at the valley position, peak position and bridge position of the topography profile along the **a** direction. The dotted lines show the spectra in Fig.7.5b with vertical off shift and its intensity is scaled by ×0.67. **c,** Constant current dI/dV spectroscopy linescan and the corresponding topography profile recorded along Cr-S-Cr. The distance is normalized to the lattice constant of $|\mathbf{b}| = 4.90\,\text{Å}$($V = 0.6\,\text{V}$, $I = 200\,\text{pA}$). **d** dI/dV spectra recorded at the Cr and S positions. The dotted line shows the spectrum in Fig.7.5c with vertical off-shift and its intensity is scaled by ×0.67. **e,** Constant height dI/dV maps recorded at given biases.

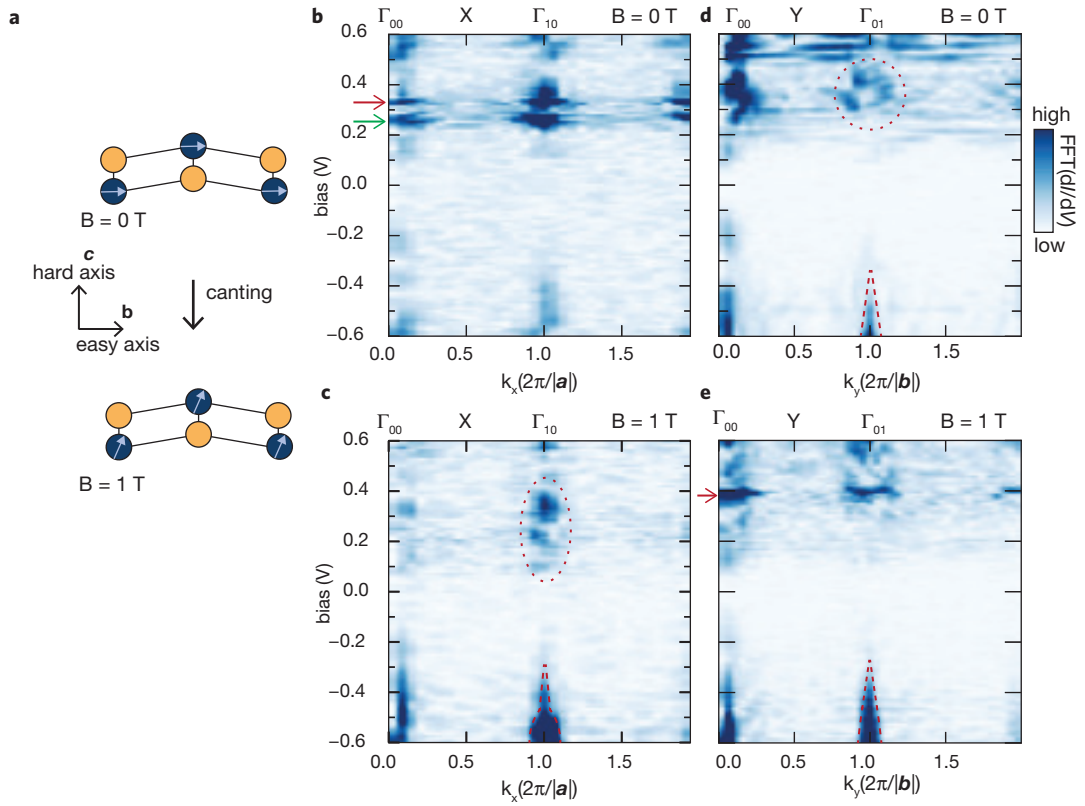

Figure 7.7: **Reconstructed band structure. a,** Schematic representation of canting the spins in CrSBr by applying an out-of-plane magnetic field along its hard axis. Bromine anions are omitted for clarity. **b,** Fourier transform amplitude of the spatially resolved dI/dV along **a**-axis in Fig.7.5a. **c,** Fourier transform amplitude of the spatially resolved dI/dV along **a**-axis in Fig.7.6a. **d,**Fourier transform amplitude of the spatially resolved dI/dV along **b**-axis in Fig.7.5c. **e,** Fourier transform amplitude of the spatially resolved dI/dV along **b**-axis in Fig.7.6c ($|\mathbf{a}| = 3.64$ Å, $|\mathbf{b}| = 4.90$ Å).

7.3.3 Reconstruct the band structure

After visualizing the changes in the electronic structure of CrSBr on 2H-$NbSe_2$ under an out-of-plane magnetic field applied along the hard axis, we now explore the relationship between spin canting and its influence on the electronic band structure of CrSBr. At 1.4 K, the saturation magnetic field of CrSBr along the **c**-axis is approximately 2 T [168]. Applying a magnetic field of $B = 1$ T induces spin canting, tilting the spins from their easy **b**-axis toward alignment along the **c**-axis. However, under this field strength, the spins do not fully align with the **c**-axis, leading to a partially canted spin configuration (Fig.7.7a).

The band dispersion of CrSBr was reconstructed by applying a Fourier transformation to the spatially resolved dI/dV spectra. The intensity of the Fourier-transformed spectra reflects the dispersion of scattering wave vectors between electronic bands. Along the $\Gamma \rightarrow X$ direction, two flat dispersion bands were identified: a lower branch at 260 mV (marked by

green arrow) and an upper branch (marked by red arrow) at 320 mV (Fig.7.7b). These flat bands are consistent with the band structure predicted by DFT calculations (Fig.7.4b).

When an out-of-plane magnetic field of 1 T was applied, the flat bands were no longer observed. Instead, two dot-like features, highlighted by a red dotted circle, appeared between 300 mV and 400 mV at the Γ-point (Fig.7.7c). This observation indicates that spin canting disrupted the flat dispersion of the CB. Additionally, a feature with strong intensity, outlined by a red dotted line, emerged below −300 mV at the Γ-point. This feature is likely associated with the dispersion of the VB, which was also affected by the spin canting induced by the magnetic field.

Along the $\Gamma \rightarrow Y$ direction, in the absence of a magnetic field, a hole-like feature centred at 400 mV was observed at the Γ-point (highlighted by a red dotted circle), along with a linear dispersion feature below −400 mV (outlined by a red dotted line) in Fig.7.7d. When an out-of-plane magnetic field was applied, the hole-like feature evolved into a flat feature with strong intensity, marked by a red arrow, at approximately 400 mV. Simultaneously, the linear-dispersion feature below −400 mV exhibited an increase in intensity (Fig.7.7e).

The comparison of band dispersion along $\Gamma \rightarrow X$ (Fig.7.7a) and $\Gamma \rightarrow Y$ (Fig.7.7b) reveals significant anisotropy in CrSBr. The two conduction bands (CBs) with flat dispersion at 260 mV and 320 mV are consistent with DFT calculations (Fig.7.4b) and prior transport measurements [177, 180]. However, theoretical calculations on the impact of spin canting on the band structure of CrSBr remain absent during the preparation of this thesis. The observation of a flat feature near 400 mV along the $\Gamma \rightarrow Y$ direction (Fig.7.7e) and the corresponding localized $\mathrm{d}I/\mathrm{d}V$ maps at the same energy (Fig.7.6e) suggests the emergence of a flat band at 400 mV under an applied magnetic field of 1 T.

A potential explanation is that spin canting induces the spin-polarised CBs along the **b**-axis to hybridise with bands of opposite spin polarisation at higher energy levels. This hybridisation arises from the reorientation of spins caused by the applied magnetic field along the **c**-axis, which disrupts the original spin alignment and introduces new coupling pathways between the spin-polarised bands [182]. Consequently, the conduction bands shift to higher energy levels, approaching the bands with opposite spin polarisation, and their dispersion relations are modified. This process leads to the reconstruction of the electronic structure, giving rise to new electronic features.

7.3.4 Magnetic-field dependent long wavelength modulation in CrSBr

Furthermore, spin canting introduces a competition between the exchange interaction and the external magnetic field. The exchange interaction favours spin alignment along the **b**-axis, while the external magnetic field aligns spins along the **c**-axis. This interplay may result in the emergence of complex spin textures.

To probe these effects, constant-height quasi-particle interference measurements were performed by applying a Fourier transform to the $\mathrm{d}I/\mathrm{d}V$ maps over a $15 \times 15\,\mathrm{nm}^2$ area (Fig.7.8).

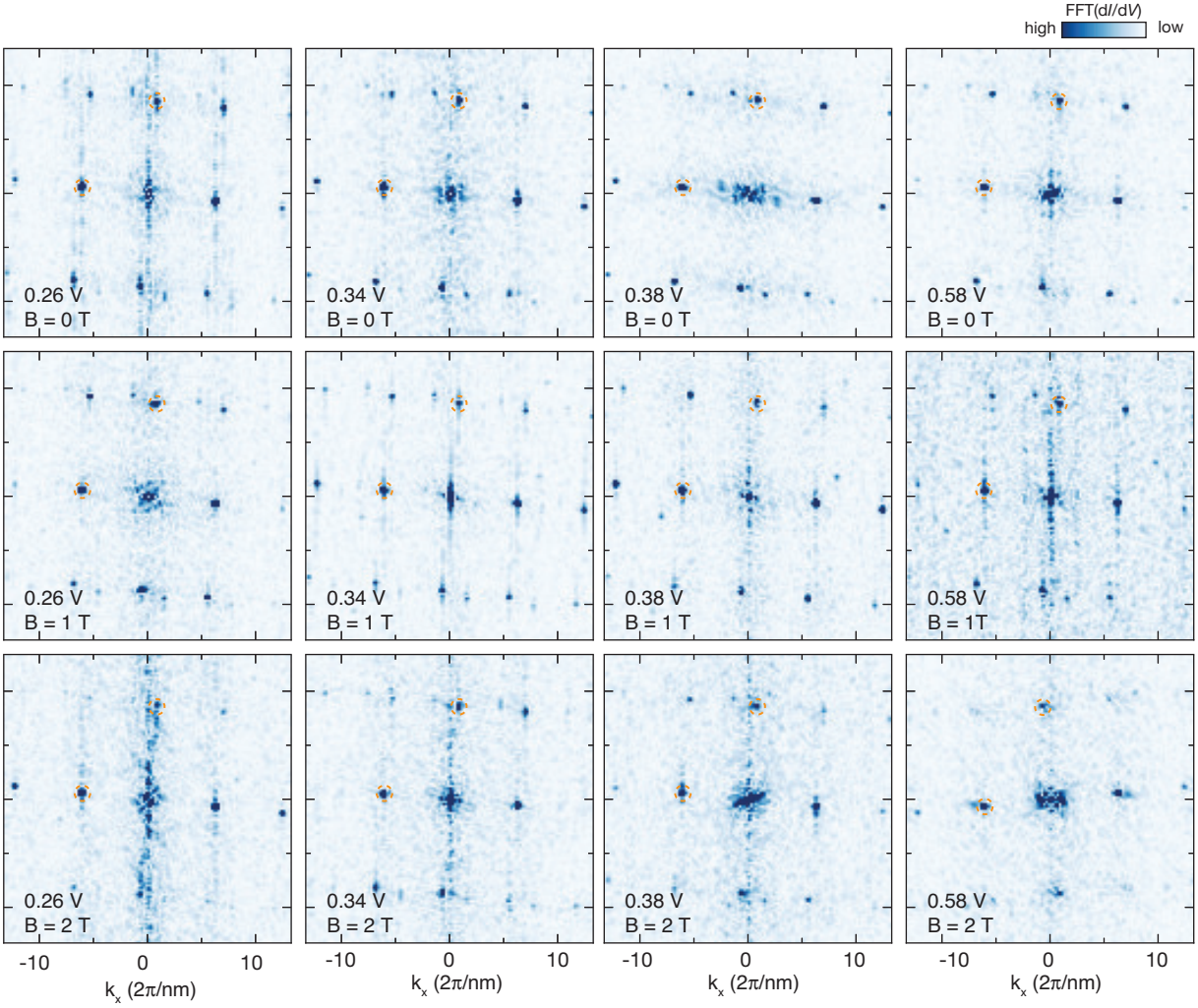

Figure 7.8: **Magnetic dependent constant height quasi-particle interference.** The dotted dashed circles indicate the Bragg peaks of the CrSBr lattice.

The orange dotted circles in Fig.7.8 indicate the Bragg peaks of CrSBr. Around the Γ-point, standing wave-like features with relatively long wavelengths are observed. These patterns are bias-dependent and exhibit changes under an applied magnetic field.

The origin of these features remains unclear. Due to their magnetic dependence, they may correspond to spin waves, such as magnons. However, quasi-particle interference from magnons typically occurs near the Fermi level [183], whereas the bias range probed here is significantly higher. This suggests that these features might arise from interactions between magnons and other quasi-particles. In CrSBr, magnon-exciton coupling has been reported [184], as well as magnon-phonon coupling [185]. However, the current measurements lack sufficient resolution and evidence to definitively confirm the coupling mechanisms or the exact nature of the observed spin-wave-like structures. For resolving the magnon structure, further spin-polarised STM measurement is necessary, as well as the theoretical calculation.

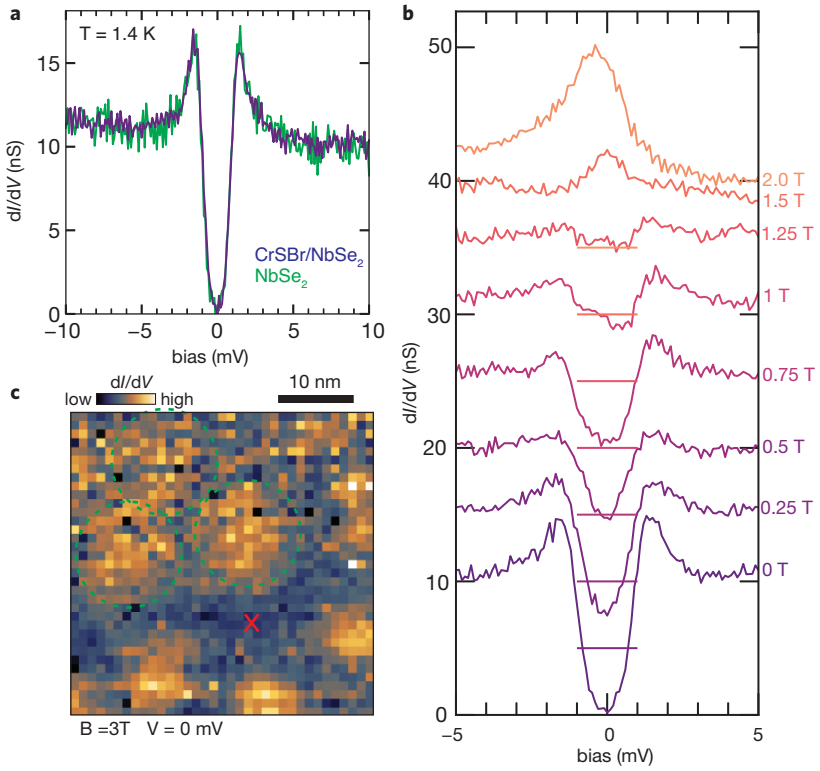

Figure 7.9: **Probing superconductivity on CrSBr/2H-NbSe$_2$ interface.** **a**,dI/dV spectra taken on 2H-NbSe$_2$ and CrSBr on NbSe$_2$. **b,** out-of-plane magnetic dependent magnetic field dependent measurement on CrSBr on 2H-NbSe$_2$ dI/dV. For clarity, each spectrum is vertically shifted by 5 nS, and the horizontal lines with the same colour show the baselines for the corresponding spectra (I = 100 pA, V = 10 mV, V_{mod} = 0.1 mV). **c,** Constant current dI/dV map slicing at 0 mV under 3 T. The black dotted lines circle the vortex profile.

7.4 Probing the superconductivity

In the final part of this chapter, I presented the electronic structure of CrSBr on 2H-NbSe$_2$ near the Fermi surface. Figure 7.9a compares the dI/dV spectrum recorded on CrSBr/2H-NbSe$_2$ with that of bulk 2H-NbSe$_2$, taken 44 nm apart. Both spectra exhibit identical features, and no in-gap states were observed in the region of CrSBr on 2H-NbSe$_2$. Upon applying an out-of-plane magnetic field, the superconducting gap shrank, and at 1.5 T, a zero-bias peak emerged, signalling the presence of an Abrikosov Vortex state(Fig.7.9b). The spatial distribution of vortices was subsequently mapped (Fig.7.9c)

This measurement could be attributed to the weak coupling between the local magnetic momentum holder by the Cr cations and the superconductivity in 2H-NbSe$_2$. As a result, CrSBr is insulating and likely acts as a vacuum barrier for the tunnelling, the observed superconducting gap and vortex state mainly contributed to the 2H-NbSe$_2$ underneath. This observation is consistent with the measurement of CrBr$_3$ on 2H-NbSe$_2$ [186].

Next, we aimed to investigate the magnetic dependence of superconductivity. After

identifying the vortex positions at a magnetic field of 3 T (Fig.7.9c), we positioned the tip in a region without vortices marked by a red cross and measured the dI/dV spectra while gradually ramping down the magnetic field. Unfortunately, during the process, the superconducting coil was quenched, resulting in damage to both the sample and the machine. As a result, we were unable to proceed with further measurements. Thus, the data presented in Fig.7.9 concludes this PhD thesis, although with low spatial resolution.

7.5 Conclusion

This chapter has delved into the electronic properties and interactions of CrSBr on 2H-$NbSe_2$, exploring its quasi-one-dimensional electronic structure and anisotropic conduction bands. CrSBr exhibits intriguing electronic and magnetic phenomena, including localised states, magnetic field-dependent modulations in the LDOS, and flat dispersion in specific directions. By stacking CrSBr on a superconducting 2H-$NbSe_2$ substrate, the study provides insight into the interplay between 2D magnetism and superconductivity.

Key findings include the identification of flat conduction bands through STS and their reconstruction under the influence of an out-of-plane magnetic field. Spin canting induced by the magnetic field disrupts the original band structure, introducing new coupling pathways and revealing magnetic field-dependent features. Additionally, long-wavelength patterns observed in quasi-particle interference maps hint at the presence of spin excitations, potentially coupled with other quasi-particles, such as magnons or phonons.

The study also probed the superconducting properties of the CrSBr/2H-$NbSe_2$ heterostructure, revealing vortex states in 2H-$NbSe_2$ and confirming weak coupling between CrSBr and the superconducting substrate. While the results did not demonstrate strong coupling effects or proximity-induced superconductivity in CrSBr, they highlight the potential of this system as a platform for exploring magnetic and electronic interactions in van der Waals heterostructures.

8 Conclusions and outlook

8.1 Conclusion

This thesis has focused on exploring the electronic structures and interactions in $NbSe_2$-based 2D vdW heterostructures using STM and STS. First, a new method known as suspended dry pick-up and flip-over assembly technique has been developed, which ensures a clean surface by avoiding polymer contact. This method, performed entirely in an argon-filled glovebox, allowed us to prepare high-quality samples for STM, a technique that is extremely surface-sensitive and ideal for probing atomic-scale quantum phenomena in heterostructures.

Using this technique, we first investigated the proximity-induced doped Mott physics in heterostructures of 1T-$NbSe_2$ and 2H-$NbSe_2$. By locally inducing a phase transition from 2H-$NbSe_2$ to 1T-$NbSe_2$ via voltage pulses, we created heterostructures for studying the interface between these two phases. Our findings revealed an ordered lattice structure of 1T-$NbSe_2$ accompanied by spatially inhomogeneous electronic properties. Notably, strong Kondo resonance peaks were observed in certain SoD clusters, while neighbouring clusters exhibited gap-like insulating behaviour. This electronic inhomogeneity was attributed to the competing effects of Kondo coupling and doping, mediated by the interplay between the 3×3 CDW in 2H-$NbSe_2$ and the $\sqrt{13} \times \sqrt{13}$ CDW in 1T-$NbSe_2$.

Building upon the 2H-to-1T phase transition in $NbSe_2$, we explored graphene interfaced with 1T-$NbSe_2$ on 2H-$NbSe_2$. By controlling the twist angle between the graphene and $NbSe_2$, we achieved near-commensurate superlattice structures: a 2×2 superlattice at 9° and a $\sqrt{3} \times \sqrt{3}$ superlattice at 27° in respect to the CDW of the 1T-$NbSe_2$ layer. In the 2×2 case, C_3 rotational symmetry was preserved, while in the $\sqrt{3} \times \sqrt{3}$ structure, we observed symmetry breaking and the emergence of stripe phases. This observed symmetry-breaking is still an open question. We have proposed some theoretical models, which can capture some of the observed spectroscopic features.

Finally, we studied the heterostructure of CrSBr on 2H-$NbSe_2$ $_2$, combining the quasi-one-dimensional ferromagnetism of CrSBr with the superconducting and charge-density-wave properties of 2H-$NbSe_2$. Our experiments revealed that CrSBr retains its intrinsic insulating properties with no significant coupling to the $NbSe_2$ substrate. STS visualized flat conduction

bands in CrSBr as predicted by DFT calculations, which were further modified by applying out-of-plane magnetic fields. The superconducting properties of $NbSe_2$ remained unaffected, as evidenced by the intact superconducting gap and vortex states.

8.1.1 Broader significance

Beyond the specific systems studied, this thesis contributes to several broader research directions. While twisted bilayer graphene has dominated the field of moiré physics, this work demonstrates that combining moiré periodicity with proximity effects from correlated materials (1T-$NbSe_2$) opens new avenues for engineering flat bands and symmetry-broken phases. The observed rotational symmetry breaking at energies far from the Fermi level suggests mechanisms distinct from conventional correlation-driven transitions.

The CrSBr/2H-$NbSe_2$ system, despite showing weak coupling, establishes a platform for studying intrinsic properties of atomically thin magnets using superconducting substrates as spectroscopic probes. The demonstrated ability to tunnel through insulating magnetic layers to image vortex states opens possibilities for studying Andreev processes and spin-polarised transport in Ferromagnetic/Superconductor (F/S) junctions.

The suspended dry pick-up and flip-over assembly technique addresses a critical bottleneck in vdW heterostructure fabrication for UHV surface-sensitive science. By avoiding polymer contamination, this method enables studies of surface-sensitive phenomena (Kondo physics, CDWs, magnetic order) that would be impossible with conventional transfer techniques.

8.2 Outlook

Looking forward, the weak coupling between CrSBr on 2H-$NbSe_2$ provides a platform to study the intrinsic magnetic order in atomic thin CrSBr flakes by the local probe technique. STM, coupled with spin sensors, for example, Nickelocene, can shed further light on visualising the spin texture of the magnetic order in CrSBr.

8.2.1 Investigate the ferromagnetic/superconductor coupling

As discussed in chapter 7, CrSBr exhibits ferromagnetic intralayer coupling with an easy axis along the b-axis (Fig.8.1a). However, the antiferromagnetic interlayer exchange interactions, characterised by coupling parameters J_{Z1} and J_{Z2}, lead to an antiferromagnetic ordering in untwisted bilayer CrSBr (Fig.8.1b).

A recent transport measurement on twisted bilayer CrSBr revealed a 700 % tunnelling magnetoresistance (TMR) ratio between antiferromagnetic and ferromagnetic configurations at zero magnetic fields [187]. This giant TMR offers an opportunity for STM to map the spatial distribution of conductivity, enabling the direct identification of interlayer magnetic order without the need for spin sensors.

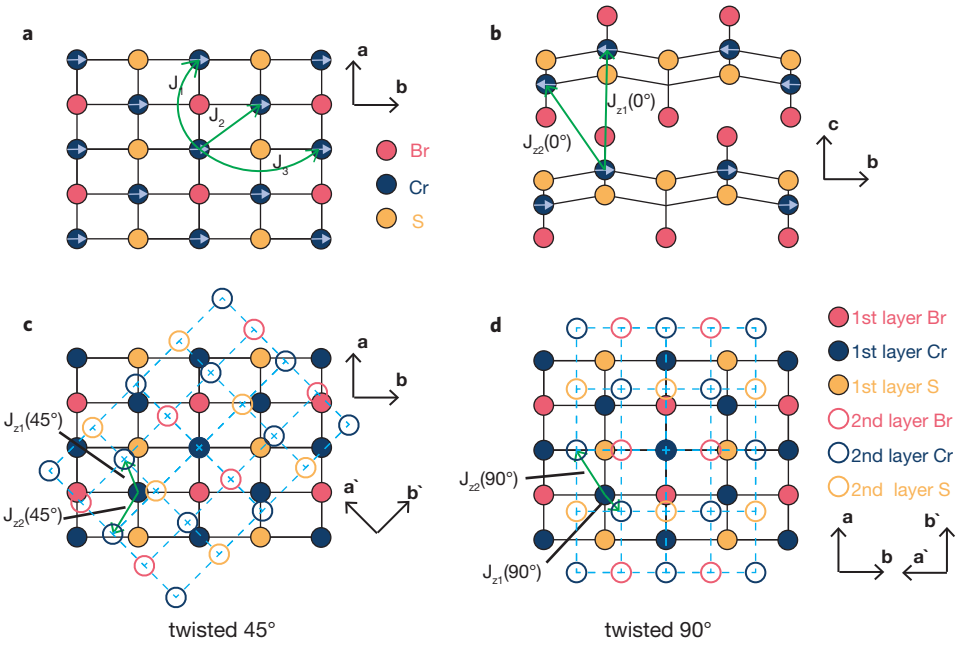

Figure 8.1: **Schematic illustration of the magnetic exchange coupling in (twisted) bilayer CrSBr. a,** Top view shows the intralayer exchange coupling between neighbouring Cr cations within a single layer of CrSBr **b,** Side view shows the interlayer exchange coupling components, J_{Z1} and J_{Z2}, for untwisted bilayer CrSBr. **c.** Top view shows the interlayer exchange coupling in bilayer CrSBr with a 45° twist. **d.** Top view shows the interlayer exchange coupling of CrSBr in with a 90° twist.

In detail, the interlayer coupling strengths J_{Z1} and J_{Z2} depend on the distances between Cr cations in adjacent layers. By introducing a twist between two CrSBr layers, these distances are periodically modulated (Fig.8.1c and d). This modulation is anticipated to manifest as a periodic conductivity landscape following the moiré periodicity, distinguishing regions of ferromagnetic and antiferromagnetic interlayer order. Such measurements will not only provide a microscopic understanding of the mechanisms behind the giant TMR effect but also highlight the potential of twisted bilayer CrSBr structures for applications in magnetic information storage, where the tunable magnetic order could serve as a robust platform for data encoding and retrieval.

8.2.2 Proximity induces external spin-orbital coupling to CrSBr

Theoreticians have predicted that a 2D lattice formed by magnetic adatoms on the surface of a superconductor with strong Rashba SOC could host a 2D topological chiral p-wave superconductor with 1D dispersive Majorana edge modes [188]. However, experimentally, this condition requires a delicate tuning of the exchange coupling, superconducting, and spin-orbital coupling of the heterostructures.

Currently, both experimental and theoretical understanding of the CrSBr/2H-$NbSe_2$ $_2$

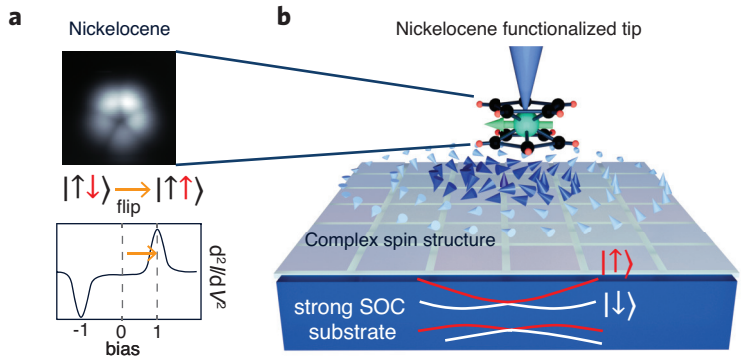

Figure 8.2: **Spin-resolved STM investigation of CrSBr based heterostructure. a,** STM image of a single Nickelocene molecule (top). Spin-flip excitation in the Nickelocene molecule as the principle of a spin sensor (bottom). **b,** The spin-resolved measurement will be performed using a nickelocene-functionalized STM tip.

heterostructure remain in preliminary stages. Chapter 7 demonstrated that direct contact between CrSBr and 2H-$NbSe_2$ results in weak coupling, with CrSBr retaining its intrinsic properties. However, this does not preclude more subtle SOC-induced modifications to the spin texture that are below the detection threshold of conventional STM.

Rashba-type SOC from the substrate could induce several effects in CrSBr:

1. **Spin canting:** Substrate SOC may induce out-of-plane spin components, breaking the purely in-plane magnetic order. This would manifest as modified magnetic anisotropy, detectable through field-dependent measurements.
2. **Dzyaloshinskii-Moriya interaction (DMI):** Interfacial SOC can induce DMI, favoring non-collinear spin textures. In CrSBr's quasi-1D structure, this could stabilize spin spirals or domain walls with characteristic wavelengths.
3. **Modified exchange coupling:** SOC-mediated superexchange could alter J_{Z1} and J_{Z2}, shifting the FM-AFM balance in bilayer CrSBr.

To observe this proximity-induced SOC effect on the spin texture of CrSBr, two key requirements must be met: a clean heterostructure sample and a spin-sensitive STM tip. The clean heterostructure can be achieved using the suspended dry pick-up and flip-over assembly technique detailed in chapter 4. For spin sensitivity, a nickelocene-functionalized STM tip is proposed (Fig.8.2), as it provides a high resolution for detecting spin textures in the zero magnetic field [189].

I propose a heterostructure design (Fig.8.2) where CrSBr is placed on a substrate with strong SOC. By utilising the Nickelocene-functionalized tip, it will be possible to resolve the complex spin texture in the CrSBr sheet, which is induced by the proximity-induced SOC. This comparative study offers a pathway to deeper insights into the interplay between SOC and magnetic properties in such heterostructures. Moreover, it represents a step toward engineering topological superconductors within 2D vdW heterostructures that combine 2D

magnets and superconductors.

A An appendix

A.1 Moiré pattern with uniaxial heterostrain

The approach to evaluate heterostrain in 2D heterostructures is based on the methods outlined in previous studies [147, 154], which have been successfully applied to twisted bilayer and twisted double bilayer graphene systems. These methods were originally developed for systems where both layers share the same lattice constant. Here, we extend this methodology to analyze graphene/$NbSe_2$ heterostructures, where the two layers have different lattice constants.

We begin by considering the unstrained lattice structures of both graphene and $NbSe_2$, which are characterized by hexagonal lattices with C_3 point group symmetry. The reciprocal lattice vectors for graphene can be expressed as:

$$\mathbf{k_{11}} = |k_1| \begin{pmatrix} 1 \\ 0 \end{pmatrix}, \mathbf{k_{12}} = R(60^\circ) \cdot \mathbf{k_{11}}, \mathbf{k_{13}} = R(120^\circ) \cdot \mathbf{k_{11}} \tag{A.1a}$$

$$\mathbf{k_{21}} = |k_2| \begin{pmatrix} 1 \\ 0 \end{pmatrix}, \mathbf{k_{22}} = R(60^\circ) \cdot \mathbf{k_{21}}, \mathbf{k_{23}} = R(120^\circ) \cdot \mathbf{k_{21}} \tag{A.1b}$$

Here, $|k_1| = 4\pi/(\sqrt{3}a_1)$, and $|k_2| = 4\pi/(\sqrt{3}a_2)$ with a_1 the lattice constant of graphene and a_2 the lattice constant of $NbSe_2$. Because of the C_3 point group symmetry, $\mathbf{k_{12}}$ is generated by rotating $\mathbf{k_{11}}$ of 120°, and $\mathbf{k_{13}}$ is generated by 240° rotation . The rotation matrix $R(\theta)$ is defined as:

$$R(\theta) \equiv \begin{bmatrix} \cos(\theta) & -\sin(\theta) \\ \sin(\theta) & \cos(\theta) \end{bmatrix}.$$

Given the twist angle θ_t between the graphene and $NbSe_2$ layers, and the different values of the lattice constants, the reciprocal vectors of the k_2 in $NbSe_2$ lattice can be related to that of graphene k_1 as:

$$\mathbf{k_{21}} = rR(\theta_t) \cdot \mathbf{k_{11}}, \mathbf{k_{22}} = rR(\theta_t) \cdot \mathbf{k_{12}}, \mathbf{k_{23}} = rR(\theta_t) \cdot \mathbf{k_{13}}, \tag{A.2}$$

where $r = a_1/a_2$ is the ratio of the graphene lattice constant to the $NbSe_2$ lattice.

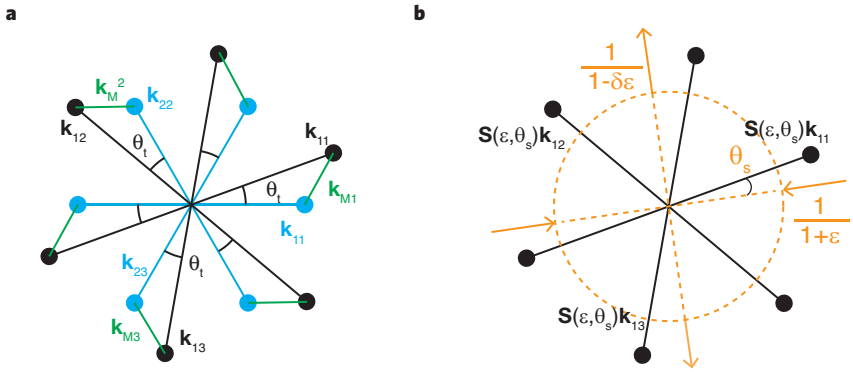

Figure A.1: **Schematic of the moiré pattern in the reciprocal space. a,**The graphene layer is rotated by an angle θ_T relative to the $NbSe_2$ lattice, resulting in a moiré superlattice due to the lattice mismatch. **b,** When uniaxial heterostrain is applied to the top graphene layer, the lattice structure has been modified.

The moiré pattern arises from the lattice mismatch between these two lattices, as shown in Fig. The reciprocal vectors of the moiré pattern are determined by the difference between the graphene and $NbSe_2$:

$$\mathbf{K}_{M1} = \mathbf{k_{11}} - \mathbf{k_{21}}, \mathbf{K}_{M2} = \mathbf{k_{12}} - \mathbf{k_{22}}, \mathbf{K}_{M3} = \mathbf{k_{13}} - \mathbf{k_{23}}, \tag{A.3}$$

For applying a uniaxial heterostrain to the graphene layer, as shown in Fig. A.1b, the strain effect along an arbitrary direction θ_s can be represented by a strain matrix S:

$$\boldsymbol{S}(\epsilon, \theta_s) = \boldsymbol{R}(-\theta_s)\boldsymbol{E}(\epsilon)\boldsymbol{R}(\theta_s), \tag{A.4}$$

where $R(\theta_s)$ is the rotation matrix specifying the strain direction, and $E(\epsilon)$ is the strain matrix when the strain is along k_{11} direction ($\theta_s = 0$):

$$\boldsymbol{S}(\epsilon, 0) = \boldsymbol{E}(\epsilon) = \begin{bmatrix} 1/(1+\epsilon) & 0 \\ 0 & 1/(1-\delta\epsilon) \end{bmatrix}, \tag{A.5}$$

where ϵ is the strain strength and δ is the Poisson ratio of the material ($\delta = 0.16$ for graphene).

As a result, the moiré periodicity with strain is modified to

$$\mathbf{K}_{s1} = \boldsymbol{S}(\epsilon, \theta_s)\mathbf{k_{11}} - \mathbf{k_{21}}, \mathbf{K}_{s2} = \boldsymbol{S}(\epsilon, \theta_s)\mathbf{k_{12}} - \mathbf{k_{22}}, \mathbf{K}_{s3} = \boldsymbol{S}(\epsilon, \theta_s)\mathbf{k_{13}} - \mathbf{k_{23}}. \tag{A.6}$$

Using equation A.2 to replace $\mathbf{k_2}$ by $\mathbf{k_1}$ yields:

$$\mathbf{K}_{s1} = \boldsymbol{S}(\epsilon, \theta_s)\mathbf{k_{11}} - rR(\theta_t)\cdot\mathbf{k_{11}}, \mathbf{K}_{s2} = \boldsymbol{S}(\epsilon, \theta_s)\mathbf{k_{12}} - rR(\theta_t)\cdot\mathbf{k_{12}}, \mathbf{K}_{s3} = \boldsymbol{S}(\epsilon, \theta_s)\mathbf{k_{13}} - rR(\theta_t)\cdot\mathbf{k_{13}}. \tag{A.7}$$

The length of reciprocal vectors of graphene, $NbSe_2$ lattices and the length of Moiré superlattice

can be determined from the FFT patterns. By defining the loss function χ^2 that captures the difference between the calculated $\mathbf{K}s1$, $\mathbf{K}s2$, and $\mathbf{K}s3$ and their experimentally measured counterparts:

$$\chi^2(\theta_{\mathrm{T}}, \theta_{\mathrm{S}}, \epsilon) = \sum_{i=1}^{3} \left| \mathbf{K}_{si}^{\mathrm{measured}} - \mathbf{K}_{si}(\theta_{\mathrm{T}}, \theta_{\mathrm{S}}, \epsilon) \right|^2 .$$

The optimal parameters θ_{T}, θ_{S}, and ϵ are obtained by minimizing the loss function:

$$\min_{\theta_{\mathrm{T}}, \theta_{\mathrm{S}}, \epsilon} \chi^2(\theta_{\mathrm{T}}, \theta_{\mathrm{S}}, \epsilon).$$

Bibliography

[1] N. D. Mermin. Crystalline Order in Two Dimensions. *Phys. Rev.*, 176(1):250–254, 1968. doi: 10.1103/physrev.176.250.

[2] K. S. Novoselov, A. K. Geim, S. V. Morozov, D. Jiang, Y. Zhang, S. V. Dubonos, I. V. Grigorieva, and A. A. Firsov. Electric Field Effect in Atomically Thin Carbon Films. *Science*, 306(5696):666–669, 2004. doi: 10.1126/science.1102896.

[3] B. Radisavljevic, A. Radenovic, J. Brivio, V. Giacometti, and A. Kis. Single-layer MoS2 transistors. *Nat. Nanotechnol.*, 6(3), 2011. doi: 10.1038/nnano.2010.279.

[4] Alexander A. Balandin, Suchismita Ghosh, Wenzhong Bao, Irene Calizo, Desalegne Teweldebrhan, Feng Miao, and Chun Ning Lau. Superior thermal conductivity of single-layer graphene. *Nano Lett.*, 8(3):902–907, 2008. doi: 10.1021/nl0731872.

[5] Mingsheng Xu, Tao Liang, Minmin Shi, and Hongzheng Chen. Graphene-Like Two-Dimensional Materials. *Chem. Rev.*, 113(5):3766–3798, 2013. doi: 10.1021/cr300263a.

[6] Vasilios Georgakilas, Michal Otyepka, Athanasios B. Bourlinos, Vimlesh Chandra, Namdong Kim, K. Christian Kemp, Pavel Hobza, Radek Zboril, and Kwang S. Kim. Functionalization of graphene: Covalent and non-covalent approaches, derivatives and applications. *Chem. Rev.*, 112(11):6156–6214, 2012. doi: 10.1021/cr3000412.

[7] Gordon W. Semenoff. Condensed-Matter Simulation of a Three-Dimensional Anomaly. *Phys. Rev. Lett.*, 53(26):2449–2452, 1984. doi: 10.1103/physrevlett.53.2449.

[8] B. Keimer and J. E. Moore. The physics of quantum materials. *Nat. Phys.*, 13(11): 1045–1055, 2017. doi: 10.1038/nphys4302.

[9] Feliciano Giustino, Jin Hong Lee, Felix Trier, Manuel Bibes, Stephen M Winter, Roser Valent, Young-Woo Son, Louis Taillefer, Christoph Heil, Adriana I Figueroa, Bernard Plaais, QuanSheng Wu, Oleg V Yazyev, Erik P A M Bakkers, Jesper Nygrd, Pol Forn-Daz, Silvano De Franceschi, J W McIver, L E F Foa Torres, Tony Low, Anshuman Kumar, Regina Galceran, Sergio O Valenzuela, Marius V Costache, Aurlien Manchon, Eun-Ah Kim, Gabriel R Schleder, Adalberto Fazzio, and Stephan Roche. The 2021 quantum materials roadmap. *J. Phys.: Mater.*, 3(4):042006, 2020. doi: 10.1088/2515-7639/abb74e.

[10] A. K. Geim and I. V. Grigorieva. Van der Waals heterostructures. *Nature*, 499(7459): 419–425, 2013. doi: 10.1038/nature12385.

[11] Andrew Davies, Juan D. Albar, Alex Summerfield, James C. Thomas, Tin S. Cheng, Vladimir V. Korolkov, Emily Stapleton, James Wrigley, Nathan L. Goodey, Christopher J. Mellor, Andrei N. Khlobystov, Kenji Watanabe, Takashi Taniguchi, C. Thomas Foxon, Laurence Eaves, Sergei V. Novikov, and Peter H. Beton. Lattice-matched epitaxial graphene grown on boron nitride. *Nano Lett.*, 18(1):498–504, 2018. doi: 10.1021/acs.nanolett.7b04453.

[12] K. S. Novoselov, A. Mishchenko, A. Carvalho, and A. H. Castro Neto. 2D materials and van der Waals heterostructures. *Science*, 353(6298):aac9439, 2016. doi: 10.1126/science.aac9439.

[13] Andres Castellanos-Gomez, Xiangfeng Duan, Zhe Fei, Humberto Rodriguez Gutierrez, Yuan Huang, Xinyu Huang, Jorge Quereda, Qi Qian, Eli Sutter, and Peter Sutter. Van der Waals heterostructures. *Nat. Rev. Methods Primers*, 2(1):58, 2022. doi: 10.1038/s43586-022-00139-1.

[14] Dante M. Kennes, Martin Claassen, Lede Xian, Antoine Georges, Andrew J. Millis, James Hone, Cory R. Dean, D. N. Basov, Abhay N. Pasupathy, and Angel Rubio. Moiré heterostructures as a condensed-matter quantum simulator. *Nat. Physics.*, 17(2):155–163, 2021. doi: 10.1038/s41567-020-01154-3.

[15] Eva Y. Andrei, Dmitri K. Efetov, Pablo Jarillo-Herrero, Allan H. MacDonald, Kin Fai Mak, T. Senthil, Emanuel Tutuc, Ali Yazdani, and Andrea F. Young. The marvels of moiré materials. *Nat. Rev. Mater.*, 6(3):201–206, 2021. doi: 10.1038/s41578-021-00284-1.

[16] Jonathan S. Alden, Adam W. Tsen, Pinshane Y. Huang, Robert Hovden, Lola Brown, Jiwoong Park, David A. Muller, and Paul L. McEuen. Strain solitons and topological defects in bilayer graphene. *Proc. Natl. Acad. Sci.*, 110(28):11256–11260, 2013. doi: 10.1073/pnas.1309394110.

[17] Yuya Shimazaki, Ido Schwartz, Kenji Watanabe, Takashi Taniguchi, Martin Kroner, and Ataç Imamoğlu. Strongly correlated electrons and hybrid excitons in a moiré heterostructure. *Nature*, 580(7804):472–477, 2020. doi: 10.1038/s41586-020-2191-2.

[18] Leon Balents, Cory R. Dean, Dmitri K. Efetov, and Andrea F. Young. Superconductivity and strong correlations in moiré flat bands. *Nat. Phys.*, 16(7):725–733, 2020. doi: 10.1038/s41567-020-0906-9.

[19] Matthew Yankowitz, Shaowen Chen, Hryhoriy Polshyn, Yuxuan Zhang, K. Watanabe, T. Taniguchi, David Graf, Andrea F. Young, and Cory R. Dean. Tuning superconductivity in twisted bilayer graphene. *Science*, 363(6431):1059–1064, 2019. doi: 10.1126/science.aav1910.

[20] Rafi Bistritzer and Allan H. MacDonald. Moiré bands in twisted double-layer graphene. *Proc. Natl. Acad. Sci. U.S.A.*, 108(30):12233–12237, 2011. doi: 10.1073/pnas.1108174108.

[21] J. M. B. Lopes dos Santos, N. M. R. Peres, and A. H. Castro Neto. Continuum model of the twisted graphene bilayer. *Phys. Rev. B*, 86(15):155449, 2012. doi: 10.1103/physrevb.86.155449.

[22] Kyounghwan Kim, Ashley DaSilva, Shengqiang Huang, Babak Fallahazad, Stefano Larentis, Takashi Taniguchi, Kenji Watanabe, Brian J. LeRoy, Allan H. MacDonald, and Emanuel Tutuc. Tunable moiré bands and strong correlations in small-twist-angle bilayer graphene. *Proceedings of the National Academy of Sciences*, 114(13):3364–3369, 2017. doi: 10.1073/pnas.1620140114.

[23] Yuan Cao, Valla Fatemi, Ahmet Demir, Shiang Fang, Spencer L. Tomarken, Jason Y. Luo, Javier D. Sanchez-Yamagishi, Kenji Watanabe, Takashi Taniguchi, Efthimios Kaxiras, Ray C. Ashoori, and Pablo Jarillo-Herrero. Correlated insulator behaviour at half-filling in magic-angle graphene superlattices. *Nature*, 556(7699):80–84, 2018. doi: 10.1038/nature26154.

[24] Yuan Cao, Valla Fatemi, Shiang Fang, Kenji Watanabe, Takashi Taniguchi, Efthimios Kaxiras, and Pablo Jarillo-Herrero. Unconventional superconductivity in magic-angle graphene superlattices. *Nature*, 556(7699):43–50, 2018. doi: 10.1038/nature26160.

[25] Xiaobo Lu, Petr Stepanov, Wei Yang, Ming Xie, Mohammed Ali Aamir, Ipsita Das, Carles Urgell, Kenji Watanabe, Takashi Taniguchi, Guangyu Zhang, Adrian Bachtold, Allan H. MacDonald, and Dmitri K. Efetov. Superconductors, orbital magnets and correlated states in magic-angle bilayer graphene. *Nature*, 574(7780):653–657, 2019. doi: 10.1038/s41586-019-1695-0.

[26] Yuan Cao, Daniel Rodan-Legrain, Jeong Min Park, Noah F. Q. Yuan, Kenji Watanabe, Takashi Taniguchi, Rafael M. Fernandes, Liang Fu, and Pablo Jarillo-Herrero. Nematicity and competing orders in superconducting magic-angle graphene. *Science*, 372(6539): 264–271, 2021. doi: 10.1126/science.abc2836.

[27] Y. Kubota, F. Nabeshima, K. Nakayama, H. Ohsumi, Yoshikazu Tanaka, K. Tamasaku, T. Suzuki, K. Okazaki, T. Sato, A. Maeda, and M. Yabashi. Pure nematic state in the iron-based superconductor FeSe. *Phys. Rev. B*, 108(10):L100501, 2023. doi: 10.1103/physrevb.108.l100501.

[28] Subir Sachdev. Colloquium: Order and quantum phase transitions in the cuprate superconductors. *Rev. Mod. Phys.*, 75(3):913–932, 2003. doi: 10.1103/revmodphys.75.913.

[29] Kin Fai Mak and Jie Shan. Semiconductor moiré materials. *Nat. Nanotechnol.*, 17(7): 686–695, 2022. doi: 10.1038/s41565-022-01165-6.

[30] Hongyuan Li, Shaowei Li, Emma C. Regan, Danqing Wang, Wenyu Zhao, Salman Kahn, Kentaro Yumigeta, Mark Blei, Takashi Taniguchi, Kenji Watanabe, Sefaattin Tongay,

Alex Zettl, Michael F. Crommie, and Feng Wang. Imaging two-dimensional generalized Wigner crystals. *Nature*, 597(7878):650–654, 2021. ISSN 0028-0836. doi: 10.1038/s41586-021-03874-9.

[31] Jiaqi Cai, Eric Anderson, Chong Wang, Xiaowei Zhang, Xiaoyu Liu, William Holtzmann, Yinong Zhang, Fengren Fan, Takashi Taniguchi, Kenji Watanabe, Ying Ran, Ting Cao, Liang Fu, Di Xiao, Wang Yao, and Xiaodong Xu. Signatures of fractional quantum anomalous Hall states in twisted MoTe2. *Nature*, 622(7981):63–68, 2023. doi: 10.1038/s41586-023-06289-w.

[32] J. J. Hauser, H. C. Theuerer, and N. R. Werthamer. Proximity effects between superconducting and magnetic films. *Phys. Rev.*, 142(1):118–126, 1966. doi: 10.1103/physrev.142.118.

[33] Ding Zhong, Kyle L. Seyler, Xiayu Linpeng, Nathan P. Wilson, Takashi Taniguchi, Kenji Watanabe, Michael A. McGuire, Kai-Mei C. Fu, Di Xiao, Wang Yao, and Xiaodong Xu. Layer-resolved magnetic proximity effect in van der Waals heterostructures. *Nat. Nanotechnol.*, 15(3):187–191, 2020. doi: 10.1038/s41565-019-0629-1.

[34] B.D. Josephson. Possible new effects in superconductive tunnelling. *Phys. Lett.*, 1(7): 251–253, 1962. doi: 10.1016/0031-9163(62)91369-0.

[35] W. L. McMillan. Tunneling Model of the Superconducting Proximity Effect. *Phys. Rev.*, 175(2):537–542, 1968. doi: 10.1103/physrev.175.537.

[36] Zhiming Zhang, Kenji Watanabe, Takashi Taniguchi, and Brian J. LeRoy. Local characterization and engineering of proximitized correlated states in graphene/NbSe2 vertical heterostructures. *Phys. Rev. B*, 102(8):085429, 2020. doi: 10.1103/physrevb.102.085429.

[37] Shujie Tang, Chaofan Zhang, Dillon Wong, Zahra Pedramrazi, Hsin-Zon Tsai, Chunjing Jia, Brian Moritz, Martin Claassen, Hyejin Ryu, Salman Kahn, Juan Jiang, Hao Yan, Makoto Hashimoto, Donghui Lu, Robert G. Moore, Chan-Cuk Hwang, Choongyu Hwang, Zahid Hussain, Yulin Chen, Miguel M. Ugeda, Zhi Liu, Xiaoming Xie, Thomas P. Devereaux, Michael F. Crommie, Sung-Kwan Mo, and Zhi-Xun Shen. Quantum spin Hall state in monolayer 1T'-WTe2. *Nat. Phys.*, 13(7):683–687, 2017. doi: 10.1038/nphys4174.

[38] Felix Lüpke, Dacen Waters, Sergio C de la Barrera, Michael Widom, David G Mandrus, Jiaqiang Yan, Randall M Feenstra, and Benjamin M Hunt. Proximity-induced superconducting gap in the quantum spin Hall edge state of monolayer WTe2. *Nat. Phys.*, 16: 526–530, 2020. doi: 10.1038/s41567-020-0816-x.

[39] Jose Martinez-Castro, Tobias Wichmann, Keda Jin, Tomas Samuely, Zhongkui Lyu, Oleksander Onufriienko, Pavol Szabo, F Stefan Tautz, Markus Ternes, and Felix Lüpke. One-dimensional topological superconductivity in a van der Waals heterostructure. *arXiv*, 2023. doi: 10.48550/arxiv.2304.08142.

[40] Shawulienu Kezilebieke, Viliam Vano, Md N. Huda, Markus Aapro, Somesh C. Ganguli, Peter Liljeroth, and Jose L. Lado. Moiré-Enabled Topological Superconductivity. *Nano Lett.*, 22(1):328–333, 2022. doi: 10.1021/acs.nanolett.1c03856.

[41] Nikhil Tilak, Michael Altvater, Sheng-Hsiung Hung, Choong-Jae Won, Guohong Li, Taha Kaleem, Sang-Wook Cheong, Chung-Hou Chung, Horng-Tay Jeng, and Eva Y. Andrei. Proximity induced charge density wave in a graphene/1T-TaS2 heterostructure. *Nat. Commun.*, 15(1):8056, 2024. doi: 10.1038/s41467-024-51608-y.

[42] D. M. Eigler and E. K. Schweizer. Positioning single atoms with a scanning tunnelling microscope. *Nature*, 344(6266):524–526, 1990. ISSN 0028-0836. doi: 10.1038/344524a0.

[43] G. Binnig, H. Rohrer, Ch. Gerber, and E. Weibel. Surface Studies by Scanning Tunneling Microscopy. *Phys. Rev. Lett.*, 49(1):57–61, 1982. doi: 10.1103/physrevlett.49.57.

[44] Gerd Binnig and Heinrich Rohrer. Scanning tunneling microscopy—from birth to adolescence. *Rev. Mod. Phys.*, 59(3):615–625, 1987. doi: 10.1103/revmodphys.59.615.

[45] M. F. Crommie, C. P. Lutz, and D. M. Eigler. Imaging standing waves in a two-dimensional electron gas. *Nature*, 363(6429):524–527, 1993. doi: 10.1038/363524a0.

[46] H Kroemer. Quasi-electric fields and band offsets: teaching electrons new tricks, 12 2000. URL http://go.nature.com/5SFA6C. Nobel Lecture.

[47] Zhi-Da Song and B. Andrei Bernevig. Magic-Angle Twisted Bilayer Graphene as a Topological Heavy Fermion Problem. *Phys. Rev. Lett.*, 129(4):047601, 2022. doi: 10.1103/physrevlett.129.047601.

[48] Nikhil Tilak, Xinyuan Lai, Shuang Wu, Zhenyuan Zhang, Mingyu Xu, Raquel de Almeida Ribeiro, Paul C. Canfield, and Eva Y. Andrei. Flat band carrier confinement in magic-angle twisted bilayer graphene. *Nat. Commun.*, 12(1):4180, 2021. doi: 10.1038/s41467-021-24480-3.

[49] Dillon Wong, Kevin P. Nuckolls, Myungchul Oh, Biao Lian, Yonglong Xie, Sangjun Jeon, Kenji Watanabe, Takashi Taniguchi, B. Andrei Bernevig, and Ali Yazdani. Cascade of electronic transitions in magic-angle twisted bilayer graphene. *Nature*, 582(7811):198–202, 2020. ISSN 0028-0836. doi: 10.1038/s41586-020-2339-0.

[50] Lisa M Rütten, Eva Liebhaber, Kai Rossnagel, and Katharina J Franke. Charge-density-wave control by adatom manipulation and its effect on magnetic nanostructures. *arXiv*, 2024. doi: 10.48550/arxiv.2410.02018.

[51] Eva Liebhaber, Lisa M Rütten, Gael Reecht, Jacob F Steiner, Sebastian Rohlf, Kai Rossnagel, Felix von Oppen, and Katharina J Franke. Quantum spins and hybridization in artificially-constructed chains of magnetic adatoms on a superconductor. *Nat. Commun.*, 13(1):2160, 2022. doi: 10.1038/s41467-022-29879-0.

[52] Tiancheng Song, Qi-Chao Sun, Eric Anderson, Chong Wang, Jimin Qian, Takashi Taniguchi, Kenji Watanabe, Michael A. McGuire, Rainer Stöhr, Di Xiao, Ting Cao, Jörg Wrachtrup, and Xiaodong Xu. Direct visualization of magnetic domains and moiré magnetism in twisted 2D magnets. *Science*, 374(6571):1140–1144, 2021. doi: 10.1126/science.abj7478.

[53] Yonglong Xie, Andrew T. Pierce, Jeong Min Park, Daniel E. Parker, Eslam Khalaf, Patrick Ledwith, Yuan Cao, Seung Hwan Lee, Shaowen Chen, Patrick R. Forrester, Kenji Watanabe, Takashi Taniguchi, Ashvin Vishwanath, Pablo Jarillo-Herrero, and Amir Yacoby. Fractional Chern insulators in magic-angle twisted bilayer graphene. *Nature*, 600(7889): 439–443, 2021. doi: 10.1038/s41586-021-04002-3.

[54] Leo Kouwenhoven and Leonid Glazman. Revival of the Kondo effect. *Phys. World*, 14(1): 33–38, 2001. doi: 10.1088/2058-7058/14/1/28.

[55] Markus Ternes, Andreas J Heinrich, and Wolf-Dieter Schneider. Spectroscopic manifestations of the Kondo effect on single adatoms. *J. Condens. Matter Phys.*, 21(5):053001, 2009. doi: 10.1088/0953-8984/21/5/053001.

[56] Steven M Girvin and Kun Yang. *Modern condensed matter physics*. Cambridge University Press, 2019.

[57] GJ Van den Berg and J De Nobel. Les propriétés à basses températures des alliages des métaux «normaux» avec des solutés de transition. *Journal de Physique et le Radium*, 23 (10):665–671, 1962. doi: 10.1051/jphysrad:019620023010066500.

[58] Jun Kondo. Resistance Minimum in Dilute Magnetic Alloys. *Prog. Theor. Phys.*, 32(1): 37–49, 1964. doi: 10.1143/ptp.32.37.

[59] P. W. Anderson. Localized magnetic states in metals. *Phys. Rev.*, 124(1):41–53, 1961. ISSN 0031-899X. doi: 10.1103/physrev.124.41.

[60] V. Madhavan, W. Chen, T. Jamneala, M. F. Crommie, and N. S. Wingreen. Tunneling into a Single Magnetic Atom: Spectroscopic Evidence of the Kondo Resonance. *Science*, 280 (5363):567–569, 1998. doi: 10.1126/science.280.5363.567.

[61] Wolf-Dieter Schneider. A local view of the Kondo effect: Scanning tunneling spectroscopy. *Pramana*, 52(6):537–552, 1999. doi: 10.1007/bf02829862.

[62] R. W. Helmes, T. A. Costi, and A. Rosch. Kondo Proximity Effect: How Does a Metal Penetrate into a Mott Insulator? *Phys. Rev. Lett.*, 101(6):066802, 2008. doi: 10.1103/physrevlett.101.066802.

[63] S. Doniach. The Kondo lattice and weak antiferromagnetism. *Phys. B+C*, 91:231–234, 1977. doi: 10.1016/0378-4363(77)90190-5.

[64] Chuan Chen, Inti Sodemann, and Patrick A. Lee. Competition of spinon Fermi surface and heavy Fermi liquid states from the periodic Anderson to the Hubbard model. *Phys. Rev. B*, 103(8):085128, 2021. doi: 10.1103/physrevb.103.085128.

[65] George Gruner. *Density waves in solids*. CRC press, 2018. doi: 10.1201/9780429501012-10.

[66] Stephen Edkins. *Visualising the charge and Cooper-pair density waves in cuprates*. Springer, 2017. doi: 10.1007/978-3-319-65975-6.

[67] Kazuhiro Fujita, Mohammad H. Hamidian, Stephen D. Edkins, Chung Koo Kim, Yuhki Kohsaka, Masaki Azuma, Mikio Takano, Hidenori Takagi, Hiroshi Eisaki, Shin-ichi Uchida, Andrea Allais, Michael J. Lawler, Eun-Ah Kim, Subir Sachdev, and J. C. Séamus Davis. Direct phase-sensitive identification of a d-form factor density wave in underdoped cuprates. *Proc. Natl. Acad. Sci.*, 111(30):E3026–E3032, 2014. doi: 10.1073/pnas.1406297111.

[68] M. H. Hamidian, S. D. Edkins, Chung Koo Kim, J. C. Davis, A. P. Mackenzie, H. Eisaki, S. Uchida, M. J. Lawler, E.-A. Kim, S. Sachdev, and K. Fujita. Atomic-scale electronic structure of the cuprate d-symmetry form factor density wave state. *Nat. Phys.*, 12(2):150–156, 2016. doi: 10.1038/nphys3519.

[69] R. E. Peierls. *Quantum Theory of Solids*. Oxford University Press, 02 2001. ISBN 9780198507819. doi: 10.1093/acprof:oso/9780198507819.001.0001.

[70] Xuetao Zhu, Yanwei Cao, Jiandi Zhang, E. W. Plummer, and Jiandong Guo. Classification of charge density waves based on their nature. *Proc. National Acad. Sci.*, 112(8):2367–2371, 2015. doi: 10.1073/pnas.1424791112.

[71] M. D. Johannes and I. I. Mazin. Fermi surface nesting and the origin of charge density waves in metals. *Phys. Rev. B*, 77(16):165135, 2007. doi: 10.1103/physrevb.77.165135.

[72] K Rossnagel. On the origin of charge-density waves in select layered transition-metal dichalcogenides. *J. Phys.: Condens. Matter*, 23(21):213001, 2011. doi: 10.1088/0953-8984/23/21/213001.

[73] Miguel M. Ugeda, Aaron J. Bradley, Yi Zhang, Seita Onishi, Yi Chen, Wei Ruan, Claudia Ojeda-Aristizabal, Hyejin Ryu, Mark T. Edmonds, Hsin-Zon Tsai, Alexander Riss, Sung-Kwan Mo, Dunghai Lee, Alex Zettl, Zahid Hussain, Zhi-Xun Shen, and Michael F. Crommie. Characterization of collective ground states in single-layer NbSe2. *Nat. Phys.*, 12(1):92–97, 2016. doi: 10.1038/nphys3527.

[74] Matteo Calandra, I. I. Mazin, and Francesco Mauri. Effect of dimensionality on the charge-density wave in few-layer 2h-NbSe2. *Phys. Rev. B*, 80(24):241108, 2009. doi: 10.1103/physrevb.80.241108.

[75] C. J. Arguello, S. P. Chockalingam, E. P. Rosenthal, L. Zhao, C. Gutiérrez, J. H. Kang, W. C. Chung, R. M. Fernandes, S. Jia, A. J. Millis, R. J. Cava, and A. N. Pasupathy. Visualizing the charge density wave transition in 2H-NbSe2 in real space. *Phys. Rev. B*, 89(23):235115, 2014. doi: 10.1103/physrevb.89.235115.

[76] Shaoxiang Sheng, Mohamad Abdo, Steffen Rolf-Pissarczyk, Kurt Lichtenberg, Susanne Baumann, Jacob A J Burgess, Luigi Malavolti, and Sebastian Loth. Terahertz spectroscopy of collective charge density wave dynamics at the atomic scale. *Nat. Phys.*, 20(10):1603–1608, 2024. doi: 10.1038/s41567-024-02552-7.

[77] Arpad Pasztor, Alessandro Scarfato, Marcello Spera, Celine Barreteau, Enrico Giannini, and Christoph Renner. Holographic imaging of the complex charge density wave order parameter. *Phys. Rev. Res.*, 1(3):033114, 2019. doi: 10.1103/physrevresearch.1.033114.

[78] Arpad Pasztor, Alessandro Scarfato, Marcello Spera, Felix Flicker, Céline Barreteau, Enrico Giannini, Jasper van Wezel, and Christoph Renner. Multiband charge density wave exposed in a transition metal dichalcogenide. *Nat. Commun*, 12(1):6037, 2021. doi: 10.1038/s41467-021-25780-4.

[79] Kevin P. Nuckolls, Ryan L. Lee, Myungchul Oh, Dillon Wong, Tomohiro Soejima, Jung Pyo Hong, Dumitru Călugăru, Jonah Herzog-Arbeitman, B. Andrei Bernevig, Kenji Watanabe, Takashi Taniguchi, Nicolas Regnault, Michael P. Zaletel, and Ali Yazdani. Quantum textures of the many-body wavefunctions in magic-angle graphene. *Nature*, 620(7974):525–532, 2023. doi: 10.1038/s41586-023-06226-x.

[80] Ke Bian, Christoph Gerber, Andreas J. Heinrich, Daniel J. Müller, Simon Scheuring, and Ying Jiang. Scanning probe microscopy. *Nat. Rev. Methods Primers*, 1(1):36, 2021. doi: 10.1038/s43586-021-00033-2.

[81] Samir Lounis. Theory of Scanning Tunneling Microscopy. *arXiv*, 2014. doi: 10.48550/arxiv.1404.0961.

[82] Bert Voigtländer. *Scanning Probe Microscopy*. Springer Berlin, Heidelberg, 2015. doi: 10.1007/978-3-662-45240-0.

[83] R.J. Hamers. *Scanning Probe Microscopy*. Wiley-VCH New York, 1993. doi: 10.21236/ada266507.

[84] Harald Ibach. *Physics of surfaces and interfaces*, volume 12. Springer, 2006. doi: 10.1007/3-540-34710-0.

[85] Andres Castellanos-gomez, Michele Buscema, and Rianda Molenaar. Deterministic transfer of two-dimensional materials by all-dry viscoelastic stamping. *2d Mater.*, 1:011002, 2014. doi: 10.1088/2053-1583/1/1/011002.

[86] James McKenzie, Nileema Sharma, and Xiaolong Liu. Fabrication of pristine 2D heterostructures for scanning probe microscopy. *APL Mater.*, 12(7):070602, 2024. doi: 10.1063/5.0213542.

[87] Filippo Pizzocchero, Lene Gammelgaard, Bjarke S. Jessen, Jose M. Caridad, Lei Wang, James Hone, Peter Bøggild, and Timothy J. Booth. The hot pick-up technique for batch assembly of van der Waals heterostructures. *Nat. Commun.*, 7(1):11894, 2016. doi: 10.1038/ncomms11894.

[88] Suhan Son, Young Jae Shin, Kaixuan Zhang, Jeacheol Shin, Sungmin Lee, Hiroshi Idzuchi, Matthew J Coak, Hwangsun Kim, Jangwon Kim, Jae Hoon Kim, Miyoung Kim, Dohun Kim, Philip Kim, and Je-geun Park. Strongly adhesive dry transfer technique for van der Waals heterostructure. *2D Mater.*, 7:041005, 2020. doi: 10.1088/2053-1583/abad0b.

[89] Yusai Wakafuji, Rai Moriya, Satoru Masubuchi, Kenji Watanabe, Takashi Taniguchi, and Tomoki Machida. 3D Manipulation of 2D Materials Using Microdome Polymer. *Nano Lett.*, 20:2486–2492, 2020. doi: 10.1021/acs.nanolett.9b05228.

[90] I G Rebollo, F C Rodrigues-Machado, W Wright, G J Melin, and A R Champagne. Thin-suspended 2D materials: facile, versatile, and deterministic transfer assembly. *2D Mater.*, 8(3):035028, 2021. doi: 10.1088/2053-1583/abf98c.

[91] Y. Cao, A. Mishchenko, G. L. Yu, E. Khestanova, A. P. Rooney, E. Prestat, A. V. Kretinin, P. Blake, M. B. Shalom, C. Woods, J. Chapman, G. Balakrishnan, I. V. Grigorieva, K. S. Novoselov, B. A. Piot, M. Potemski, K. Watanabe, T. Taniguchi, S. J. Haigh, A. K. Geim, and R. V. Gorbachev. Quality heterostructures from two-dimensional crystals unstable in air by their assembly in inert atmosphere. *Nano Lett.*, 15(8):4914–4921, 2015. doi: 10.1021/acs.nanolett.5b00648.

[92] Zhizhan Qiu, Matthew Holwill, Thomas Olsen, Pin Lyu, Jing Li, Hanyan Fang, Huimin Yang, Mikhail Kashchenko, Kostya S Novoselov, and Jiong Lu. Visualizing atomic structure and magnetism of 2D magnetic insulators via tunneling through graphene. *Nat. Commun.*, 12(1):70, 2021. doi: 10.1038/s41467-020-20376-w.

[93] Yang Xu, Ariana Ray, Yu-Tsun Shao, Shengwei Jiang, Kihong Lee, Daniel Weber, Joshua E. Goldberger, Kenji Watanabe, Takashi Taniguchi, David A. Muller, Kin Fai Mak, and Jie Shan. Coexisting ferromagnetic–antiferromagnetic state in twisted bilayer CrI3. *Nat. Nanotechnol.*, 17(2):143–147, 2022. doi: 10.1038/s41565-021-01014-y.

[94] A. M. Goossens, V. E. Calado, A. Barreiro, Kenji Watanabe, Takashi Taniguchi, and Lieven M.K. Vandersypen. Mechanical cleaning of graphene. *Appl. Phys. Lett.*, 100: 073110, 2012. doi: 10.1063/1.3685504.

[95] Jose Martinez-Castro, Diego Mauro, Árpád Pásztor, Ignacio Gutiérrez-Lezama, Alessandro Scarfato, Alberto F. Morpurgo, and Christoph Renner. Scanning Tunneling Microscopy of an Air Sensitive Dichalcogenide Through an Encapsulating Layer. *Nano Lett.*, 18:6696–6702, 2018. doi: 10.1021/acs.nanolett.8b01978.

[96] Iréne Cucchi, Ignacio Gutierrez-Lezama, Edoardo Cappelli, Siobhan McKeown Walker, Flavio Y Bruno, Giulia Tenasini, Lin Wang, Nicolas Ubrig, Céline Barreteau, Enrico

Giannini, Marco Gibertini, Anna Tamai, Alberto F Morpurgo, and Felix Baumberger. Microfocus Laser-Angle-Resolved Photoemission on Encapsulated Mono-, Bi-, and Few-Layer 1T'-WTe 2. *Nano Lett.*, 19:554–560, 2019. doi: 10.1021/acs.nanolett.8b04534.

[97] Kyounghwan Kim, Matthew Yankowitz, Babak Fallahazad, Sangwoo Kang, Hema C. P. Movva, Shengqiang Huang, Stefano Larentis, Chris M. Corbet, Takashi Taniguchi, Kenji Watanabe, Sanjay K. Banerjee, Brian J. LeRoy, and Emanuel Tutuc. van der Waals Heterostructures with High Accuracy Rotational Alignment. *Nano Lett.*, 16(3):1989–1995, 2016. doi: 10.1021/acs.nanolett.5b05263.

[98] Felix Lüpke, Dacen Waters, Anh D. Pham, Jiaqiang Yan, David G. Mandrus, Panchapakesan Ganesh, and Benjamin M. Hunt. Quantum spin hall edge states and interlayer coupling in twisted bilayer wte2. *Nano Lett.*, 22(14):5674–5680, 2022. doi: 10.1021/acs.nanolett.2c00432.

[99] Dmitry Shcherbakov, Petr Stepanov, Daniel Weber, Yaxian Wang, Jin Hu, Yanglin Zhu, Kenji Watanabe, Takashi Taniguchi, Zhiqiang Mao, Wolfgang Windl, Joshua Goldberger, Marc Bockrath, and Chun Ning Lau. Raman Spectroscopy, Photocatalytic Degradation, and Stabilization of Atomically Thin Chromium Tri-iodide. *Nano Lett.*, 18:4214–4219, 2018. doi: 10.1021/acs.nanolett.8b01131.

[100] Eike Icking, Luca Banszerus, Frederike Wörtche, Frank Volmer, Philipp Schmidt, Corinne Steiner, Stephan Engels, Jonas Hesselmann, Matthias Goldsche, Kenji Watanabe, Takashi Taniguchi, Christian Volk, Bernd Beschoten, and Christoph Stampfer. Transport Spectroscopy of Ultraclean Tunable Band Gaps in Bilayer Graphene. *Adv. Electron. Mater.*, 8 (11):2200510, 2022. doi: 10.1002/aelm.202200510.

[101] Florian Sigger, Hendrik Lambers, Katharina Nisi, Julian Klein, Nihit Saigal, Alexander W. Holleitner, and Ursula Wurstbauer. Spectroscopic imaging ellipsometry of two-dimensional TMDC heterostructures. *Appl. Phys. Lett.*, 121(7):071102, 2022. doi: 10.1063/5.0109189.

[102] Bharti Parashar, Lars Rathmann, Hyun-Jung Kim, Iulia Cojocariu, Aaron Bostwick, Chris Jozwiak, Eli Rotenberg, José Avila, Pavel Dudin, Vitaliy Feyer, Christoph Stampfer, Bernd Beschoten, Gustav Bihlmayer, Claus M. Schneider, and Lukasz Plucinski. Photoemission study of twisted monolayers and bilayers of wse_2 on graphite substrates. *Phys. Rev. Mater.*, 7:044004, 2023. doi: 10.1103/physrevmaterials.7.044004.

[103] Bálint Fülöp, Albin Márffy, Simon Zihlmann, Martin Gmitra, Endre Tóvári, Bálint Szentpéteri, Máté Kedves, Kenji Watanabe, Takashi Taniguchi, Jaroslav Fabian, Christian Schönenberger, Péter Makk, and Szabolcs Csonka. Boosting proximity spin-orbit coupling in graphene/WSe2 heterostructures via hydrostatic pressure. *npj 2D Mater. Appl.*, 5:82, 2021. doi: 10.1038/s41699-021-00262-9.

[104] Mengqiao Sui, Guorui Chen, Liguo Ma, Wen Yu Shan, Dai Tian, Kenji Watanabe, Takashi Taniguchi, Xiaofeng Jin, Wang Yao, Di Xiao, and Yuanbo Zhang. Gate-tunable topological

valley transport in bilayer graphene. *Nat. Phys.*, 11:1027–1031, 2015. doi: 10.1038/nphys3485.

[105] Zhe Wang, Dong Keun Ki, Jun Yong Khoo, Diego Mauro, Helmuth Berger, Leonid S. Levitov, and Alberto F. Morpurgo. Origin and magnitude of 'designer' spin-orbit interaction in graphene on semiconducting transition metal dichalcogenides. *Phys. Rev. X*, 6: 041020, 2016. doi: 10.1103/PhysRevX.6.041020.

[106] Nathan P. Wilson, Kihong Lee, John Cenker, Kaichen Xie, Avalon H. Dismukes, Evan J. Telford, Jordan Fonseca, Shivesh Sivakumar, Cory Dean, Ting Cao, Xavier Roy, Xiaodong Xu, and Xiaoyang Zhu. Interlayer electronic coupling on demand in a 2D magnetic semiconductor. *Nat. Mater.*, 20:1657–1662, 2021. doi: 10.1038/s41563-021-01070-8.

[107] Jonghwan Kim, Chenhao Jin, Bin Chen, Hui Cai, Tao Zhao, Puiyee Lee, Salman Kahn, Kenji Watanabe, Takashi Taniguchi, Sefaattin Tongay, Michael F. Crommie, and Feng Wang. Observation of ultralong valley lifetime in WSe2/MoS2 heterostructures. *Sci. Adv.*, 3:1700518, 2017. doi: 10.1126/sciadv.1700518.

[108] Momoko Onodera, Yusai Wakafuji, Taketo Hashimoto, Satoru Masubuchi, Rai Moriya, Yijin Zhang, Kenji Watanabe, Takashi Taniguchi, and Tomoki Machida. All-dry flip-over stacking of van der Waals junctions of 2D materials using polyvinyl chloride. *Sci. Rep.*, 12:21963, 2022. doi: 10.1038/s41598-022-26193-z.

[109] Jeffrey J. Schwartz, Hsun-Jen Chuang, Matthew R. Rosenberger, Saujan V. Sivaram, Kathleen M. McCreary, Berend T. Jonker, and Andrea Centrone. Chemical identification of interlayer contaminants within van der waals heterostructures. *ACS Appl Mater Interfaces*, 11(28):25578–25585, 2019. doi: 10.1021/acsami.9b06594.

[110] B Giambattista, A Johnson, R V Coleman, B Drake, and P K Hansma. Charge-density waves observed at 4.2 K by scanning-tunneling microscopy. *Phys. Rev. B*, 37(5):2741–2744, 1988.

[111] Masatoshi Imada, Atsushi Fujimori, and Yoshinori Tokura. Metal-insulator transitions. *Rev. Mod. Phys.*, 70(4):1039–1263, 1998. doi: 10.1103/revmodphys.70.1039.

[112] Leon Balents. Spin liquids in frustrated magnets. *Nature*, 464(7286):199–208, 2010. doi: 10.1038/nature08917.

[113] F. Kadijk and F. Jellinek. On the polymorphism of niobium diselenide. *J. Less Common Met.*, 23(4):437–441, 1971. doi: 10.1016/0022-5088(71)90053-1.

[114] R. F. Frindt. Superconductivity in Ultrathin NbSe2 Layers. *Phys. Rev. Lett.*, 28(5):299–301, 1971. doi: 10.1103/physrevlett.28.299.

[115] Jan Berges. *Many-body instabilities in two-dimensional materials*. PhD thesis, University of Bremen, 2020.

[116] Yuki Nakata, Katsuaki Sugawara, Ryota Shimizu, Yoshinori Okada, Patrick Han, Taro Hitosugi, Keiji Ueno, Takafumi Sato, and Takashi Takahashi. Monolayer 1T-NbSe2 as a Mott insulator. *NPG Asia Mater.*, 8(11):e321–e321, 2016. doi: 10.1038/am.2016.157.

[117] Zhen-Yu Liu, Shuang Qiao, Bing Huang, Qiao-Yin Tang, Zi-Heng Ling, Wen-Hao Zhang, Hui-Nan Xia, Xin Liao, Hu Shi, Wen-Hao Mao, Gui-Lin Zhu, Jing-Tao Lv, and Ying-Shuang Fu. Charge Transfer Gap Tuning via Structural Distortion in Monolayer 1T-NbSe2. *Nano Lett.*, 21(16):7005–7011, 2021. doi: 10.1021/acs.nanolett.1c02348.

[118] Mengke Liu, Joshua Leveillee, Shuangzan Lu, Jia Yu, Hyunsue Kim, Cheng Tian, Youguo Shi, Keji Lai, Chendong Zhang, Feliciano Giustino, and Chih-Kang Shih. Monolayer 1T-NbSe2 as a 2D-correlated magnetic insulator. *Sci. Adv.*, 7(47):eabi6339, 2021. doi: 10.1126/sciadv.abi6339.

[119] Liwei Liu, Han Yang, Yuting Huang, Xuan Song, Quanzhen Zhang, Zeping Huang, Yanhui Hou, Yaoyao Chen, Ziqiang Xu, Teng Zhang, Xu Wu, Jiatao Sun, Yuan Huang, Fawei Zheng, Xianbin Li, Yugui Yao, Hong-Jun Gao, and Yeliang Wang. Direct identification of Mott Hubbard band pattern beyond charge density wave superlattice in monolayer 1T-NbSe2. *Nat. Commun.*, 12(1):1978, 2021. doi: 10.1038/s41467-021-22233-w.

[120] Yi Chen, Wen-Yu He, Wei Ruan, Jinwoong Hwang, Shujie Tang, Ryan L. Lee, Meng Wu, Tiancong Zhu, Canxun Zhang, Hyejin Ryu, Feng Wang, Steven G. Louie, Zhi-Xun Shen, Sung-Kwan Mo, Patrick A. Lee, and Michael F. Crommie. Evidence for a spinon Kondo effect in cobalt atoms on single-layer 1T-TaSe2. *Nat. Phys.*, 18(11):1335–1340, 2022. doi: 10.1038/s41567-022-01751-4.

[121] Wen-Yu He and Patrick A. Lee. Magnetic impurity as a local probe of the U(1) quantum spin liquid with spinon Fermi surface. *Phys. Rev. B*, 105(19):195156, 2022. doi: 10.1103/physrevb.105.195156.

[122] Quanzhen Zhang, Wen-Yu He, Yu Zhang, Yaoyao Chen, Liangguang Jia, Yanhui Hou, Hongyan Ji, Huixia Yang, Teng Zhang, Liwei Liu, Hong-Jun Gao, Thomas A. Jung, and Yeliang Wang. Quantum spin liquid signatures in monolayer 1T-NbSe2. *Nat. Commun.*, 15(1):2336, 2024. doi: 10.1038/s41467-024-46612-1.

[123] Xin Huang, Jose L Lado, Jani Sainio, Peter Liljeroth, and Somesh Chandra Ganguli. Doped Mott phase and charge correlations in monolayer 1T-NbSe2. *arXiv*, 2024. doi: 10.48550/arxiv.2401.08296.

[124] Zhen-Yu Liu, Heng Jin, Yao Zhang, Kai Fan, Ting-Fei Guo, Hao-Jun Qin, Lan-Fang Zhu, Lian-Zhi Yang, Wen-Hao Zhang, Bing Huang, and Ying-Shuang Fu. Charge-density wave mediated quasi-one-dimensional Kondo lattice in stripe-phase monolayer 1T-NbSe2. *Nat. Commun.*, 15(1):1039, 2024. doi: 10.1038/s41467-024-45335-7.

[125] Wen Wan, Rishav Harsh, Antonella Meninno, Paul Dreher, Sandra Sajan, Haojie Guo, Ion Errea, Fernando de Juan, and Miguel M Ugeda. Evidence for ground state coherence in

a two-dimensional Kondo lattice. *Nat. Commun.*, 14(1):7005, 2023. doi: 10.1038/s41467-023-42803-4.

[126] Aline Ramires and Jose L. Lado. Emulating Heavy Fermions in Twisted Trilayer Graphene. *Phys. Rev. Lett.*, 127(2):026401, 2021. doi: 10.1103/physrevlett.127.026401.

[127] Alexander Cyril Hewson. *The Kondo Problem to Heavy Fermions*. Cambridge University Press, 1993. doi: 10.1017/cbo9780511470752.

[128] Lorenzo Crippa, Hyeonhu Bae, Paul Wunderlich, Igor I. Mazin, Binghai Yan, Giorgio Sangiovanni, Tim Wehling, and Roser Valentí. Heavy fermions vs doped Mott physics in heterogeneous Ta-dichalcogenide bilayers. *Nat. Commun.*, 15(1):1357, 2024. doi: 10.1038/s41467-024-45392-y.

[129] Viliam Vaňo, Mohammad Amini, Somesh C. Ganguli, Guangze Chen, Jose L. Lado, Shawulienu Kezilebieke, and Peter Liljeroth. Artificial heavy fermions in a van der Waals heterostructure. *Nature*, 599(7886):582–586, 2021. doi: 10.1038/s41586-021-04021-0.

[130] Cosme G Ayani, Michele Pisarra, Iván M Ibarburu, Manuela Garnica, Rodolfo Miranda, Fabián Calleja, Fernando Martín, and Amadeo L Vázquez de Parga. Probing the Phase Transition to a Coherent 2D Kondo Lattice. *Small*, 20(8), 2024. doi: 10.1002/smll.202303275.

[131] M. B. J. Meinders, H. Eskes, and G. A. Sawatzky. Spectral-weight transfer: Breakdown of low-energy-scale sum rules in correlated systems. *Phys. Rev. B*, 48(6):3916–3926, 1993. doi: 10.1103/physrevb.48.3916.

[132] Sindhunil Barman Roy. *Mott Insulators*. 2053-2563. IOP Publishing, 2019. doi: 10.1088/2053-2563/ab16c9.

[133] Eva Liebhaber, Sergio Acero Gonzalez, Rojhat Baba, Gael Reecht, Benjamin W. Heinrich, Sebastian Rohlf, Kai Rossnagel, Felix von Oppen, and Katharina J. Franke. Yu–Shiba–Rusinov States in the Charge-Density Modulated Superconductor NbSe2. *Nano Lett.*, 20(1):339–344, 2020. doi: 10.1021/acs.nanolett.9b03988.

[134] Lisa M Rütten, Eva Liebhaber, Kai Rossnagel, and Katharina J Franke. Charge-density-wave control by adatom manipulation and its effect on magnetic nanostructures. *arXiv*, 2024. doi: 10.48550/arxiv.2410.02018.

[135] Zongxiu Wu, Kunliang Bu, Wenhao Zhang, Ying Fei, Yuan Zheng, Jingjing Gao, Xuan Luo, Zheng Liu, Yu-Ping Sun, and Yi Yin. Effect of stacking order on the electronic state of 1T-TaS2. *Phys. Rev. B*, 105(3):035109, 2022. doi: 10.1103/physrevb.105.035109.

[136] Markus Ternes, Christopher P. Lutz, Andreas J. Heinrich, and Wolf-Dieter Schneider. Sensing the Spin of an Individual Ce Adatom. *Phys. Rev. Lett.*, 124(16):167202, 2020. doi: 10.1103/physrevlett.124.167202.

[137] Markus Ternes. *Scanning tunneling spectroscopy at the single atom scale*. PhD thesis, EPFL, Lausanne, 2006. URL https://infoscience.epfl.ch/handle/20.500.14299/221680.

[138] K. T. Law and Patrick A. Lee. 1t-TaS2 as a quantum spin liquid. *Proc National Acad Sci*, 114(27):6996–7000, 2017. doi: 10.1073/pnas.1706769114.

[139] Jose L Lado and Peter Liljeroth. Designer quantum matter in van der Waals heterostructures. *arXiv*, 2021. doi: 10.48550/arxiv.2102.11779.

[140] P. San-Jose, J. González, and F. Guinea. Non-Abelian Gauge Potentials in Graphene Bilayers. *Phys. Rev. Lett.*, 108(21):216802, 2012. doi: 10.1103/physrevlett.108.216802.

[141] Aline Ramires and Jose L. Lado. Electrically Tunable Gauge Fields in Tiny-Angle Twisted Bilayer Graphene. *Phys. Rev. Lett.*, 121(14):146801, 2018. doi: 10.1103/physrevlett.121.146801.

[142] Mit H. Naik, Sudipta Kundu, Indrajit Maity, and Manish Jain. Origin and evolution of ultraflat bands in twisted bilayer transition metal dichalcogenides: Realization of triangular quantum dots. *Phys. Rev. B*, 102(7):075413, 2020. doi: 10.1103/physrevb.102.075413.

[143] Zhiming Zhang, Yimeng Wang, Kenji Watanabe, Takashi Taniguchi, Keiji Ueno, Emanuel Tutuc, and Brian J. LeRoy. Flat bands in twisted bilayer transition metal dichalcogenides. *Nat. Phys.*, 16(11):1093–1096, 2020. doi: 10.1038/s41567-020-0958-x.

[144] Chendong Zhang, Chih-Piao Chuu, Xibiao Ren, Ming-Yang Li, Lain-Jong Li, Chuanhong Jin, Mei-Yin Chou, and Chih-Kang Shih. Interlayer couplings, Moiré patterns, and 2D electronic superlattices in MoS2/WSe2 hetero-bilayers. *Sci. Adv.*, 3(1), 2017. doi: 10.1126/sciadv.1601459.

[145] Kevin Peter Nuckolls. *Electronic Correlations, Topology, and Unconventional Superconductivity in Twisted Bilayer Graphene*. Princeton, NJ: Princeton University, 2023. URL http://arks.princeton.edu/ark:/88435/dsp01t148fm400.

[146] Yuhang Jiang, Xinyuan Lai, Kenji Watanabe, Takashi Taniguchi, Kristjan Haule, Jinhai Mao, and Eva Y. Andrei. Charge order and broken rotational symmetry in magic-angle twisted bilayer graphene. *Nature*, 573(7772):91–95, 2019. doi: 10.1038/s41586-019-1460-4.

[147] Carmen Rubio-Verdu, Simon Turkel, Yuan Song, Lennart Klebl, Rhine Samajdar, Mathias S. Scheurer, Jörn W. F. Venderbos, Kenji Watanabe, Takashi Taniguchi, Héctor Ochoa, Lede Xian, Dante M. Kennes, Rafael M. Fernandes, Angel Rubio, and Abhay N. Pasupathy. Moiré nematic phase in twisted double bilayer graphene. *Nat. Phys.*, 18(2):196–202, 2022. doi: 10.1038/s41567-021-01438-2.

[148] Caiyun Chen, Jiangchang Zheng, Ruopeng Yu, Soumya Sankar, Kam Tuen Law, Hoi Chun Po, and Berthold Jäck. Visualizing the localized electrons of a kagome flat band. *Phys. Rev. Res.*, 5(4):043269, 2023. doi: 10.1103/physrevresearch.5.043269.

[149] Caiyun Chen, Jiangchang Zheng, Yuman He, Xuzhe Ying, Soumya Sankar, Luanjing Li, Yizhou Wei, Xi Dai, Hoi Chun Po, and Berthold Jäck. Cascade of strongly correlated quantum states in a partially filled kagome flat band. *arXiv*, 2024. doi: 10.48550/arxiv.2409.06933.

[150] Yiran Zhang, Robert Polski, Cyprian Lewandowski, Alex Thomson, Yang Peng, Youngjoon Choi, Hyunjin Kim, Kenji Watanabe, Takashi Taniguchi, Jason Alicea, Felix von Oppen, Gil Refael, and Stevan Nadj-Perge. Promotion of superconductivity in magic-angle graphene multilayers. *Science*, 377(6614):1538–1543, 2022. ISSN 0036-8075.

[151] Ruiheng Su, Manabendra Kuiri, Kenji Watanabe, Takashi Taniguchi, and Joshua Folk. Superconductivity in twisted double bilayer graphene stabilized by WSe2. *Nat. Mater.*, 22(11):1332–1337, 2023. doi: 10.1038/s41563-023-01653-7.

[152] Hanbin Deng, Hailang Qin, Guowei Liu, Tianyu Yang, Ruiqing Fu, Zhongyi Zhang, Xianxin Wu, Zhiwei Wang, Youguo Shi, Jinjin Liu, Hongxiong Liu, Xiao-Yu Yan, Wei Song, Xitong Xu, Yuanyuan Zhao, Mingsheng Yi, Gang Xu, Hendrik Hohmann, Sofie Castro Holbæk, Matteo Dürrnagel, Sen Zhou, Guoqing Chang, Yugui Yao, Qianghua Wang, Zurab Guguchia, Titus Neupert, Ronny Thomale, Mark H. Fischer, and Jia-Xin Yin. Chiral kagome superconductivity modulations with residual Fermi arcs. *Nature*, 632 (8026):775–781, 2024. doi: 10.1038/s41586-024-07798-y.

[153] Patrick Zeller and Sebastian Günther. What are the possible moiré patterns of graphene on hexagonally packed surfaces? Universal solution for hexagonal coincidence lattices, derived by a geometric construction. *N. J. of Phys.*, 16(8):083028, 2014. doi: 10.1088/1367-2630/16/8/083028.

[154] Alexander Kerelsky, Leo J. McGilly, Dante M. Kennes, Lede Xian, Matthew Yankowitz, Shaowen Chen, K. Watanabe, T. Taniguchi, James Hone, Cory Dean, Angel Rubio, and Abhay N. Pasupathy. Maximized electron interactions at the magic angle in twisted bilayer graphene. *Nature*, 2019. doi: 10.1038/s41586-019-1431-9.

[155] Pranab Kumar Nag, Rajib Batabyal, Julian Ingham, Noam Morali, Hengxin Tan, Jahyun Koo, Armando Consiglio, Enke Liu, Nurit Avraham, Raquel Queiroz, Ronny Thomale, Binghai Yan, Claudia Felser, and Haim Beidenkopf. Pomeranchuk Instability Induced by an Emergent Higher-Order van Hove Singularity on the Distorted Kagome Surface of Co3Sn2S2. *arXiv*, 2024. doi: 2410.01994.

[156] E Kamil, J Berges, G Schönhoff, M Rösner, M Schüler, G Sangiovanni, and T O Wehling. Electronic structure of single layer 1T-NbSe2: interplay of lattice distortions, non-local exchange, and Mott–Hubbard correlations. *J. Phys. Condens. Matter*, 30(32):325601, 2018. doi: 10.1088/1361-648x/aad215.

[157] N. D. Mermin and H. Wagner. Absence of Ferromagnetism or Antiferromagnetism in One- or Two-Dimensional Isotropic Heisenberg Models. *Phys. Rev. Lett.*, 17(22): 1133–1136, 1966. doi: 10.1103/physrevlett.17.1133.

[158] Cheng Gong, Lin Li, Zhenglu Li, Huiwen Ji, Alex Stern, Yang Xia, Ting Cao, Wei Bao, Chenzhe Wang, Yuan Wang, Z. Q. Qiu, R. J. Cava, Steven G. Louie, Jing Xia, and Xiang Zhang. Discovery of intrinsic ferromagnetism in two-dimensional van der waals crystals. *Nature*, 546(7657):265–269, 2017. ISSN 0028-0836. doi: 10.1038/nature22060.

[159] Bevin Huang, Genevieve Clark, Efrén Navarro-Moratalla, Dahlia R. Klein, Ran Cheng, Kyle L. Seyler, Ding Zhong, Emma Schmidgall, Michael A. McGuire, David H. Cobden, Wang Yao, Di Xiao, Pablo Jarillo-Herrero, and Xiaodong Xu. Layer-dependent ferromagnetism in a van der Waals crystal down to the monolayer limit. *Nature*, 546(7657): 270–273, 2017. doi: 10.1038/nature22391.

[160] J L Lado and J Fernandez-Rossier. On the origin of magnetic anisotropy in two dimensional CrI3. *2D Mater.*, 4(3):035002, 2017. doi: 10.1088/2053-1583/aa75ed.

[161] P. W. Anderson. Antiferromagnetism. Theory of Superexchange Interaction. *Phys. Rev.*, 79(2):350–356, 1950. doi: 10.1103/physrev.79.350.

[162] Lebing Chen, Jae-Ho Chung, Tong Chen, Chunruo Duan, Astrid Schneidewind, Igor Radelytskyi, David J. Voneshen, Russell A. Ewings, Matthew B. Stone, Alexander I. Kolesnikov, Barry Winn, Songxue Chi, R. A. Mole, D. H. Yu, Bin Gao, and Pengcheng Dai. Magnetic anisotropy in ferromagnetic CrI3. *Phys. Rev. B*, 101(13):134418, 2020. doi: 10.1103/physrevb.101.134418.

[163] Amilcar Bedoya-Pinto, Jing-Rong Ji, Avanindra K. Pandeya, Pierluigi Gargiani, Manuel Valvidares, Paolo Sessi, James M. Taylor, Florin Radu, Kai Chang, and Stuart S. P. Parkin. Intrinsic 2D-XY ferromagnetism in a van der Waals monolayer. *Science*, 374(6567): 616–620, 2021. doi: 10.1126/science.abd5146.

[164] M. Kim, P. Kumaravadivel, J. Birkbeck, W. Kuang, S. G. Xu, D. G. Hopkinson, J. Knolle, P. A. McClarty, A. I. Berdyugin, M. Ben Shalom, R. V. Gorbachev, S. J. Haigh, S. Liu, J. H. Edgar, K. S. Novoselov, I. V. Grigorieva, and A. K. Geim. Micromagnetometry of two-dimensional ferromagnets. *Nat. Electron.*, 2(10):457–463, 2019. doi: 10.1038/s41928-019-0302-6.

[165] A Manchon, J Zelezny, I M Miron, T Jungwirth, J Sinova, A Thiaville, K Garello, and P Gambardella. Current-induced spin-orbit torques in ferromagnetic and antiferromagnetic systems. *Rev. Mod. Phys.*, 91(3):035004, 2019. doi: 10.1103/revmodphys.91.035004.

[166] Kapildeb Dolui, Marko D. Petrovic, Klaus Zollner, Petr Plechac, Jaroslav Fabian, and Branislav K. Nikolic. Proximity Spin–Orbit Torque on a Two-Dimensional Magnet within van der Waals Heterostructure: Current-Driven Antiferromagnet-to-Ferromagnet Reversible Nonequilibrium Phase Transition in Bilayer CrI3. *Nano Lett.*, 20(4):2288–2295, 2020. doi: 10.1021/acs.nanolett.9b04556.

[167] Johannes Beck. Über Chalkogenidhalogenide des Chroms Synthese, Kristallstruktur und Magnetismus von Chromsulfidbromid, CrSBr. *Zeitschrift für anorganische und allgemeine Chemie*, 585(1):157–167, 1990. doi: 10.1002/zaac.19905850118.

[168] Evan J. Telford, Avalon H. Dismukes, Kihong Lee, Minghao Cheng, Andrew Wieteska, Amymarie K. Bartholomew, Yu-Sheng Chen, Xiaodong Xu, Abhay N. Pasupathy, Xiaoyang Zhu, Cory R. Dean, and Xavier Roy. Layered Antiferromagnetism Induces Large Negative Magnetoresistance in the van der Waals Semiconductor CrSBr. *Adv. Mater.*, 32 (37):2003240, 2020. doi: 10.1002/adma.202003240.

[169] Thomas Naimer, Martin Gmitra, and Jaroslav Fabian. Tuning proximity spin-orbit coupling in graphene/NbSe2 heterostructures via twist angle. *Phys. Rev. B*, 109(20): 205109, 2024. doi: 10.1103/physrevb.109.205109.

[170] Peigen Li, Jihai Zhang, Di Zhu, Cui-Qun Chen, Enkui Yi, Bing Shen, Yusheng Hou, Zhongbo Yan, Dao-Xin Yao, Donghui Guo, and Dingyong Zhong. Observation of In-Gap States in a Two-Dimensional CrI2/NbSe2 Heterostructure. *Nano Lett.*, 24(31):9468–9476, 2024. doi: 10.1021/acs.nanolett.4c01848.

[171] F. S. Bergeret, A. F. Volkov, and K. B. Efetov. Odd triplet superconductivity and related phenomena in superconductor-ferromagnet structures. *Rev. Mod. Phys.*, 77(4):1321–1373, 2005. doi: 10.1103/revmodphys.77.1321.

[172] A. I. Buzdin. Proximity effects in superconductor-ferromagnet heterostructures. *Rev. Mod. Phys.*, 77(3):935–976, 2005. doi: 10.1103/revmodphys.77.935.

[173] W A Fertig, D C Johnston, L E DeLong, R W McCallum, M B Maple, and B T Matthias. Destruction of Superconductivity at the Onset of Long-Range Magnetic Order in the Compound ErRh4B4. *Phys. Rev. Lett.*, 38(17):987–990, 1977. doi: 10.1103/physrevlett.38.987.

[174] R. S. Keizer, S. T. B. Goennenwein, T. M. Klapwijk, G. Miao, G. Xiao, and A. Gupta. A spin triplet supercurrent through the half-metallic ferromagnet CrO2. *Nature*, 439(7078): 825–827, 2006. doi: 10.1038/nature04499.

[175] Hideki Narita, Jun Ishizuka, Ryo Kawarazaki, Daisuke Kan, Yoichi Shiota, Takahiro Moriyama, Yuichi Shimakawa, Alexey V. Ognev, Alexander S. Samardak, Youichi Yanase, and Teruo Ono. Field-free superconducting diode effect in noncentrosymmetric superconductor/ferromagnet multilayers. *Nat. Nanotechnol.*, 17(8):823–828, 2022. doi: 10.1038/s41565-022-01159-4.

[176] Shawulienu Kezilebieke, Md Nurul Huda, Viliam Vano, Markus Aapro, Somesh C. Ganguli, Orlando J. Silveira, Szczepan Glodzik, Adam S. Foster, Teemu Ojanen, and Peter Liljeroth. Topological superconductivity in a van der Waals heterostructure. *Nature*, 588 (7838):424–428, 2020. ISSN 0028-0836. doi: 10.1038/s41586-020-2989-y.

[177] Fan Wu, Ignacio Gutiérrez-Lezama, Sara A López-Paz, Marco Gibertini, Kenji Watanabe, Takashi Taniguchi, Fabian O von Rohr, Nicolas Ubrig, and Alberto F Morpurgo. Quasi-1D Electronic Transport in a 2D Magnetic Semiconductor. *Adv. Mater.*, 34(16), 2022. doi: 10.1002/adma.202109759.

[178] Michael E. Ziebel, Margalit L. Feuer, Jordan Cox, Xiaoyang Zhu, Cory R. Dean, and Xavier Roy. CrSBr: An Air-Stable, Two-Dimensional Magnetic Semiconductor. *Nano Lett.*, 24 (15):4319–4329, 2024. doi: 10.1021/acs.nanolett.4c00624.

[179] Ke Yang, Guangyu Wang, Lu Liu, Di Lu, and Hua Wu. Triaxial magnetic anisotropy in the two-dimensional ferromagnetic semiconductor CrSBr. *Phys. Rev. B*, 104(14):144416, 2021. doi: 10.1103/physrevb.104.144416.

[180] Julian Klein, Benjamin Pingault, Matthias Florian, Marie-Christin Heißenbuttel, Alexander Steinhoff, Zhigang Song, Kierstin Torres, Florian Dirnberger, Jonathan B. Curtis, Mads Weile, Aubrey Penn, Thorsten Deilmann, Rami Dana, Rezlind Bushati, Jiamin Quan, Jan Luxa, Zdenek Sofer, Andrea Alu, Vinod M. Menon, Ursula Wurstbauer, Michael Rohlfing, Prineha Narang, Marko Loncar, and Frances M. Ross. The Bulk van der Waals Layered Magnet CrSBr is a Quasi-1D Material. *ACS Nano*, 2023. doi: 10.1021/acsnano.2c07316.

[181] Marco Bianchi, Kimberly Hsieh, Esben Juel Porat, Florian Dirnberger, Julian Klein, Kseniia Mosina, Zdenek Sofer, Alexander N. Rudenko, Mikhail I. Katsnelson, Yong P. Chen, Malte Rösner, and Philip Hofmann. Charge transfer induced Lifshitz transition and magnetic symmetry breaking in ultrathin CrSBr crystals. *Phys. Rev. B*, 108(19): 195410, 2023. doi: 10.1103/physrevb.108.195410.

[182] R. Yang, M. Corasaniti, C. C. Le, Z. Y. Liao, A. F. Wang, Q. Du, C. Petrovic, X. G. Qiu, J. P. Hu, and L. Degiorgi. Spin-Canting-Induced Band Reconstruction in the Dirac Material Ca1-xNaxMnBi2. *Phys. Rev. Lett.*, 124(13):137201, 2020. doi: 10.1103/physrevlett.124.137201.

[183] Somesh Chandra Ganguli, Markus Aapro, Shawulienu Kezilebieke, Mohammad Amini, Jose L. Lado, and Peter Liljeroth. Visualization of moiré magnons in monolayer ferromagnet. *Nano Lett.*, 23(8):3412–3417, 2023. doi: 10.1021/acs.nanolett.3c00417.

[184] Youn Jue Bae, Jue Wang, Allen Scheie, Junwen Xu, Daniel G Chica, Geoffrey M Diederich, John Cenker, Michael E Ziebel, Yusong Bai, Haowen Ren, Cory R Dean, Milan Delor, Xiaodong Xu, Xavier Roy, Andrew D Kent, and Xiaoyang Zhu. Exciton-coupled coherent magnons in a 2D semiconductor. *Nature*, 609(7926):282–286, 2022. doi: 10.1038/s41586-022-05024-1.

[185] Youn Jue Bae, Taketo Handa, Yanan Dai, Jue Wang, Huicong Liu, Allen Scheie, Daniel G. Chica, Michael E. Ziebel, Andrew D. Kent, Xiaodong Xu, Ka Shen, Xavier Roy, and Xiaoyang Zhu. Transient magnetoelastic coupling in CrSBr. *Phys. Rev. B*, 109(10):104401, 2024. doi: 10.1103/physrevb.109.104401.

[186] Yuanji Li, Ruotong Yin, Mingzhe Li, Jiashuo Gong, Ziyuan Chen, Jiakang Zhang, Ya-Jun Yan, and Dong-Lai Feng. Observation of Yu-Shiba-Rusinov-like states at the edge of CrBr3/NbSe2 heterostructure. *Nat. Commun.*, 15(1):10121, 2024. doi: 10.1038/s41467-024-54525-2.

[187] Yuliang Chen, Kartik Samanta, Naafis A. Shahed, Haojie Zhang, Chi Fang, Arthur Ernst, Evgeny Y. Tsymbal, and Stuart S. P. Parkin. Twist-assisted all-antiferromagnetic tunnel junction in the atomic limit. *Nature*, 632(8027):1045–1051, 2024. doi: 10.1038/s41586-024-07818-x.

[188] Joel Röntynen and Teemu Ojanen. Topological Superconductivity and High Chern Numbers in 2D Ferromagnetic Shiba Lattices. *Phys. Rev. Lett.*, 114(23):236803, 2015. doi: 10.1103/physrevlett.114.236803.

[189] B. Verlhac, N. Bachellier, L. Garnier, M. Ormaza, P. Abufager, R. Robles, M.-L. Bocquet, M. Ternes, N. Lorente, and L. Limot. Atomic-scale spin sensing with a single molecule at the apex of a scanning tunneling microscope. *Science*, 366(6465):623–627, 2019. doi: 10.1126/science.aax8222.

Curriculum Vitae

Keda Jin

Date of Birth:	May 15, 1995
Place of Birth:	Kunming, Yunnan, China
Nationality:	Chinese

Education

Since May 2021	**PhD student** in physics RWTH Aachen University, Germany Thesis Title: Probing Electric and Magnetic Order in 2D van der Waals Heterostructures with Scanning Tunneling Methods Supervisor: Prof. Markus Ternes
Oct. 2018–Mar.2021	**M.Sc.** in Functional Material Philipps-University Marburg,Germany Thesis Title: In-situ growth and characterization of molecular films of regio-selectively substituted pentacene species on Ag(111) Note: 1.4 Supervisor: Prof. Peter Jakob
Sep. 2013–June 2017	**B.Eng.** in Metallurgy Engineering Central South University, China

Research experience

May 2021–Dec 2024	Forschungszentrum Jülich

Sign: (Keda Jin)

Publication

1. **K. Jin**, T. Wichmann, S. Wenzel, T. Samuely, O. Onufriienko, P. Szabó, K. Watanabe, T. Taniguchi, J. Yan, F. S. Tautz, F. Lüpke, M. Ternes, and J. Martinez-Castro *Assembly of Arbitrary Designer Heterostructures with Atomically Clean Interfaces.* Adv. Mater. Interfaces (2023)

2. J. Martinez-Castro, T. Wichmann, **K. Jin**, T. Samuely, Z. Lyu, J. Yan, O. Onufriienko, P. Szabó, F. S. Tautz, M. Ternes, F. Lüpke, One-dimensional topological superconductivity in a van der Waals heterostructure. arXiv, doi: 10.48550/arxiv.2304.08142 (2023).

3. H. Boban, M. Qahosh, X. Hou, T. Sobol, E. Beyer, M. Szczepanik, D. Baranowski, S. Mearini, V. Feyer, Y. Mokrousov, **K. Jin**, T. Wichmann, J. Martinez-Castro, M. Ternes, F. S. Tautz, F. Lüpke, C. M. Schneider, J. Henk, L. Plucinski, Scattering makes a difference in circular dichroic angle-resolved photoemission. arXiv, doi: 10.48550/arxiv.2410.19652 (2024).